The Mechanistic Description of the Open Circuit Potential for the Lithiation of Magnetite Nanoparticles

Christianna N. Lininger

Submitted in partial fulfillment of the
requirements for the degree of
Doctor of Philosophy
in the Graduate School of Arts and Sciences

Columbia University

2018

© 2018

Christianna N. Lininger

All rights reserved

ABSTRACT

The Mechanistic Description of the Open Circuit Potential for the Lithiation of Magnetite Nanoparticles

Christianna N. Lininger

Batteries are ubiquitous in modern society, from the portable devices we use daily to the yet-to-be realized integration of batteries into the electrical grid and electrical vehicle markets. One of the primary roles of batteries to date has been to enable portability of devices, and as chemical energy storage becomes more affordable, batteries will play a larger role in how society cares for the environment by enabling technologies that are poised to decrease greenhouse gas emissions. Low cost and environmentally conscious materials are pivotal for the economic feasibility and widespread integration of batteries into new markets. Batteries operate far from equilibrium and may operate under extreme stress and varying loads, therefore, for a material to be successful in an operational battery it must meet multiple design criteria. Here, an in-depth analysis of magnetite, a low cost and abundant iron oxide studied for use as an electrode material in lithium-ion batteries, is presented.

In the second Chapter, an in-depth analysis into how magnetite accepts lithium into the solid state at low depths of discharge is examined with density functional theory and a mechanistic understanding of a phase change from the parent spinel to a rocksalt-like material is presented. When magnetite is used as an electrode material in a lithium-ion battery, lithium must enter into and eject from the solid state of the host material, where the direction of lithium movement is a function of the current in the battery. In many electrode materials, magnetite included, large structural rearrangements can occur in the host material as lithium moves into and out of the lattice. These structural rearrangements can be

irreversible and can contribute to overpotentials, decreasing efficiency and lifecycle for the battery. The structural rearrangements in bulk magnetite occurring due to lithium insertion are found to be driven primarily by Coulombic interactions. Additionally, the energetics and structural rearrangements for lithium insertion into defective magnetite and maghemite are examined, as these derivative structures commonly co-exist with magnetite, especially when the material is nanostructured. It is found that defective magnetite and maghemite accept lithium by a different mechanism, one that does not initially result in substantial structural rearrangement, as is the case in magnetite.

In Chapter three, the effects of nanostructuring magnetite on the reversible potential are examined as a function of nanoparticle size. Due to solid-state mass-transport resistances, active electrode materials in batteries are commonly nanostructured. When a material is nanostructured, the bulk properties are often replaced due to interesting phenomena that can occur as a result of stark differences between the nanostructured material and the bulk counterpart. These differences are often attributed to surface area to volume ratios, the exaggerated role of surface energies, lattice defects, and the variation in electronic behavior, all properties which change between a bulk and nanostructured material. The reversible potential is found to be particle size dependent, and this dependence is explained, in part, by the cationic defective surfaces in the particles and the differences in surface area to volume ratio between varying particle sizes. Evidence for these defects is presented with materials characterization techniques such as XRD and EELS studies. Finally, the reversible potential at low lithiation states is predicted theoretically and found to match well to the experimentally measured potential.

A study of the DFT predicted potentials and XRD characterization for multiple metastable pathways is examined in the fourth Chapter. Room temperature and long-time scale persistence of metastable phases is a pervasive phenomenon in nature. Magnetite is known to undergo both phase change and conversion reactions upon lithiation. Due to large mass transport and kinetic resistances, multiple phase changes are often observed in parallel during discharge, resulting in heterogenous phase formation in particles which can have large local lithium concentration variations. Phases which form during discharge can become kinetically trapped and the equilibrium state can therefore follow a metastable pathway. Theoretical potentials and XRD patterns are compared to the experimental patterns taken following 600 hours of relaxation following discharge at the slow rate of C/600. The evidence presented supports a metastable pathway occurring on the first voltage plateau.

In the fifth Chapter, the methodologies for the density functional theory calculations are presented in full detail. This includes various studies on the more subtle electronic properties of magnetite and its lithiated derivates studied herein. These studies include examination of the charge and orbital ordering problem related to the Verwey transition in magnetite, the charge and magnetic order in the rocksalt-like lithiated magnetite, and a full theoretical description of the various phases in the Li-Fe-O ternary phase diagram that were calculated to make the relevant conclusions in Chapters 2-4. Finally, corrections to DFT predicted formation energy and volume are presented.

The aim of this thesis is to use theoretical techniques to examine the lithiation of magnetite on the atomic scale and make meaningful connections to the experimentally observed electrochemical behavior of the material. To accomplish this, magnetite **and** the structural derivatives of magnetite that co-exist with the material under physically realistic

conditions must be treated theoretically. In this thesis, ties between phenomena occurring on the atomic scale and the measurable properties of the macroscopic system, such as voltage, will be related. It will be illustrated that as a function of nanoparticle size, the magnetite system can vary in its atomic structure and the resultant electrochemistry and phase change characteristics are both affected. The findings indicate the relevance of the atomic properties and nanostructure for magnetite to the observed and measured electrochemical properties of the material.

TABLE OF CONTENTS

LIST OF FIGURES

LIST OF TABLES

ACKNOWLEDGEMENTS

I would first like to thank my thesis advisor, Alan West. I once heard him say to a colleague that his most important contribution is his role as a mentor to his students. He has provided immense support in countless ways in the completion of this thesis and in my success as a graduate student. He has given me the tools to develop technical competence in electrochemistry and in chemical engineering. Most importantly though, he has given me the tool of a paradigm through which I can approach complex and difficult research problems, *an instrument for thinking* that I will most certainly take with me throughout my career, and for that I am very grateful

I would also like to thank Mark Hybertsen, who has advised me at great length through the technical details of the calculations that compose the body of this thesis. Many hours were spent hashing through the difficult subtleties in this work. He has taken the time and care to impart on me a great deal of his technical expertise, and I am very grateful for the time and attention he has given to this body of work and to my maturation as a researcher.

I would like to thank Michael Panunto, my physics professor at Butte Community College, who encouraged me to pursue a degree in the sciences. I would like to thank Kristin Millinkevich, who guided and mentored the early stages of my passions for chemistry while at Butte Community College. She gave me countless opportunities and devoted much time to explanation and my understanding of organic chemistry while at Butte Community college. I would like to thank Kathy Durkin, who was a mentor to me during my undergraduate research. She taught me many lessons about navigating academia and graduate school and was instrumental in my NSF GRFP proposal.

I would like to thank my lab mates, Nick Brady and Kevin Knehr, for their intellectually stimulating conversations and their contributions to my understanding of the magnetite system. I would also like to thank Andrea Bruck for the countless conversations we have had concerning the magnetite system studied at hand. I would like to thank Yan Li for her guidance on technical details and also her mentoring to me as a developing scientist and researcher.

I would like to thank my classmates, who have now become my friends, for their support, friendship, *and for all of the laughter*. Their comradery has made the difficult times in graduate school bearable.

Finally, I would like to thank and dedicate this thesis to my family. I would like to thank Rhonin, for the role he has played in my mental health during graduate school and for his unyielding loyalty. I would like to thank Amy, Richard, Matt, John, and Diane for their endless support and love. I am incredibly fortunate to have been taught so many lessons through example from my family members. My dad and brother have taught me the invaluable lesson of perseverance and resilience through adversity. My mom has taught me the importance of finding joy and the silver lining in all circumstances that I am faced with. Lastly, I would like to thank my husband, Kevin, who has been the most extraordinary source of encouragement and support in *all* of my endeavors. They have all individually shaped me in ways I cannot begin to comprehend and this thesis is dedicated to them.

There is no royal road to geometry.

-Euclid

CHAPTER 1: INTRODUCTION TO MAGNETITE, LITHIUM-ION BATTERIES, AND DENSITY FUNCTIONAL THEORY[1]

1.1 Relevance of Lithium-ion Batteries to Modern Society

Lithium-ion chemical energy storage was introduced in the 1970s[1] and has had a large impact on technological developments and modern society since its introduction. Lithium-ion batteries have been a critical component to the now ubiquitous portable electronics and have enabled countless other contemporary technologies. However, lithium-ion batteries have yet to make their full impact on daily life, as their implementation on both the grid and vehicle scales are yet to reach fruition. Lithium-ion batteries are poised to be key in the large-scale deployment of electric vehicles and implementation of renewable energy sources on the grid scale, where possibly the most long-lasting impact of this technology will be realized: the role of energy storage in the mitigation of greenhouse gases.

1.1.1 The Role of Energy Storage in Renewable Electricity Generation and Outlook for CO_2 Levels

CO_2 and other greenhouse gases act as insulators for the earth's atmosphere, and as such, higher CO_2 concentrations result in more heat maintained in the atmosphere, resulting in average global temperature rises.[2] Decarbonizing electricity sources has the greatest potential to decrease global CO_2 levels, as the largest fraction of global CO_2 emission by sector in the U.S. has historically been due to electricity and heat production.[3,4] Currently, the largest source of electrical energy (both U.S. + worldwide) comes from coal and for every

[1] Part of this chapter was written in a publication co-authored by Nicholas W. Brady and Alan C. West.[128]

kWhr electricity generated via coal burning, an average of 1 kg of lifecycle CO_2 is released into the atmosphere.[5]

Solar, wind, and other renewables are great alternatives to coal burning, they are continuously supplied by nature and do not need to be replenished, they do not contribute to depletion of fossil fuels, addition of greenhouse gases, and produce little to no pollutants.[6] However, due to the volatile and intermittent nature of the sun and wind, they are not a practical fuel source to supply continuously needed energy.[5] Additionally, the energy market does not currently have a widespread energy storage infrastructure in place. The demand of energy must be met by instantaneous supply, and the grid is not equipped to integrate intermittent renewable energy sources.[5,7] In order to utilize renewable fuel sources into the electric grid, there must be a method in place that can reliably and effectively store energy on a large scale.[7] Technologies must also be economical and reliant on abundant materials, and thus magnetite is an attractive electrode material.

Electrical energy storage systems (EESS) are considered one of the key technologies that will enable the realization of a renewable-energy-based grid, they are capable of smoothing out the intermittency of renewable energy sources and can mitigate inefficiencies in the current energy infrastructure.[5] Batteries are uniquely designed for storage integration on the grid level, they redeliver upwards of 90% of the energy they store, the technology is not geographically dependent, voltage output is not a strong function of the state of discharge which strengthens reliability, and batteries have shown to scale well.[8] Li-ion batteries are uniquely suited for grid-level storage as they have a long cycle life, high energy capacity, high power, and high efficiency.[5,9,10] However, the current cost of lithium-ion battery materials needs to be reduced in order for grid-level energy storage to be an economically feasible

solution.[5,7,11] Hence, the continued need for research and design in lithium-ion chemical energy storage emerges to mitigate current inefficiently designed power grids, increase renewable energy fuel sources, decrease fossil fuel depletion and greenhouse gas emission, and enable economically feasible Li-ion energy storage technologies for the green grid.[5–7]

1.2 The Physics of Lithium-ion Batteries

Individual battery cells can be combined to create a multi-cell configuration; the optimization of cell packs is an engineering-design problem that factors in cost and safety and other physical constraints. The cell scale (Figure 1.1a) is the most basic battery unit. This is where most of the chemistry and physics of the technology can be studied and where materials innovation and development are most active. Fundamental research of the phenomena occurring at interfaces and across multiple length scales can propel developments that reduce the costs, extend the life, improve the safety and performance of batteries, and may enable full penetration into transportation and grid-scale markets.

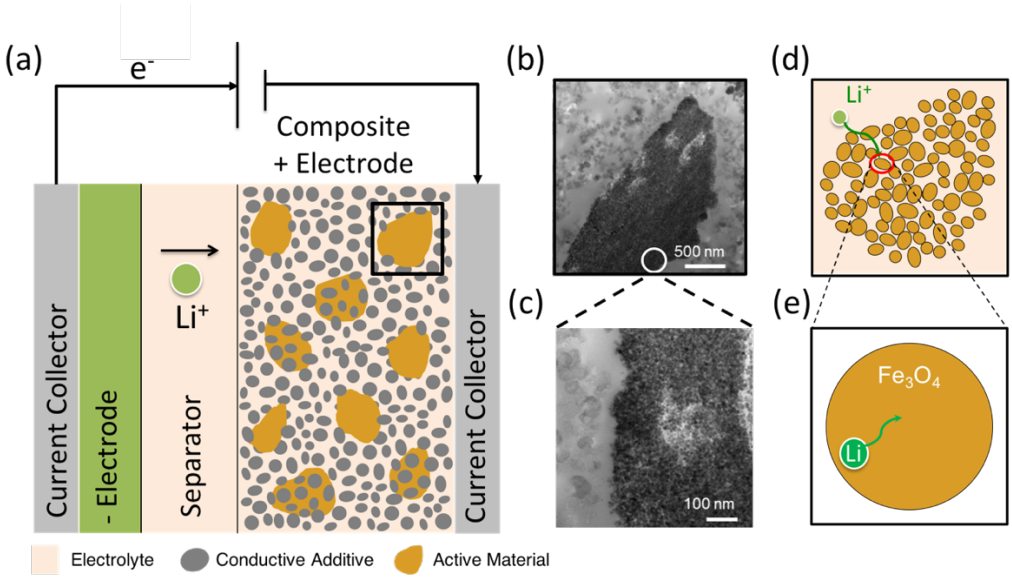

Figure 1.1 a) Schematic of a llithium-ion battery with Li^0 anode. The cathode is a composite compised of active material and conductive additive. Electron and Li^+ transport shown by arrows for discharge. b) TEM of micron sized agglomerates in Fe_3O_4 electrode[12] and c) magnification of agglomerate,

showing nanoparticulate Fe_3O_4.[12] d) Schematic of lithium-ion transport through porous regions between the nanopartictles of an agglomerate and e) solid-state transport of lithium through the nanoparticulate Fe_3O_4.

1.2.1 How a Lithium-ion Battery Works

Lithium-ion batteries store and release energy by conversion between chemical potential and electrical work. The main components of a lithium battery are the positive and negative electrodes, separator, and the electrolyte, as depicted in Figure 1.1a, where the two solid electrode materials are separated by a porous separator, and an electronically insulating solid or liquid electrolyte.[13] During discharge, chemical energy stored in the battery is released as electrical energy. Half reactions occur at each electrode and the porous separator facilitates the selective transport of species between electrodes as well as the physical separation between the two electrodes to disallow short-circuiting. At the anode, lithium is oxidized, producing free electrons and mobile lithium ions. From the anode, the electrons travel through a load, and the lithium ions travel through the electrolyte towards the cathode where they react with the active material (Figure 1.1a). The electrolyte acts to conduct ions but is necessarily electronically insulating, as to induce current out of the cell to be accessed in the form of electrical energy.[9] The oxidation half reactions at the negative and positive electrodes are illustrated in Reaction 1 and Reaction 2 respectively, and the total cell reaction is given in Reaction 3. Where θ represents a generic intercalation material that is capable of facilitating multiple electrons per formula unit. A solid lithium anode is shown in Figure 1.1a,, but other chemistries, such as lithium-graphite, are more commonly used in commercial batteries.

$xLi^0 \leftrightarrow xLi^+ + xe^-$ Reaction 1

$Li_x\theta \leftrightarrow xLi^+ + xe^- + \theta$ Reaction 2

$xLi^0 + \theta \leftrightarrow Li_x\theta$ Reaction 3

1.2.2 Measurement of Voltage and of the Reversible Potential

In a battery, the electrochemical potential difference between the working electrode and counter electrode is measured as a voltage. The electrochemical potential of a species is analogous to the chemical potential of that species, however, if the species is charged, the effects that electrostatics have on the electrochemical potential must be taken into consideration. This electrochemical potential is given in Equation 1, where μ_i is the electrochemical potential of species *i*, z_i is the charge of species *i*, F is Faraday's constant, and ϕ is the electric potential that species *i* interacts with.[14]

$$\mu_i = \mu_{i,chem} + z_i F\phi \quad \text{Equation 1}$$

The electrochemical potential difference measured between the two electrodes is the Gibbs free energy. The Gibbs free energy can be equated to the electrodes' affinities for electrons, providing information about which direction electrons will flow spontaneously and hence information about the reactions occurring in the system (Equation 2).[14]

$$\Delta G = \sum_i^{cathode} s_i\mu_i - \sum_i^{anode} s_i\mu_i \quad \text{Equation 2}$$

The measured voltage can be related to the Gibbs free energy with Faraday's constant, F, and the number of electrons transferred during the reaction, *x* (Equation 3). When there is zero net current between the electrodes, the net reaction is zero and the system is at equilibrium. The equilibrium voltage that is measured is called the reversible potential, assuming all electrodes are ideal. [14]

$$U_{rev} = -\frac{\Delta G}{xF}$$ Equation 3

Galvanostatic Intermittent Titration Technique (GITT) is an electrochemical experimental technique used to probe, among other properties, the reversible potential of a given electrochemical system. In GITT, the working electrode is discharged to a certain state of discharge, *x*, at which point the current is stopped. Once the current is stopped, the system is allowed to relax until the voltage no longer changes. The end of relaxation voltage is the open circuit potential at the state of discharge of interrupt, *x*. This experiment can be done for multiple states of discharge and the reversible potential can be formed for the entire operating window of the material.

1.3 Ionic Transport Processes and Nanostructuring

Secondary (rechargeable) lithium-ion batteries operate through intercalation and conversion reactions. Intercalation is the reversible insertion of ions into a host lattice without severe disruption of the host crystalline lattice, while conversion involves rearrangement of that lattice.[8,15] Lithium ions also move through the electrolyte during charge and discharge of the cell. Diffusion through the electrode is often limiting, as liquid ionic diffusivities are in the range of 10^{-6} cm^2s^{-1}, and solid-state ionic diffusivities are in the range of 10^{-18}-10^{-8} cm^2s^{-1}.[16,17] Electronic transport processes also occur, but are orders of magnitude faster due to the decreased size of electrons and incorporation of carbon black in electrodes to increase electrical conductivity.[17,18]

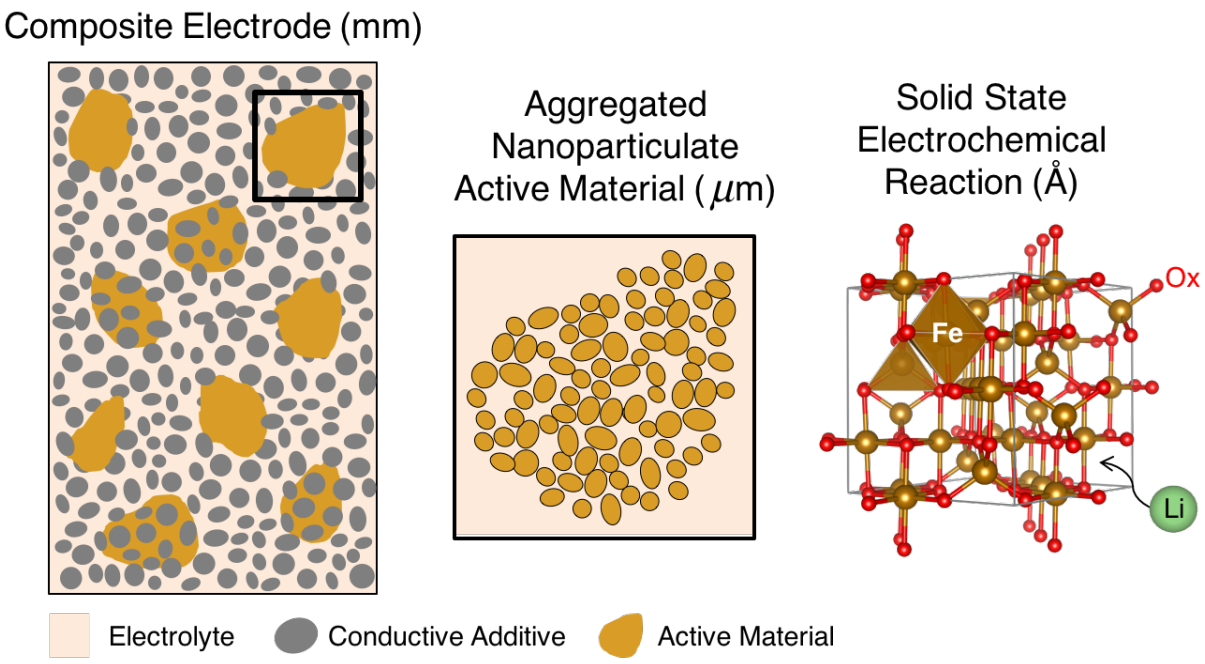

Figure 1.2: Cartoon depiction of composite electrode in lithium-ion battery, showing the mm electrode length scale (left), the micron sized agglomerates of nanoparticulate active material (middle) and the solid-state crystal structure of the active material (right).

Nanostructuring an electrode decreases the transport path lengths in the material and increases the number of grain boundaries which increases apparent diffusion coefficient. Through nanostructuring, surface areas are increased, resulting in more contact between electrode and electrolyte and also therefore improved charge-transfer kinetics.[19] A common commercial Li-ion cathode material, $FePO_4$, was initially deemed inoperable due to ionic transport issues. Upon nanostructuring, the material now reaches close to its theoretical capacity.[20] Nanostructuring an electrode material introduces higher surface energies, and secondary structures can be formed, which can be composed of agglomerated nanoparticles, on the order of microns.[19]

1.4 History of Magnetite and its Wide Range of Uses

Magnetite was discovered around 1500 B.C., and as such is the earliest known magnet with a rich history of study in the literature.[21,22] In contemporary investigations, magnetite has been considered for uses in multiple fields spanning applications in biomedical systems,[23–25] magnetic core memory for computers, catalysts for traditional chemical processes such as catalysis of ammonia synthesis, water-gas-shift reactions, and the Fischer-Tropsch synthesis,[26–28] to the proposed use of the material in lithium-ion electrodes, the topic of investigation herein. The wide range of interest in magnetite can be tied to its rich electronic, magnetic, and ionic structure in combination with its earth abundance and its property of being environmentally benign.

1.5 Electronic Structure of Magnetite

In magnetite, iron exists in two oxidation states and in two different coordination environments, with the 8a tetrahedral A-site fully occupied by Fe^{3+} and the 16d octahedral B-site 50:50 by Fe^{2+}:Fe^{3+}. Oxygen defines the cubic close packed lattice at the 32e site.[29] Magnetite is ferrimagnetic below the Neel temperature of 860 K, with the tetrahedral A sites and octahedral B sites ferromagnetically aligned within Wyckoff site designation and antiferromagnetically aligned between Wykoff site designation. Below 120 K, magnetite undergoes an abrupt transition from a semiconductor to an insulator, known famously as the Verwey transition. The Verwey model for magnetite aimed to describe the electronic origin for this transition.[30–32]

To understand the electronic structure and subtleties occurring in the Verwey transition, the Crystal Field Theory description of what occurs to the d-orbitals of Fe^{2+} and Fe^{3+} in the presence of oxygen in an FeO_6 octahedron must first be explored. Iron is a 3d transition metal

ion with 26 total electrons its neutral state, as indicated by the atomic number of iron on the periodic table. The electron configuration of neutral iron is $1s^2 2s^2 2p^6 3s^2 3p^6 3d^6 4s^2$ illustrated in Figure 1.3a. Ionization of iron occurs when electrons are lost and the material takes on a positive charge, iron is observed to occur as Fe^{2+}, Fe^{3+}, and Fe^{4+} in the presence of oxygen and lithium. Magnetite is comprised of the ferrous (Fe^{2+}) and ferric (Fe^{3+}) ions, and as such, those will be discussed herein. In the case of Fe^{3+}, three electrons are lost resulting in an electron configuration of $1s^2 2s^2 2p^6 3s^2 3p^6 3d^5$, with five unpaired electrons, one for each of the five 3d orbitals, as seen in Figure 1.3b. For the ferrous ion, Fe^{2+}, the electron configuration is $1s^2 2s^2 2p^6 3s^2 3p^6 3d^6$ with six electrons in the five 3d orbitals, leading to an additional electron in the 3d orbitals, the 'minority spin', leading to some of the interesting behavior of iron complexes, seen in Figure 1.3c.

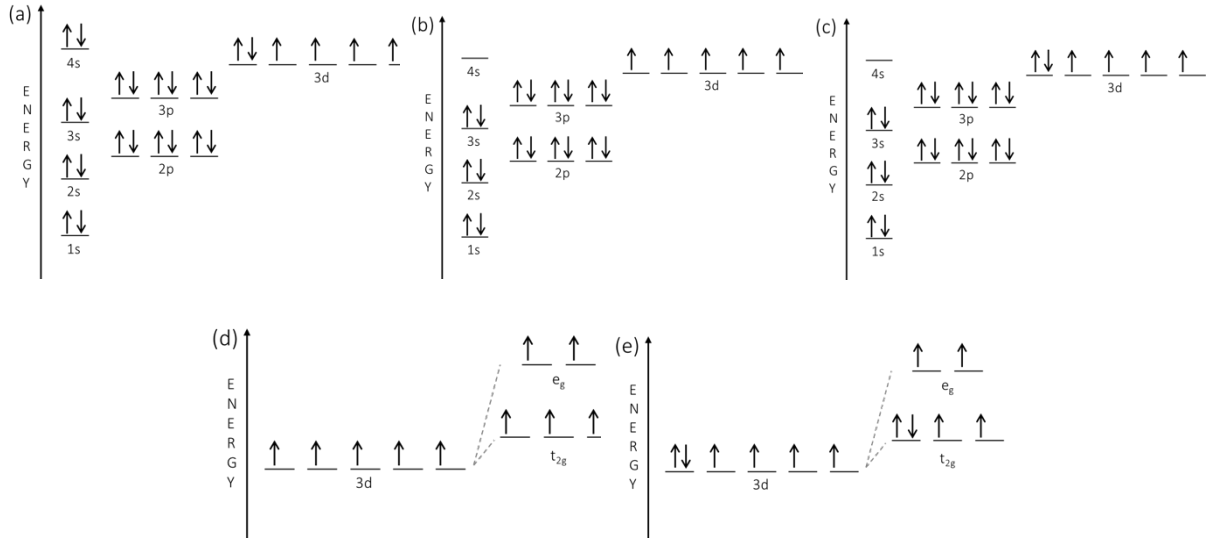

Figure 1.3.a) Neutral iron with 26 electrons. b) Ferric ion, Fe^{3+}, with 23 electrons and five unpaired electrons in the five available d-orbitals. c) Ferrous ion, Fe^{2+}, with 24 electrons and six unpaired electrons in the five available d-orbitals. Symmetry breaking of 3d orbitals in an FeO_6 octahedron for (d) Fe^{3+} and (e) Fe^{2+}, where no additional Jahn-Teller symmetry lowering is shown here.

1.5.1 Introduction to Crystal Field Theory

In Figure 1.3(a-c), the five d-orbitals are all degenerate. When oxygen physically approaches iron, some of the d-orbitals will experience repulsion from oxygen's electrons. In an octahedral coordination environment, FeO_6, oxygen approaches iron from the $\pm x$, $\pm y$, and the $\pm z$ directions and the five 3d orbitals are split to three t_{2g} states and two higher energy e_g states, as seen in Figure 1.3d for a Fe^{3+}. The two e_g states are comprised of dz^2 and dx^2-y^2, while the three t_{2g} states are comprised of dyz, dxz, and dxy. In the case of Fe^{2+}, there is a minority spin which induces additional symmetry breaking of the t2g states and is the basis for the well known Jahn-Teller effect, the additional symmetry breaking is not shown herein but will be further discussed in Chapter 5.7.

The implication of both Fe^{2+} and Fe^{3+} on the 16d site in magnetite is that the partially filled orbitals have a degree of freedom associated with the quantum state of the interacting electrons in addition to the degree of freedom associated with ionic positions of the Fe^{2+} and Fe^{3+} species on the lattice.[33] The quantum state of the electrons in the 3d orbitals of magnetite is defined by the arrangement of the charge order on the B-site lattice, the magnetic state on each iron, and the orbital occupation in the Fe^{2+} irons on the B-site, and as such modeling the electronic configuration can be quite complex.

1.5.2 The Verwey Transition in Magnetite

In the low temperature phase of Fe_3O_4, there are four total and two unique electronic states at the B-site which is comprised of 1:1 Fe^{3+}:Fe^{2+}. The Fe^{3+} splitting results in one electron on each of the three t_{2g} orbitals and one electron on each of the two eg orbitals, a high spin solution, shown in Figure 1.3d. In the case of Fe^{2+}, the additional electron can occupy any of the three t_{2g} orbitals (dxy, dxz, or dyz), resulting in three degenerate solutions,

as depicted in Figure 1.3(e). The distinction between the Fe^{2+} and Fe^{3+} d sites can be determined in DFT+U calculations directly by examining the minority spin occupancy or indirectly by examining the ionic distortions, although the latter method is likely less robust. In the case of electronic structure determination, the t_{2g} orbital of Fe^{3+} has an occupation of $\{\delta, \delta, \delta\}$, and Fe^{2+}, an occupation of $\{\alpha, \delta, \delta\}$. Where α=0.7-1.0 and δ=0.0-0.3. In the case of ionic distortions, the Fe^{3+} ion, being electronically symmetric with no minority spins, theoretically has all equal bond lengths of 2.03 Å. However, Fe^{2+}, with one minority spin electron occupying three t_{2g} orbitals degenerately, there are theoretically 4 Fe^{2+}-O^{2-} bonds at 2.15 Å and two at 2.03 Å. The plane that the four elongated bonds occupy identifies the t_{2g} orbital that houses the additional minority spin electron. This exemplifies the Jahn-Teller distortion on the Fe^{2+} B-site in Fe_3O_4.[33] In reality, the subtleties of the ionic distortions may not be so straight forward either experimentally or theoretically, as evidence by experimental low temperature refinements for magnetite,[34] and the effects of supercell size on the degrees of freedom associated with ionic distortion that the theorist must reconcile.

The two distinct octahedra described above, one for Fe^{3+} and the second for Fe^{2+} are proposed to be independent species that order below 120K, the Verwey temperature. According to Verwey, the Fe^{2+} and Fe^{3+} irons stack along the <100> direction in the Fe_3O_4 cubic cell. This ordering of charge that occurs below the Verwey Temperature results in electrons that are strongly localized and magnetite undergoes a sharp transition from a semiconductor to an insulator. The details of the charge ordering are further complicated by the additional degree of freedom associated with the minority spin orbital occupation. The charge and orbital ordering problem in magnetite is one that has been thoroughly

investigated theoretically and experimentally in the literature, however, the solution for the exact charge and orbital ordering remains contested.[21,33–37]

1.6 Magnetite as an Electrode Material in Lithium-Ion Batteries

The electrode material in a Li-ion battery must allow for reversible intercalation of lithium, and there are a range of materials capable of this behavior.[38,39] In the case of magnetite for use as an electrode in lithium-ion batteries, the material was initially attractive due to its high theoretical capacity and its environmental abundance. The theoretical capacity of the material as a positive electrode is 926 mAhr/g, as it can accept 8 e- per formula unit of Fe_3O_4. Magnetite, $(Fe_{8a}^{3+})[Fe^{3+}Fe^{2+}]_{16d}O_{4,32e}^{2-}$, has a close-packed inverse spinel structure and undergoes both intercalation and conversion reactions upon full lithiation. However, the material has suffered some performance limiting drawbacks. The solid-state transport of lithium in magnetite is observed to be slow, lending to high mass-transport resistances.[40] The material's performance has also been observed to be highly dependent on discharge rate.[41]

1.6.1 Nanoparticulate Magnetite in Lithium-ion Electrodes

Magnetite has been studied as a cathode material since the 1980s, both experimentally[38] and theoretically,[42] and as a result much is known about how the material accepts lithium. At low lithium concentrations, there is an intercalation regime followed by a phase change that proceeds with slow kinetics. At high lithium concentrations, conversion to $Li_2O + Fe^0$ is observed.[42–44] The average solid-state lithium concentration at which these processes are observed is a function of particle size and discharge rate.[41,45] Due to slow

kinetics, particle-size dependence, and irreversibilities during cycling, the realized capacity can be significantly lower than the theoretical maximum.

To mitigate the solid-state transport resistances, magnetite is nanostructured, which can lead to the formation of secondary structures such as the agglomerates of nanoparticles observed in Figure 1.1b, 1c, and Figure 1.2.[12,46–49] Due to these secondary structures, the performance of nanoparticulate magnetite in an operating battery has a dependence on the structural matrix in the electrode. Recent studies have utilized unique structural motifs and have alleviated the meso-scale transport resistances.[50]

1.6.2 Mechanistic Understanding of the Lithiation of Magnetite

Pioneering work on the lithiation of magnetite was conducted by Thackeray, David, and Goodenough in 1982. Thackeray *et al.* conducted open circuit measurements in conjunction with powder X-ray diffraction measurements of <44 μm Fe_3O_4 particles. Measurements performed 24 hours after lithiation were used to elucidate the reaction mechanisms occurring during lithiation of magnetite (Figure 1.4).[38] Thackeray *et al.* reported that initial lithium insertion into magnetite, $(Fe_{8a}^{3+})[Fe^{3+}Fe^{2+}]_{16d}O_{4,32e}^{2-}$ (Figure 1.4a), produced a defective rocksalt, $[Li^{+}Fe^{2+}]_{16c}[Fe^{3+}Fe^{2+}]_{16d}O_{4,32e}^{2-}$, (Figure 1.4d). The authors hypothesized that lithium inserted onto vacant 16c sites until a critical concentration was reached, where Coulombic repulsion between Li in 16c sites and iron in the nearby tetrahedral 8a sites caused the tetrahedral 8a iron to move to vacant octahedral 16c sites (Figure 1.4b and c). Lithiation past x=1.0 resulted in lithium insertion into vacant tetrahedral sites, $(Li^{+})_{8a/8b/48f}[Li^{+}Fe^{2+}]_{16c}[Fe^{2+}Fe^{2+}]_{16d}O_{4,32e}^{2-}$. Full lithiation to 8 equivalents resulted in conversion to Li_2O + Fe^0.[38] The first theoretical investigation of

lithium insertion into Fe_3O_4 was carried out by Islam and Catlow in 1988.[42] They used interatomic potentials to model host-host and host-intercalate ion interactions and validated Thackeray *et al.*'s findings, that lithium preferentially occupies vacant octahedral sites over tetrahedral sites, and that lithium insertion resulted in the displacement of tetrahedral 8a iron.[38,42]

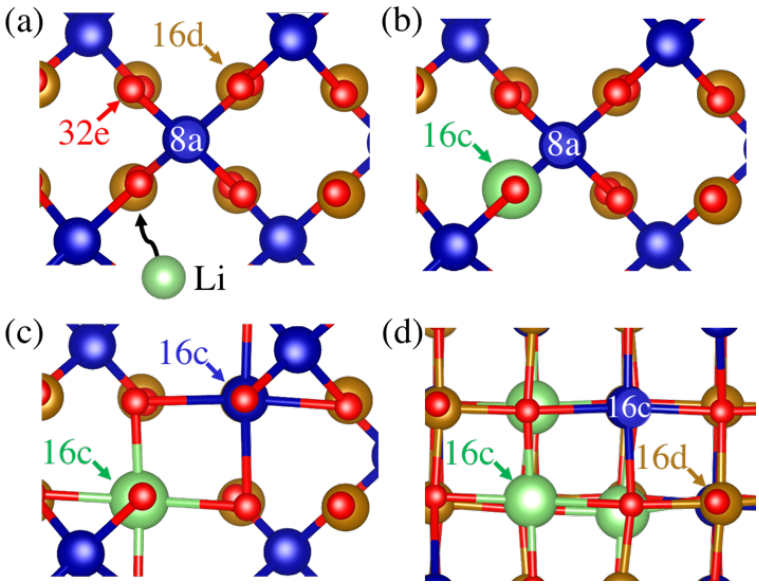

Figure 1.4 a) Zoom in on Fe_3O_4 with tetrahedral 8a iron in blue, octahedral 16d iron in brown, and 32e oxygen shown in red. Lithium is shown in green. All 16c sites are vacant. b) A structure showing lithium inserting onto a vacant 16c site. c) The resultant Coulombic repulsion from the tetrahedral 8a iron and the inserted 16c lithium causes 8a iron to migrate to a vacant 16c site. d) Full movement of all 8a iron to 16c sites due to Coulombic interactions.

In a subsequent review in 1987 by Thackeray *et al.*, a more refined reversible potential was reported. Two plateaus were observed, the first originating at x=1.0 at a potential of 1.2 V, for which the products could not be determined from powder XRD due to poor crystallinity. The second plateau occurred from x=1.5 through full lithiation, believed to be the conversion to Li_2O + Fe^0.[51] Both of the reversible potentials in the literature reported by Thackeray *et al.* are reproduced in Figure 1.5b. In 2016, Knehr *et al.* reported the reversible potential for lithiation into 6, 8, and 32-nm Fe_3O_4 particles, using the resting

voltage 30 days after lithiation; the 6, 8, and 32-nm particles undergo two voltage plateaus, the first at ~1.8 V and the second at ~1.2 V (Figure 1.5a).

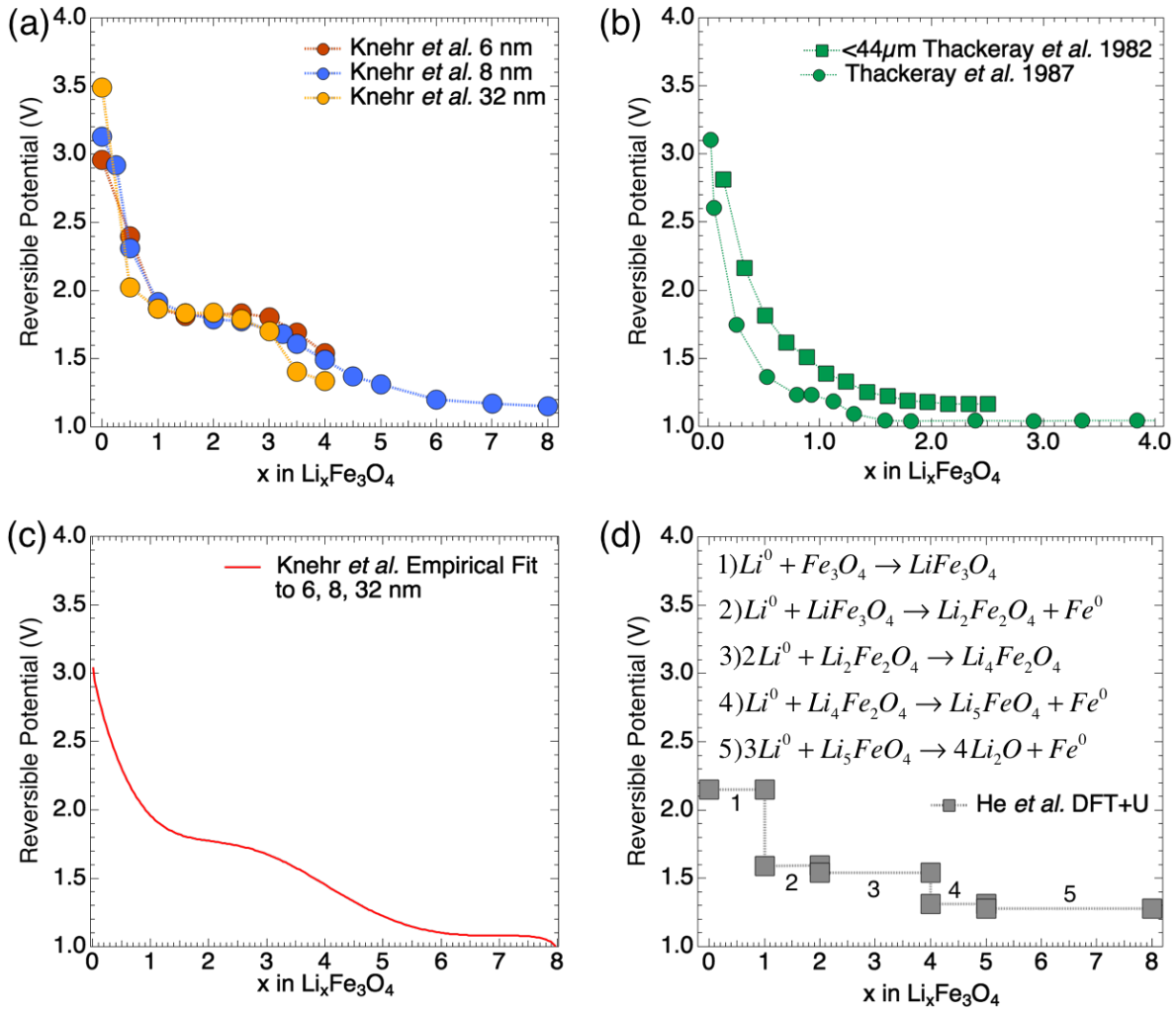

Figure 1.5 Literature reporting's of reversible potential for lithiation of magnetite. a) GITT experiments of 6, 8, and 32-nm Fe_3O_4.[40,52] b) GITT experiment of <44 micron Fe_3O_4.[38,51] c) Redlich-Kister empirical fit to 6, 8, and 32-nm data in a).[40,52] d) DFT+U determined OCP from He et al.[41]

Reversible potentials can be estimated from first principles with Density Functional Theory (DFT) calculations.[53–55] To accurately capture the electronic and magnetic properties in magnetite, the electron correlation in the *d* orbitals of iron must be accounted for with the Hubbard U correction.[56,57] DFT+U voltages are calculated from periodically repeating structures representative of bulk materials at 0 K and 0 pressure. Guided by the stable

phases on the ternary Li-Fe-O phase diagram, He *et al.* used DFT+U calculations to predict the reversible potential of lithium insertion into bulk magnetite over the full range of lithiation, $0 < x < 8$ (Figure 1.5d).[41] However, from Figure 1.5a and 3b it appears that the observed reversible potential varies as a function of magnetite particle size. This indicates that although the DFT+U studies can give insight into possible reactions occurring in a bulk material, models and first principles methods that capture the effects of nanosizing may be necessary for a full understanding of the thermodynamics of magnetite. For example, surface non-idealities in magnetite may be important, and would be especially impactful as nanoparticle size decreases.

1.6.3 Observation of Phase Change during the Lithiation of Magnetite

At the atomic length scale, the insertion of lithium into host materials can cause phase change by inducing movement of the iron atoms. The slope of the reversible potential can be used to suggest when two phases are in equilibrium, while materials characterization methods allow for equilibrium phase identification.[58,59] The reversible potential for full discharge ($0 < x < 8$) of 8-nm magnetite shows two flat voltage plateaus ($1 < x < 2.5$ and $5\text{-}6 < x < 8$), suggesting two phase changes, as seen in Figure 1.5a. However, magnetite has slow phase-change kinetics, so during discharge a voltage plateau may be difficult to observe, making it challenging to rely on only electrochemical measurements to identify the formation of a new phase.

Using *in situ* TEM, He *et al.* observed multiple phases in a single 80-nm nanoparticle, due to the occurrence of simultaneous reactions.[41] Bock *et al.* also observed particle phase inhomogeneity and studied the effect of particle size on the kinetics of phase change. Bock *et al.* used *in situ* XRD and *ex situ* XAS on 11-nm and 39-nm magnetite particles and found

that the mechanism of the first intercalation process, $0 < x < 1.0$, was independent of particle size. However, the mechanisms for lithiation beyond x=1, that involved the Fe^0 conversion process, appeared to be crystallite-size dependent.[45] In Figure 1.6a, which is adapted from Abraham *et al.*, the results of various studies are summarized as a function of lithium concentration, in 9-10.6 nm Fe_3O_4 particles.[60] The X-ray Diffraction (XRD) data[61] in the first column is a measure of the averaged long-range order in a sample, while the next four columns[44] give structurally refined information concerning local chemical environments. Possible discrepancies within Figure 1.6a and with other studies may be attributed, in part, to the significant spatial variations in lithiation state.

(a)

	XRD	XANES	EXAFS	STEM	HAAD/ABF
	Bulk information	*Atoms local environment, coordination number, distance between atoms*		*Atomic resolution imaging, contrast directly related to atomic number*	
x=1.0	Inverse Spinel (0.7)	Fe(8a) Decreasing (0.7)	No Change (0.7)	Fe(8a) → Fe(16c) (0.6)	
x=2.0	Inverse Spinel (1.7)			FeO Peaks	Equal Fe occupation on 16c, 16d (FeO)
x=3.0	Intermediate Structure (2.8)	Fe8a Decreasing (2.8)	10-20% FeO-like (2.8)		
x=4.0	FeO	Fe Oxidation State Change	Single Fe-Fe Bond length		No Fe^0, Increased Li on 8a, 48f, 8b
x=6.0			20% Fe^0	Li_2O, FeO, Fe^0 ~1 nm BCC Fe^0 particles	Fe^0/FeO, Presence of nanograins
x=8.0	FeO		50% Fe^0, Single Fe-Fe Bond length (FeO)	Li_2O, Fe^0, 1 nm nanograins	Fe^0/FeO More Fe^0 than at 6.0

(b)

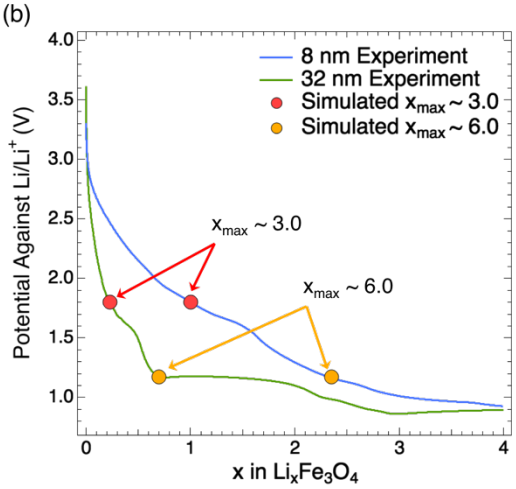

Figure 1.6a) Materials characterization results for 9-10.6 nm Fe_3O_4 as a function of x. b) Experimental discharge curves at C/200 for 8-nm and 32-nm Fe_3O_4 and mutli-scale simulation predictions for the concentrations of lithium at the surface of the agglomerate, x_{max}.

To probe the observation of phase inhomogeneity in lithiated magnetite nanoparticles, a validated model was used to predict the maximum lithium concentrations, x_{max}, within the system as a function of the measured discharged concentration in Figure 1.6b.[40,52] The simulation predicts that the 32-nm particles undergo much higher local lithium concentrations than the 8-nm particles at the same depth of discharge. As seen in Figure 1.6b,

when x~0.75 equivalents of lithium have been discharged in a system comprised of agglomerated 32-nm magnetite particles, the local Li concentrations are predicted to be as high as x~6.0. When this same concentration, x~0.75, is discharged in a system comprised of agglomerated 8-nm particles, the maximum local Li concentrations are less than 3.0. At 6.0 equivalents, the conversion reaction to $Li_2O + Fe^0$ is expected to occur, but at concentrations less than 3.0 equivalents, a FeO-like phase or composite $FeO{\cdot}Li_2O$ have been observed.[44,45,60] These local increased concentrations result from transport resistances on both the agglomerate-scale and the crystal-scale. This is commensurate with Bock *et al.'s* observation that the larger particles, with larger Li^+ diffusion lengths (higher solid-state transport resistances), converted to $Li_2O + Fe^0$ at lower average lithium concentrations than the smaller particles, presumably because of higher localized solid-state Li concentrations.[45] The simulation predictions allow for a reconciliation of the observation of phase inhomogeneity within the crystals, and how the inhomogeneities change as a function of crystal size.

1.6.4 Cycling and Dynamic Behavior

Capacity fade can indicate non-idealities, including side reactions which may be especially important in the first cycle when the solid-electrolyte interface (SEI) is formed. Capacity fade can arise from many factors including irreversible phase change, mechanical stress, and surface modification of the active material.[62,63] In practice, the first cycle may be engineered to result in irreversible SEI formation that prolongs the life of the battery. Using cyclic voltammetry on magnetite, one study found significant differences between the first discharge cycle and all subsequent cycles. Namely, the first discharge showed three peaks corresponding to three distinct mechanisms of lithium insertion into magnetite: lithium

insertion into octahedral sites, shifting of tetrahedral iron to octahedral sites, and conversion to $Li_2O + Fe^0$ (which occurs in parallel to lithium insertion into carbon). However, the second and subsequent discharge cycles only show one reduction peak, attributed primarily to the $3FeO + 6\ Li^+ + 6\ e^- \rightarrow 3Fe^0 + 3Li_2O$ conversion reaction.[49] In another cycling study, following full lithiation to $Li_8Fe_3O_4$, delithiation was unable to extract all of the inserted lithium, and the material failed after four cycles.[64] The inability to extract all inserted lithium suggests an irreversible phase change may arise at some point between $0 < x < 8$. Komaba *et al.* found that 10-nm and 100-nm magnetite particles were shown to cycle without substantial fade for up to 25 cycles if the material was only discharged to $x < 2$. However, Komaba *et al.* found that 400-nm magnetite particles cycled poorly compared to the 10 and 100-nm.[46]

1.7 Density Functional Theory for Strongly Correlated Materials

Density Functional Theory (DFT) models the electronic structure of atoms, on the basis that the properties of a system of interacting particles can be determined from their electronic density.[65,66] Transition metal oxides (TMO) comprise a class of materials with interesting electronic properties due to the strongly correlated behavior of the d- and f-orbitals. Electrons that would normally be itinerant in a s- or p- orbital, become localized due to Coulombic repulsion of neighboring d- or f- electrons. This localization behavior leads to metal-insulator transitions, and deviation from traditional band-gap theory.[67,68] In traditional band theory, materials such as NiO, FeO, and MnO are all ionic, with partially filled 3d orbitals, and therefore should have high electronic mobility and be metallic. In contrast, they are experimentally observed to be insulators.[69] These non-ideally behaving materials are called Mott-Insulators. A Mott-Insulator is a material that is predicted to be metallic and to have mobile electrons, but due to the strong Coulombic repulsion occurring in the d- and

f- orbitals, the electrons are limited in their mobility and the material exhibits insulating properties.[69]

DFT fails to capture the electronic properties of materials with partially filled d- and f- bands, transition-metal oxides, and prototypical Mott-insulating materials.[70] When trying to model strongly correlated materials with DFT, a unique problem arises stemming from this Coulombic repulsion. DFT is a mean-field theory and as a result, the electronic density is treated as a smeared out delocalized electron gas that behaves like the average of the entire density. This is a sufficient approximation to capture the behavior of most materials, however this averaged behavior is inadequate when it comes to the strongly correlated TMO.[71,72] Density functional theory predicts that the TMO have metallic ground states with mobile electrons in their highest bands, when in fact they are insulators at 0K. Additionally, the theory underestimates their lattice parameters and overestimates their binding energies.[72] In DFT, the potential defining the interactions in the system is a function of the electron density only, however in order to capture the electronic correlation correctly, an orbital-dependent potential must be formed.

In this orbital dependent potential, the electrons are considered on an individual basis, and each electron has a strong influence on its neighboring electrons, hence many-body terms are introduced for the electronic energy.[66,68] This orbital dependent version of DFT is commonly referred to as DFT+U, with inclusion of the Hubbard U parameter. Where the U parameter represents the energetic penalty due to Coulombic repulsion for double occupation of a single orbital.[68,73] In Equation 4, the DFT+U formulation shows that the energy as a function of the electron density, *p(r)*, is a function of the traditional DFT energy which is only a function of the electronic density, plus the Coulombic repulsion energy, which

is a function of the occupation numbers of the localized orbitals, *m* and *m*', at atomic site I, with electron spin *q*. Since atomic site I and its electrons are already accounted for in E_{DFT}, the double counting of these must be subtracted, which is the last term in Equation 4, E_{DC}.[66] This improved DFT+U is capable of accurately representing the electronic and chemical properties of strongly correlated materials.[68]

$$E_{DFT+U}[p(r)] = E_{DFT}[p(r)] + E_U[n_{mm'}^{Iq}] - E_{DC}[n^{Iq}] \quad \text{Equation 4}$$

1.8 Density Functional Theory for Electrochemical Processes as they Pertain to Lithium-ion Batteries

DFT is useful in determining the electronic configuration of the lowest energy structure of a material. This lowest energy state is a zero temperature and zero pressure structure and is referred to as the ground state. The thermodynamic reference for these ground structures is their atomic constituents at an infinite distance apart. Since electrochemical open circuit potential is a measure of the equilibrium state of two electrodes, DFT predicted ground state calculations of solid-state electrodes can be used determine the reversible potential of a battery.

As seen in Equation 3, the reversible potential U_{rev} is proportional to the change in the electrochemical potential, ΔG. The Gibbs free energy is the change in the internal energy, E, plus the pressure-volume work, minus the entropic contributions (Equation 5).

$$\Delta G = \Delta E + P\Delta V - T\Delta S \quad \text{Equation 5}$$

Since DFT is a zero pressure and zero temperature theory, the Gibbs free energy is approximated as the change in the internal energy, or the reaction energy, ΔE. The entropic and pressure-volume effects that are neglected in the zero temperature free energy are

generally regarded as small compared to the reaction energy, on the order of ~1-5 eV. However, inclusion of temperature and other effect have shown to better the agreement between theoretical and experimental voltages in some cases.[55] With these approximations made, the DFT determined open circuit potential can be seen in Equation 6.

$$U_{rev}(x) = -\frac{\Delta G}{xF} = -\frac{\Delta E + P\Delta V - T\Delta S}{xF} \approx -\frac{\Delta E}{xF} \quad \text{Equation 6}$$

The total cell reaction is given in Reaction 3, with this reaction, ΔE can be defined as the free energy of the products minus the free energy of the reactants (Equation 7).

$$U_{rev}(x) = -\frac{E(Li_xFe_3O_4) - E(Fe_3O_4) - xE(Li^0)}{xF} \quad \text{Equation 7}$$

The DFT ground state calculations consider the potential difference between the working electrode and counter electrode materials in their ground bulk state. Differences between DFT voltages and experimental voltages can give insight into physical processes. As will be shown in the Chapters 2 and 3, the effects and non-idealities that occur as a function of nano-structuring an electrode material has a measurable impact on the experimental reversible potential and DFT is employed to elucidate the physical atomic scale non-idealities. In Chapter 4, voltages and XRD patterns for metastable pathways are predicted with DFT and compared to experimental measurements to show that in magnetite nanoparticles, the open circuit potential follows a metastable pathway.

CHAPTER 2: ENERGETICS OF LITHIUM INSERTION INTO MAGNETITE, DEFECTIVE MAGNETITE, AND MAGHEMITE[2]

2.1 Chapter Overview

At low concentrations of lithium insertion into inverse spinel magnetite Fe_3O_4, a phase change to rocksalt-like $Li_xFe_3O_4$ has been observed. We use density functional theory based (DFT) calculations to study the structural origins of this phase change, the concentration at which it occurs, the role of iron vacancies, and the stability of the various motifs that form during the electrochemical reduction process in the Li-Fe-O ternary space up to x=1.33. We compare our results to new experimental measurements of the open circuit voltage for 8-9 nm magnetite particles over a comparable range of lithium insertion. Of the vacant sites in magnetite, 16c, 8b, and 48f, lithium insertion is found to be most stable on 16c. Coulomb interactions between the added lithium and iron at the 8a site in magnetite lead to substantial displacement of the iron. As further lithium is added, the most energetically favored motif involves lithium clustering in 16c sites around the shifted 8a iron up to a total of three lithiums. In competition with the lithium clustering motif, lithium insertion can be accompanied by the full displacement of all 8a iron to 16c sites, to form the rocksalt-like $Li_xFe_3O_4$, saturating at x=1. The defective rock-salt structure is found to be more stable than the lithium clustering motif for $x \geq 0.5$. The rocksalt-like $LiFe_3O_4$ is found to be stable in the Li-Fe-O ternary space for a continuous range of Li-Fe organization on the 16c sites, stabilized by Coulomb interactions. For x<1, neither the lithium clustering motif, nor

[2] This chapter presents work that was done in collaboration with: Christina A. Cama, Kenneth J. Takeuchi, Amy C. Marschilok, Esther S. Takeuchi, Alan C. West, Mark S. Hybertsen.

the defective rock-salt like structure for $Li_xFe_3O_4$ are stable against phase segregation to $LiFe_3O_4$ and Fe_3O_4. This phase segregation ($0<x<1$) occurs at a predicted voltage of ~2.0 V. However, when iron defects on the 16d site are introduced, lithium insertion to the vacant 16d sites in $Fe_{2.875}O_4$, and γ-$Fe_{2.67}O_4$ (maghemite) result in stable intercalated materials at a predicted voltage of ~3.0 V. Beyond the concentration of such iron vacancy defect sites, phase segregation is predicted to the rocksalt-like $Li_{1.125}Fe_{2.875}O_4$ and $Li_{1.33}Fe_{2.67}O_4$, again at ~2.0 V. These results are consistent with observed open circuit voltages.

2.2 Introduction

There is broad interest in a range of iron oxides as electrode materials for secondary lithium-ion batteries due to their low cost, high abundance, and low toxicity.[15,60,74–76] Magnetite (Fe_3O_4), hematite (α-Fe_2O_3), maghemite (γ-Fe_2O_3), and α-$LiFe_5O_8$ have been investigated as electrode materials since the 1980s.[38,42,77–82] Magnetite specifically, undergoing both intercalation and conversion reactions, has a theoretical capacity of 926 mAh/g against Li^0, corresponding to eight Li per formula unit. However, due to the close packed inverse spinel crystal structure, solid state mass-transfer resistances can lead to poor active material utilization and the inability to reach the theoretical capacity at nominal rates. While the use of nano-scale active material has been extensively investigated to improve capacity and other characteristics, the choice of the matrix, processing of the composite, the occurrence of side reactions, and irreversibility upon charging can all be significant.[46,47,49,64,83–88] Fundamental understanding of lithiation pathways, optimization of nanostructured active material, and the interplay with the matrix all remain as significant challenges to be addressed through in-depth characterization and multi-scale modeling.[40,41,92,44,45,49,60,61,89–91]

Magnetite has an inverse spinel structure ($Fd\bar{3}m$) with the oxygen atoms forming a face-centered cubic close-packed lattice and the iron atoms occupying specific interstitial sites relative to that lattice, octahedral 16d and tetrahedral 8a, as visualized in Figure 2.1. If instead, iron atoms occupied all of the octahedral sites (16c and 16d), the result would be wüstite (FeO) with a rock-salt structure. In Fe_3O_4, the iron is nominally mixed valence. In the cubic eight formula unit cell, eight Fe^{3+} cations occupy tetrahedral sites (A-type) while eight each of Fe^{2+} and Fe^{3+} occupy octahedral sites (B-type).[32] This can be expressed as $(Fe_1^{3+})_{8a}(Fe_1^{3+}Fe_1^{2+})_{16d}(O_4^{2-})_{32e}$. Robust ferrimagnetic order results from antiferromagnetic coupling between A and B type cations. There remain possible competing structures corresponding to the distribution of Fe^{2+} and Fe^{3+} on the 16d site. Also, for the Fe^{2+} ions in an octahedral environment, the extra d-electron occupies three-fold degenerate t_{2g} orbitals that can result in distortions due to the Jahn-Teller (JT) effect. Below the Verwey transition at ~120 K, orbital and charge ordering emerge together with structural distortions, the detail of which has been determined surprisingly recently.[35,36] The orbital and charge degrees of freedom represent a complex space with implications for the entropy change at the Verwey transition[32,93] and the interplay of competing, low symmetry structures that ultimately determine the low temperature phase.[33,34,94]

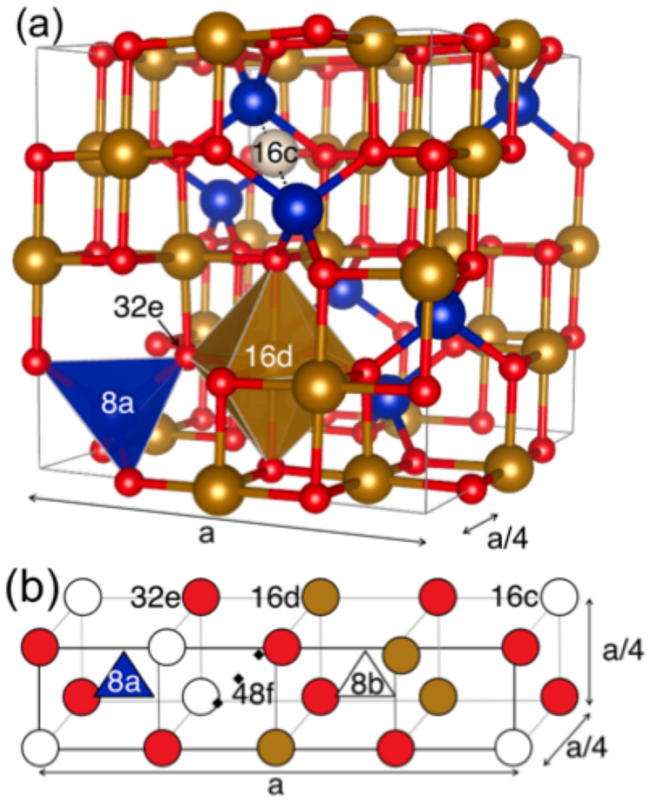

Figure 2.1. (a) Cubic inverse spinel structure for Fe_3O_4, where iron in 16d octahedral sites are brown, iron in tetrahedral 8a are blue, cubic close packed oxygen on 32e are red, and a single vacant 16c site has been depicted in white to show equidistance to 8a sites. The labeled 32e oxygen, 16d octahedron, and 8a tetrahedron in (a) correspond to the labeled 32e, 16d, and 8a atoms in the cartoon depiction of one quarter of the unit cell in (b).

Guided by nominal ionic charges on the near neighbors, the empty octahedral 16c sites are most attractive for an additional charge, followed by the lower symmetry 48f sites. However, insertion of Li^+ onto an octahedral 16c site exposes it to two, nearest-neighbor nominally Fe^{3+} cations (Figure 2.1b). Thackeray, *et al.*, applied this picture to develop their hypothesis for the structural response upon lithiation.[38] At low levels of lithiation, below a critical concentration (x_c) this repulsion would be accommodated locally. The natural outlet for the perturbed local Fe^{3+} on 8a sites drives them toward nearby empty 16c sites. Since each 16c site has two 8a neighbors, local displacement of Fe^{3+} to 16c sites sets up a cascade

of cation shifts. Above x_c, a concerted shift of Fe^{3+} from 8a to 16c sites would occur, resulting in a rocksalt-like structure with partial occupancy $(Li_xFe)_{16c}$, $x_c<x<1$. This picture was supported by simulations based on empirical interaction potentials.[42] The simulations also suggested that, for low levels of lithiation, up to three Li^+ would cluster together instead of being randomly dispersed.

To give a frame of reference for discussion of lithiation of magnetite, a Li–Fe–O ternary convex hull is shown in Figure 2.2 primarily based on data from the Materials Project. The stable phases shown are all known compounds (Table 5.4).[95] We add α-$LiFe_5O_8$, also known from experiment.[79,81,96] The dashed line illustrates the continuous insertion of Li into Fe_3O_4 to form $Li_xFe_3O_4$, with some discrete possible compounds indicated for x=1, 2, 4, 5, and 8 at tie line intersections. The stability of any phases along this line, thermodynamically or kinetically, is fundamental to understanding the insertion process. For segments along this line where the phases are unstable, absent kinetic limitations, each successive Gibbs triangles in Figure 2.2 defines phase segregation products. The corresponding electrochemical open circuit voltage consists of a series of plateaus. For x>1, this would involve formation of Fe^0 and a sequence of intermediate phases leading to final conversion to Li_2O.

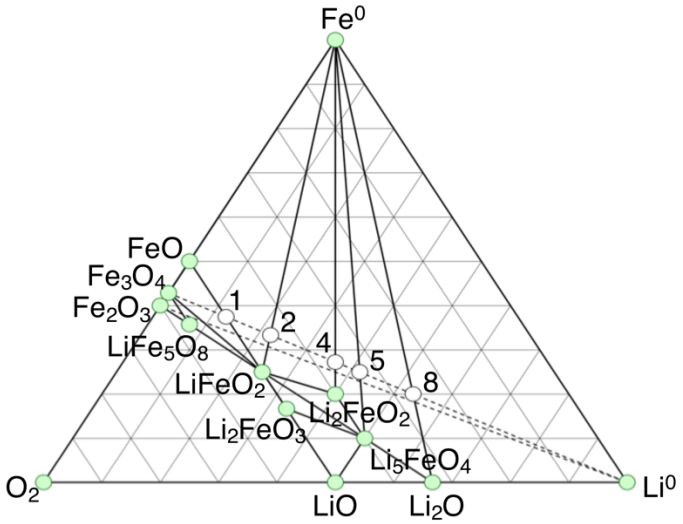

Figure 2.2. Li-Fe-O ternary phase diagram where dashed lines are lithium intercalation lines. The green points are known stable phases, white points and corresponding numbers are reference points for x in $Li_xFe_3O_4$.

Early experiments showed a continuous variation in open circuit voltage starting from about 3 V, with a change in slope near x=1 and finally leveling off to a plateau value of 1 V for x>1.5.[51] Analysis of X-ray diffraction revealed the change to a rock-salt structure noted above. For x>1, this nominally requires Li^+ to occupy sites in addition to 16c, such as 8b or 48f. Even so, evidence pointed to a rock-salt structure for $Li_2Fe_3O_4$ with the possible presence of unreacted spinel Fe_3O_4 regions, although details of the Li ion positions could not be determined.[80,97] Complimentary support was the lack of evidence for Fe^0 formation. Finally, the long plateau for larger x suggested direct conversion to Fe^0 and Li_2O, without evidence for intervening phases.

Subsequent research, including that based on nano-scale magnetite crystallites, agrees on the appearance of the rock-salt structure, although the corresponding range of x varies.[41,44–46,61] Direct experimental evidence for the formation of Fe^0 upon electrochemical

lithiation was achieved through use of a nano-crystalline Fe_3O_4 material.[61] Studies have been performed that address the slow kinetics of the processes occurring during discharge, revealing that magnetite undergoes long relaxation times following lithium insertion, during which parasitic side reactions can occur.[40,84,91] Also, as a function of particle size and discharge rate, multiple reactions can occur simultaneously in a single particle during discharge.[45,98] In particular, real-time transmission electron microscopy, performed at a discharge rate of 0.017 mA/cm^2, clearly shows the coexistence of the different phases in individual, nano-scale particles.[41]

Sample stoichiometry presents an additional complication. Magnetite samples often have some concentration of cation defects depending on synthetic method and oxygen exposure.[32] Iron vacancies specifically, corresponding to $Fe_{3-\delta}O_4$, have been observed, occurring predominantly on the 16d site (in the B-type position), as shown by Mossbauer spectroscopy.[99] The structure of maghemite, γ-Fe_2O_3, presents the logical limit of fully oxidized $Fe_{3-\delta}O_4$ with δ=0.33. The vacancies are generally confined to the 16d site, schematically $(Fe_1^{3+})_{8a}(Fe_{1.67}^{3+}\ \boxdot_{0.33})_{16d}(O_4^{2-})_{32e}$. Maghemite can be formed by topotactic oxidation of magnetite.[100] Maghemite crystals can be prepared in which the vacancies are ordered in a unit cell that is tripled along one of the Cartesian axes of the conventional magnetite cubic cell to form tetragonal unit cell with space group $P4_12_12$.[101,102] This ordering was confirmed in density functional theory (DFT) based studies, which also pointed to minimization of ionic interactions as the basic mechanism.[103]

Lithiation of maghemite, including in nano-crystalline form, has been extensively studied.[82,83,85,89,90,104,105] Overall, the characteristics are similar to magnetite, including long relaxation times following lithium insertion, parasitic side reactions, and improved

electrochemical performance with nano-sizing. For ease of comparison with magnetite, we describe the results with reference to the equivalent formula unit, $Li_xFe_{2.67}O_4$. Pernet, *et al.*, identified a sequence of three reaction on an electrochemical lithiation path ending at $x \sim 1.33$.[82] The first reaction corresponded to the filling of 16d vacancies with lithium, ending at about $x=0.33$. The second reaction, clearly slower, corresponded with clear changes in structure measured by X-ray diffraction, specifically from spinel to rock-salt. At the end of this regime, there was residual tetrahedral Fe and $x \sim 1.15$ indicated that not all 16c sites were occupied. The third reaction, considerably faster, was hypothesized to correspond to filling those residual sites with Li. The parallel with the original Thackeray et al. picture for magnetite is clear. Interestingly, some subsequent investigations of nano-scale materials have suggested a suppression of the transition to the rock-salt structure,[83,90] and observed apparent reversibility in the spinel to rock-salt transition.[85] Other studies showed an irreversible spinel to rock-salt transition.[44,45]

As studies on the lithiation of magnetite progress, the importance of discharge rate on observed mechanism, the observation of slow kinetics of phase change, and mass transport resistances occurring in the material, highlight the importance of separating kinetic from thermodynamic effects. For the initial stages of lithium insertion, a key question controlling the thermodynamic picture is the relative stability of $LiFe_3O_4$. The second question is whether there is finite range of x over which $Li_xFe_3O_4$ forms continuously, an intercalation regime, as suggested by the experimental voltage profiles. Finally, the role of iron vacancies and the extent to which maghemite behaves differently during lithium insertion must be addressed. This is particularly highlighted in nanocrystalline samples. Experiments show that processing conditions may lead to a structure with magnetite core

and an oxidized cladding, Fe^{3+} rich[61] or even specifically maghemite.[106] Overall, fundamental understanding requires open circuit potential data where kinetic factors have been thoroughly characterized so that the regimes of continuous lithium insertion can be distinguished from the plateaus that signal conversion reactions.

In this chapter, the open circuit potential data for magnetite nanocrystalline materials based on slow lithium insertion rates and open circuit potential monitored for up to 30 days is presented. We then present results from an in-depth analysis, using DFT-based calculations, substantially expanding on the scope of structures considered in recent studies.[41,44] We revisit the relative stability of the rock-salt-like $LiFe_3O_4$ phase and the relative stability more generally of $Li_xFe_3O_4$ at low levels of lithiation, $x<1$. We also consider Li insertion into Fe deficient magnetite, $Fe_{2.875}O_4$, and maghemite, $Fe_{2.67}O_4$. Based on calculations for distinct ways to organize Li and Fe ions on the 16c site of rock-salt-like structures for $LiFe_3O_4$ in an eight formula unit cell, we find a series of structures that are stable relative to the convex hull at zero temperature with a continuous variation in energy. We discuss the roles of charge, spin and orbital ordering in our conclusions. Relative to the most stable $LiFe_3O_4$ structure, we found no stable, intermediate phases for $Li_xFe_3O_4$ with $x<1$. The calculations showed that lithium initially inserts into Fe vacancies available on 16d sites, including filling all the available such vacancies in maghemite. The predicted voltage for this process, near 3 V, corresponds well to the initial, low lithium concentration measured open circuit potential. The predicted voltage for the spinel to rock-salt-like structure conversion, near 2 V, aligns with the first plateau in the measured open circuit potential. However, the lithium concentration at which the measured plateau starts is beyond that which can be accounted for simply through Fe vacancies in the sample.

2.3 Results and Discussion

2.3.1 Measured Reversible Potential.

Galvanostatic intermittent titration technique experiments (GITT) at x = 0.2, 0.4, 0.5, 0.6, 0.8, 1.0, 1.5, and 2.0 equivalents of lithium into 8-9 nm Fe_3O_4 nanoparticles resulted in the voltage relaxation curves shown in Figure 2.3 a. It was observed that at low depths of discharge (x = 0.2 and 0.4), the relaxation profiles took 30 days to reach full equilibrium. For more extensive discharge (x = 0.6, 0.8, 1.0, 1.5, and 2.0), ~5 days was sufficient relaxation time. Previous studies have shown that for larger particles, 30 days relaxation time may not be sufficient.[40] In Figure 2.3 b, the reversible potential starts with a concentration dependent region that lasts until x = 0.8 and ranges from 2.8 V down to 1.9 V. Following the concentration dependent intercalation regime, there is a short voltage plateau near x = 1.0 followed by a slight drop in voltage out to x = 2.0. In comparison, the early measurements by Thackeray, et al., were based on shorter equilibration time (24 hours).[38,51] The low concentration reversible potential was similar to that measured here, but the plateau region was less pronounced near x=1 and had a lower voltage.

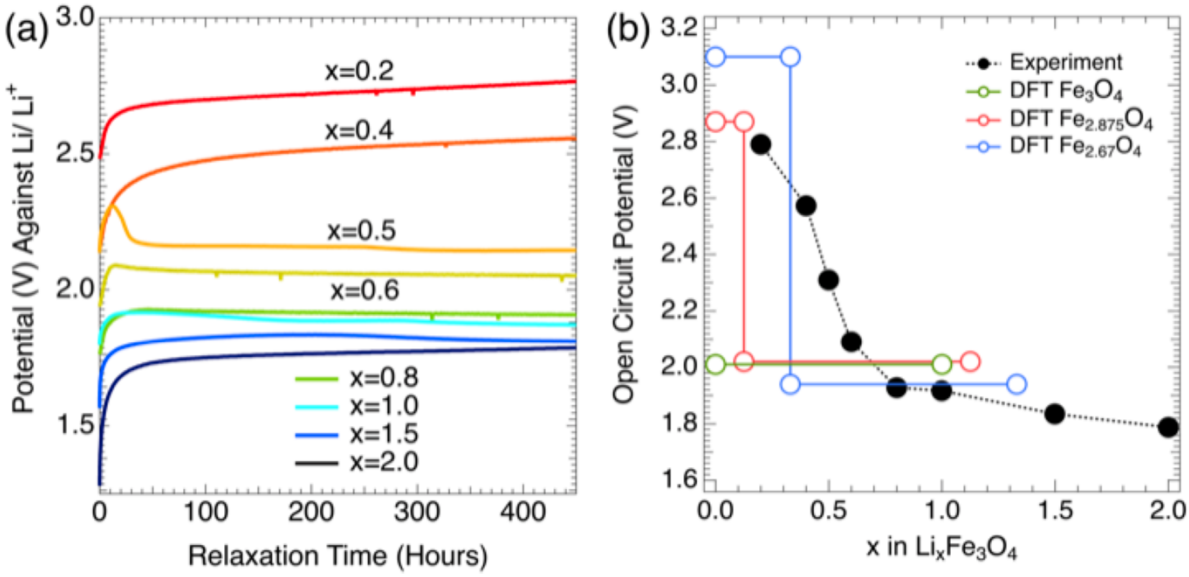

Figure 2.3. a) GITT Voltage relaxation curves for lithiation of 8-9 nm Fe_3O_4 nanoparticles. Maximum Voltage during relaxation is plotted as a function of lithium concentration for the experimental Reversible Potential for $0 < x < 2$ in b). DFT predicted voltage profiles for lithiation of pristine (green), defective magnetite $Fe_{2.875}O_4$ (red), and maghemite $Fe_{2.667}O_4$ (blue) over the experimental Reversible Potential in b).

2.3.2 Structure and Stability of $LiFe_3O_4$.

To establish the $LiFe_3O_4$ high lithium concentration end point, all 97 of the symmetry distinct configurations with 16d comprised entirely of Fe and eight Li and eight Fe occupying the 16c site in an eight formula unit cell have been calculated, representing a defective rocksalt-like structure. Additionally, the one symmetry unique way to compute this same organization in a two formula unit cell was also calculated. The computed energies for both cell sizes are displayed in Figure 2.4 a, with zero taken from the lowest energy configuration. Across the sampled configurations, the energy varied by almost 0.2 eV/f.u. The Madelung Energy for each fully relaxed structure was computed with the charge assigned as the charge that was found self consistently from DFT. In Figure 2.4 b, it can be seen that there is a strong correlation between the electrostatic contribution to the energy and the total energy of the

system. Additionally, this electrostatic contribution has been previously shown as the driving force for vacancy ordering on the 16d site in the related γ-Fe_2O_3 system.[103]

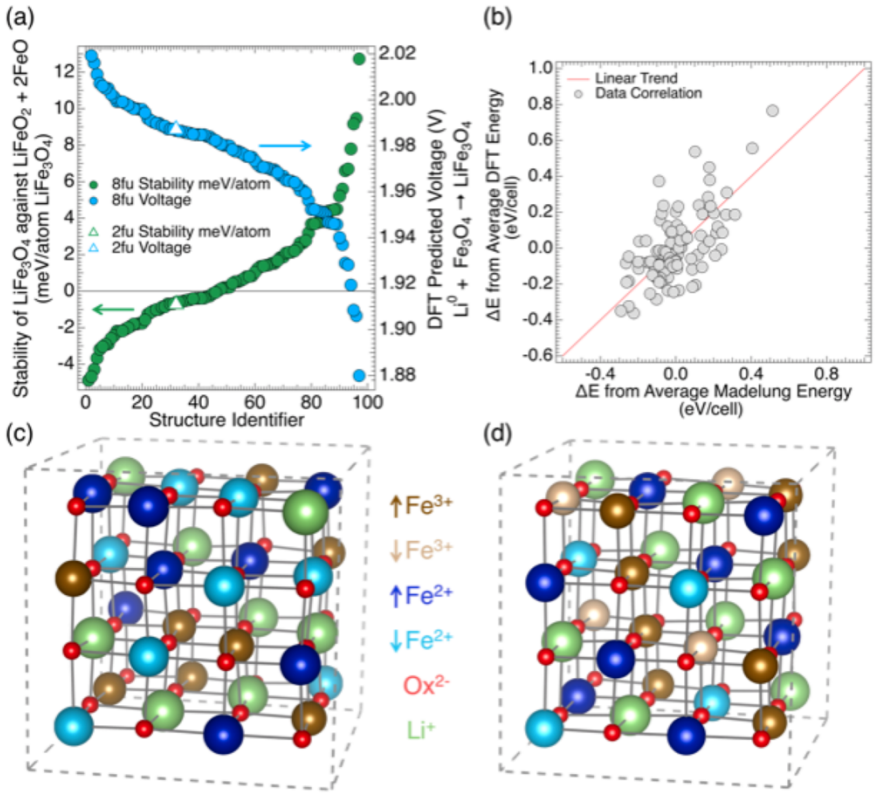

Figure 2.4. (a) Phase stability (left y-axis) of $LiFe_3O_4$ in the rock-salt-like structure for the 97 (one) symmetry distinct configurations of Li and Fe on the 16c site in the eight (two) formula unit cell shown in green circles (green open triangle). The blue symbols (right y-axis) show the corresponding calculated voltage relative to Li metal for the 97 eight formula unit ionic arrangements and the one two formula unit arrangement (blue open triangle). (b) Correlation between the DFT energy of all 97 relaxed $LiFe_3O_4$ ionic arrangements and the Madelung energy of the same relaxed ionic structure. The lowest energy eight formula unit and two formula unit cell are shown in (c) and (d), respectively. Spin up and spin down Fe^{3+} are dark and light brown, respectively. Spin up and spin down Fe^{2+} are dark and light blue, respectively. Lithium is in green and oxygen is in red.

To determine the magnetic ordering of the $LiFe_3O_4$ structure, magnetic exchange interactions were probed by counting the number of first nearest neighbor and second nearest neighbor Heisenberg exchange interactions, represented by the J_1 and J_2 Heisenberg exchange constants for various magnetic orders. In the eight formula unit cell, ferromagnetic, ferrimagnetic, and antiferromagnetic orderings were tested for a handful of ionic

arrangements spanning the full 97 structures. The lowest energy magnetic order was found to be ferrimagnetic in all of the eight formula unit cells tested, where the 8a iron that moved to 16c site maintained spin down and the 16d iron maintained spin up. Antiferromagnetic spin order was found to be most stable in the two formula unit cell by 120 meV/f.u. over the ferrimagnetic order described above in the same cell. The most stable spin structures are shown in Figure 2.4 c and d for the eight f.u. and two f.u. cells, respectively.

It was found that the most stable magnetic structure maximized anti-spin coupling for the second neatest neighbor shell, iron-iron interaction at 180° through neighboring oxygen, corresponding to J_2. For a given ionic arrangement there is more than one way to maximize the second nearest neighbor interaction, however, if the iron at the 16c site are anti-spin coupled to the iron on the 16d site, the J_2 anti-spin coupling is maximized. In the eight formula unit cell, the lowest energy configuration was lower than the one identified from the two formula unit cell, by about 33 meV/f.u. The total magnetic order for the lowest energy $LiFe_3O_4$ was found to be 4.89 μ_B/f.u. The lowest energy eight formula unit structure had no symmetry (P_1), and can be visualized in Figure 2.4 c compared to the higher symmetry two formula unit structure in Figure 2.4 d.

The distribution of energies illustrated in Figure 2.4 a is essentially continuous. The energies for the lowest ten configurations span about 20 meV/Li. While we primarily focus on the zero temperature energy here, we have used the complete sampling of configurations in the eight formula unit cell to make an estimate of the contribution of Li-Fe configuration entropy to the room temperature free energy.[107] The result was 19 meV/Li. For reference, the high temperature limit in the eight formula unit cell can capture 85.3% of the lattice gas analytical result. Additionally, the measured configurational entropy gain for Fe_3O_4 across

the Verwey transition is ~6 J/mol/K,[108] corresponding to 7.6 meV/mol Fe_3O_4 at the 122 K Verwey temperature. The noninteracting lattice gas result for complete disorder of d^5 and d^6 states on 16d site in Fe_3O_4 is 14.5 meV/mol Fe_3O_4 at the Verwey temperature.

With reference to Figure 2.2, the stability of $LiFe_3O_4$ was determined by reference to the formation energies of FeO and $Li_2Fe_2O_4$. The lowest energy structures found for $LiFe_3O_4$ had a computed formation energy that was -5 meV/atom below phase segregation into FeO and $LiFeO_2$, while the two formula unit cell was found to be -1 meV/atom below the hull, as can be seen in Figure 2.4b. This result was independent of the corrections applied more generally to the formation energies across the Li-Fe-O ternary phase diagram, as described Chapter 5.10.

2.3.3 Lithium Insertion into Spinel Fe_3O_4

Using the reference eight formula unit cell, the energy for Li insertion to the 16c, 48f, and 8b, sites was compared, with full atomic and cell shape relaxation in each case. In agreement with previous literature,[42] insertion to the 16c was lowest in energy, followed closely by the 48f site (0.05 eV/Li higher). The energy for the 8b site was considerably higher (2.4 eV/Li), as expected due to the repulsive near neighbor environment (Figure 2.1b).

To investigate the dilute limit of isolated Li insertion, a 16 formula unit cell was also constructed, with focus on the insertion to the 16c site. The computed energy gain, relative to metallic Li, was -0.70 eV/Li, similar to the result at a concentration of x=0.125 found with the eight formula unit cell (-1.01 eV/Li). The lowest energy structures for x=0.0625 and 0.125 are shown in Figure 2.5 a and b respectively. The local motif, clearly shows substantial displacement of one of the neighboring Fe^{3+} cations from its 8a site. While the displacement

is generally in the direction of the available empty 16c site. In the ideal *x*=0.0 lattice, the vacant 16c site where lithium inserts is equidistant from two 8a irons, at 1.81 Å from the 8a to the 16c site. The line connecting the two 8a sites and the vacant 16c site is 179.11°, for Fe_{8a}-$Vacant_{16c}$-Fe_{8a}. After lithium insertion, the two Li-Fe_{8a} distances are 2.39 Å (8a*) and 2.48 Å (8a**). The iron labeled 8a* has been displaced toward a vacant 16c site, moving 1.25 Å from its position in the *x*=0.0 lattice, while the other, 8a**, displaces by only 0.15 Å from its original *x*=0.0 8a site. However, the Li inserted on the 16c site moves 0.59 Å from the high symmetry 16c site, off the high symmetry Fe_{8a}-$Vacant_{16c}$-Fe_{8a} line (179.11°) to an angle of 132.13° for Fe_{8a}-Li_{16c}-Fe_{8a}. With these structural changes, the distance between 8a* and 8a** has gone from 3.62 Å in the *x*=0.0 lattice to 4.50 Å in the *x*=0.0625 lattice.

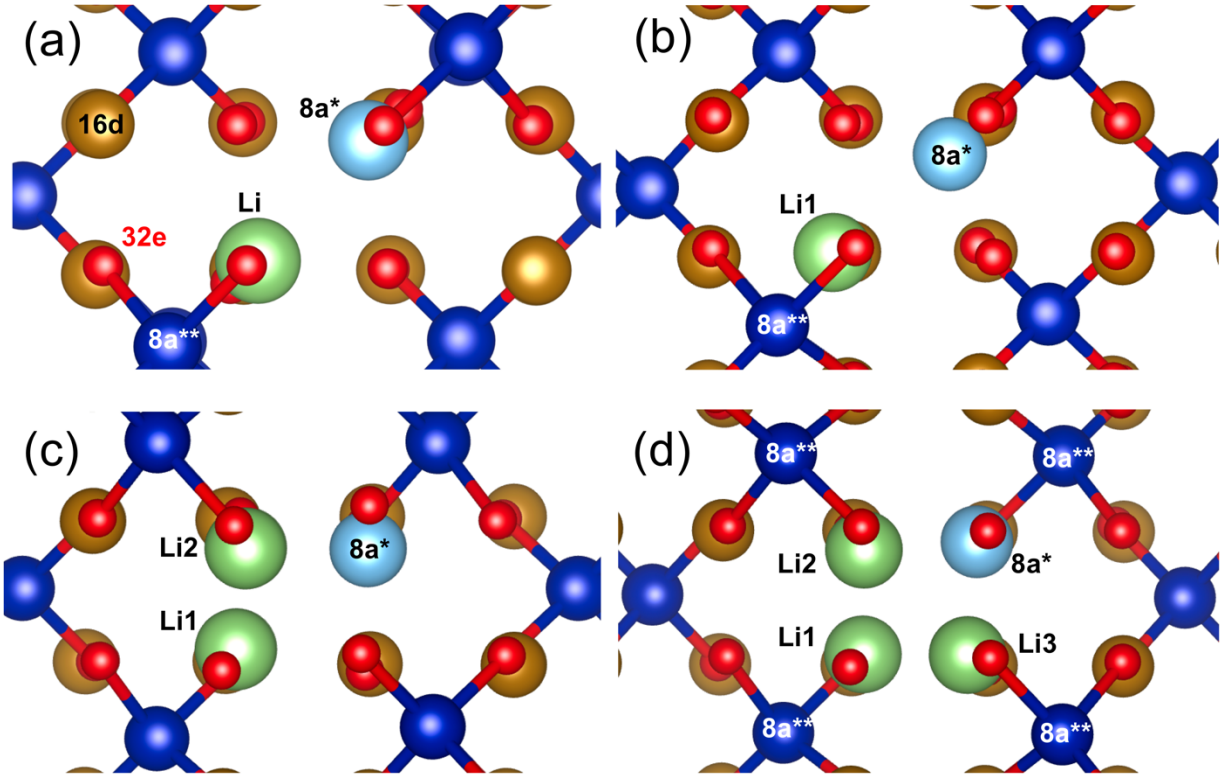

Figure 2.5. Lowest energy structures for (a) $Li_{0.0625}Fe_3O_4$, (b) $Li_{0.125}Fe_3O_4$, (c) $Li_{0.25}Fe_3O_4$, and (d) $Li_{0.375}Fe_3O_4$. Brown atoms are Fe_{16d}, red atoms are oxygen at 32e, dark blue atoms are Fe_{8a}, green

atoms are lithium inserted at 16c site, light blue atoms are Fe_{8a} that have been displaced due to proximal Li_{16c}.

For x=0.125 the Li-8a* distance is 2.45 Å and the Li-8a** distance is 2.42 Å, while in x=0.0625 these distances were 2.38Å and 2.48 Å, respectively. The Li displaces off the high symmetry 16c position by 0.52 Å in x=0.125 and 0.59 Å in x=0.0625. The angle of displacement for Fe_{8a}-Li_{16c}-Fe_{8a} in x=0.125 is 132.09°, while in x=0.0625, it is 135.13°. The 8a*-8a** distance is 4.45 Å for x=0.125, while it was 4.50 Å for x=0.0625. However, between the two dilute concentrations, x=0.0625 and x=0.125, there are also differences in the details of the local motif. The Fe labeled 8a* and 8a** displace from the 8a positions in the x=0.0 structure by 0.79 Å and 0.40 Å in x=0.125 but for x=0.0625, these displacements are more asymmetric. Where for x=0.0625 8a* displaced by 1.25 Å and 8a** 0.15 Å. In the x=0.125 case, the local motif is not isolated due to the supercell used. In the first coordination shell for Li-Fe_{8a}, comprised of 8a* and 8a** the average displacements for x=0.125 and 0.0625 are 0.70 Å and 0.60 Å, respectively. The displacement for the second Li-Fe_{8a} coordination shell, comprised of 6 additional Fe_{8a}'s, is 0.10 Å for x=0.125 and 0.06 Å for x=0.0625. In the case of x=0.125, the 3rd Li-Fe_{8a} coordination shell contains no new Fe_{8a}'s, as there are 8 in the supercell and all 8 have been accounted for in the first and second coordination shells. For x=0.125, the average displacement in the 3rd coordination shell is 0.11 Å, where for x=0.0625, with all unique Fe_{8a}'s, it is only 0.03 Å.

All symmetry distinct configurations for addition of two and three Li atoms, x=0.25 and x=0.375, respectively, to 16c sites in the eight formula unit spinel structure cell were investigated. Figure 2.5c and d illustrate the lowest energy structures found. The results clearly demonstrate clustering of the added Li atoms in this regime. With reference to Figure 2.1, each 8a site has four vacant 16c site nearest neighbors. As shown in Figure 2.5b, the first

inserted Li, Li1, on one of the vacant 16c sites leads to displacement of the proximal tetrahedral 8a Fe, 8a*, towards a second one of the vacant 16c sites, and this displacement costs energy. There are two remaining empty 16c sites in the local motif seen in Figure 2.5b. As illustrated in Figure 2.5c, the lowest energy site for addition of another lithium, Li2, is adjacent to Li1, where the two Li atoms can share the energy cost of the displacement of the tetrahedral 8a* Fe. A third added lithium, Li3, to the eight formula unit cell preferentially goes onto the final vacant 16c site adjacent to Li1 and Li2 and the displaced 8a* Fe (Figure 2.5d). Qualitatively, the local 8a* Fe cation displaces further with each added Li, approaching the 16c site for three neighboring Li atoms. The energy gain per lithium added is -0.70 eV/Li, -1.01 eV/Li, -1.13 eV/Li, and -1.30 eV/Li for x=0.0625, 0.125, 0.25, and 0.375 illustrated structurally in Figure 2.5a, b, c, and d. The distance of the displaced Fe 8a* to the vacant 16c site is 0.84 Å, 0.62 Å, and 0.34 Å at x=0.125, 0.25, and 0.375 (Figure 2.5b, c, and d). Illustrating how the increasing concentrations of lithium cooperatively push the iron into the 16c site. This cooperative force is maximized at x=0.375, as all the available local 16c sites in this motif have been exhausted.

We observe that as the displaced 8a* Fe approaches the 16c site, it is now in close proximity to an adjacent 8a tetrahedral iron, labeled 8a** in Figure 2.5d. This causes further displacements of 8a** Fe, each 8a** is displaced by RMSD of 0.02 Å from the x=0.0 fully relaxed structure. However, the cooperative displacement of all of the 8a Fe atoms in the structure to 16c sites previously hypothesized in the literature and discussed in the introduction, has not yet occurred. In fact, explicit calculations of configurations at x=0.375, based on the rock-salt structure, discussed further in Section 3.4, show that the local cluster configuration identified in Figure 2.5d is in fact lowest in energy at x=0.375. The lowest

energy motif based on insertion of an additional lithium into an eight formula unit cell, x=0.5, starting from spinel still showed clustering, but now with four Li atoms around two displaced Fe atoms from 8a sites. However, competing with this were x=0.5 configurations with full conversion of all tetrahedral irons to 16c sites and lithium at 16c sites dispersed throughout the structure, which were found to be lower in energy than the clustering. It is found that lithium clustering around and displacing Fe^{3+} from the 8a site to Fe^{2+} at the 16c site is energetically favored up to a concentration of x=0.375, or 3 Li^{+} in an eight formula unit cell.

2.3.4 Lithium Insertion into Defective Rocksalt Fe_3O_4

As discussed in Chapter 2.3.2, all symmetry unique configurations at x=1.0 with full occupation of Fe on 16d and 50:50 Li:Fe on 16c were calculated. The lowest energy structure was low symmetry, P_1, and it is visualized in Figure 2.4 c. This lowest energy parent structure was used to create Li vacancies, enabling the analysis of the defective rocksalt structure for $Li_xFe_3O_4$ with $0.125 < x < 0.875$. In the dilute limit, Thackeray et al.'s hypothesis of cooperative displacement was tested for x=0.125. The lowest energy cooperative displacement structure was 0.56 eV/f.u. higher in energy than a lithium at the 16c site in the inverse spinel structure, eliminating the possibility of a cooperative displacement at x=0.125. For x=0.25 and 0.375, the lithium clustering and displacement of a tetrahedral iron is lowest in energy, but at x=0.5, movement of all tetrahedral iron to 16c sites with lithium also on the 16c sites is 55.62 meV/f.u. lower in energy than lithium clustering. Indicating that cooperative displacement to defective rocksalt is energetically competitive at x=0.5.

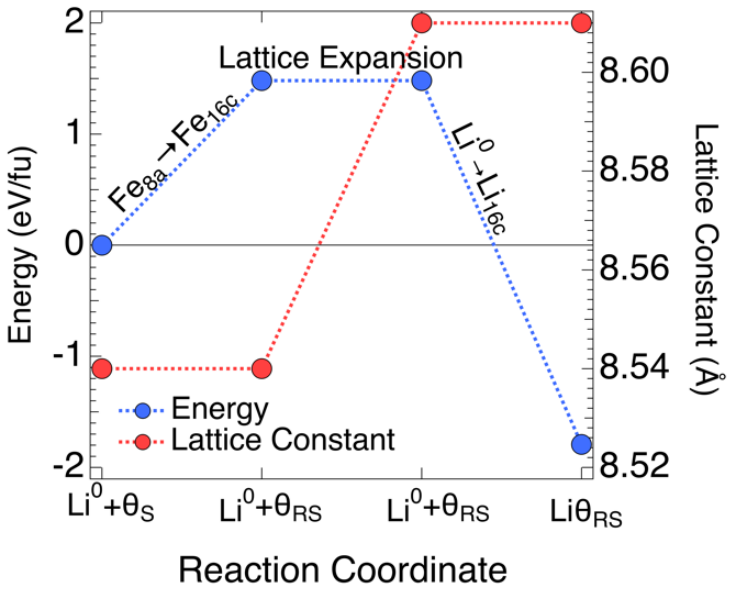

Figure 2.6. Stepwise energetic contributions for movement of tetrahedral 8a iron in x=0.0 inverse spinel, θ_S, to 16c sites to make defective rock-salt, θ_{RS}, at fixed volume. Energy to expand lattice to x=1.0 lattice constant, and energy gain upon lithium insertion, $Li\theta_{RS}$. All calculations are in a two formula unit cell.

To further investigate the competition between the observed low concentration lithium clustering effect versus the conversion of all 8a iron to vacant 16c sites observed at high lithium concentrations, the energy to displace all tetrahedral 8a iron from the inverse spinel structure to the 16c sites in the defective rocksalt structure was calculated in a two formula unit cell. The first step in is the movement of all 8a iron to 16c sites with no change in lattice parameter from the x=0.0 structure but allowed relaxation of internal coordinates (Figure 2.6). This is the energy cost to displace the iron from 8a to 16c and was found to be +1.48 eV/f.u. Second, the structure was expanded to the final x=1.0 lattice parameter, representing the energetic cost of lattice expansion. From Figure 2.6, it is seen that the lattice expansion contributes negligibly to the energetic cost, the majority of the energetic cost comes from the displacement of the tetrahedral irons to octahedral 16c sites. The third step

is the energetic gain associated with lithium insertion into the defective rocksalt structure, which was found to be -1.80 eV/f.u from the starting structure.

2.3.5 $Li_xFe_3O_4$ Convex Hull.

Referring to Figure 2.2, the relative stability of Li intercalated magnetite should generally be determined relative to the corners of the Gibbs triangle consisting of FeO, Fe_3O_4 and $Li_2Fe_2O_4$. Our calculations suggest that $LiFe_3O_4$ is just below the convex hull and it is representative of rock-salt-like structures in the Li-Fe phase diagram. This suggests that $LiFe_3O_4$ is a thermodynamically stable compound. It is therefore interesting to probe whether the early stages of lithium insertion into spinel, with the cluster effects noted in Sect. 3.2, form a continuously stable regime, or if they are unstable against phase segregation into $LiFe_3O_4$. To assess this, a one-dimensional convex hull has been computed with Fe_3O_4 and $LiFe_3O_4$ as the end points.

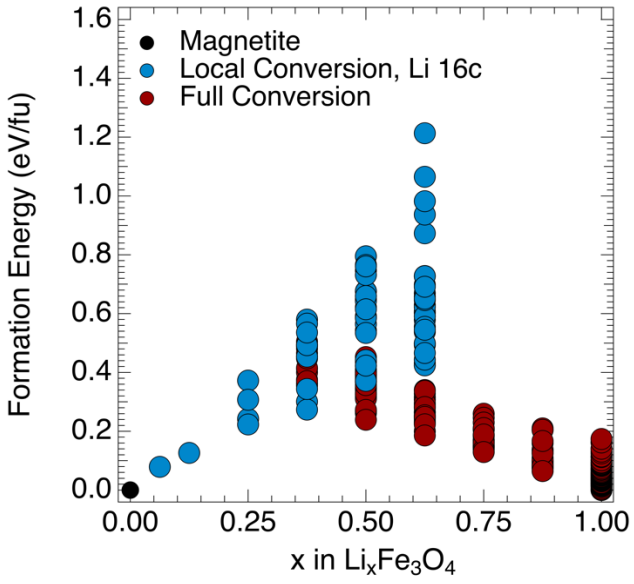

Figure 2.7. Convex-Hull for lithium insertion into Fe_3O_4 for $0 \le x \le 1$. All symmetry distinct configurations were sampled for insertion into the 16c site of the spinel phase up to x=0.625. Full Conversion represents a defective rocksalt structure for which Li from x=0.125 to 0.875 was sampled

(red circles). Multiple configurations exist for the organization of Fe on the 16c sites to create the defective rocksalt structure, the details of which can be seen in Chapter 5.6.

The comprehensive results for Li insertion in the range $0 \leq x \leq 1$ are summarized in Figure 2.7. From the lowest concentration probed here (x=0.0625), no insertion compound is found to be stable. As discussed above (Chapter 2.3.3), this traces back to the strong Coulomb repulsion between the inserted Li and the Fe cation on the 8a site. The energy cost to displace Fe8a is simply too high. Even though the results for low concentration do show a stable local motif with up to three Li atoms around a single displaced Fe8a (Figure 2.5 d) in the spinel structure, this motif is not found to be stable against phase segregation to form the rock-salt-like phase and unlithiated magnetite. Li deficient ($0.5 < x < 0.875$) rock-salt compounds are found to be unstable against formation of the fully occupied rock-salt-like phase. Now, as noted in the previous section, the $LiFe_3O_4$ end point considered here is stable against phase segregation to FeO + $\alpha -LiFeO_2$ by around -5 meV/atom. This phase stability is low and at room temperature, FeO + $\alpha -LiFeO_2$ may also form. Interestingly, either result, $LiFe_3O_4$ or FeO + $\alpha -LiFeO_2$, is fully consistent with the widely observed formation of rock-salt-like structure, particularly when it is taken into account that typical X-ray measurements are not sensitive to the specific location of Li in the sample.

2.3.6 Impact of Iron Vacancies on Lithium Insertion***.***

The site preference for a nominally isolated Fe vacancy was tested in an eight formula unit cell and, in agreement with experiment,[99] a Fe vacancy on the 16d site was found to be energetically preferred over a vacancy on the 8a site, by 1.1 eV/defect. In the case of defective magnetite, $Fe_{2.875}O_4$, the charge distribution among the 15 occupied 16d sites was the expected ten Fe^{3+} and five Fe^{2+}, with the eight Fe^{3+} on the tetrahedral 8a sites unaffected by

the presence of the 16d defect. Individual iron magnetic moments were largely unaffected, but the net magnetic moment was reduced to 3.70 μ_b per f.u. for $Fe_{2.875}O_4$. For maghemite, $Fe_{2.67}O_4$, all cation sites were Fe^{3+}, as expected and the net magnetic moment was further reduced to 3.29 μ_b per f.u., compared to the experimentally bulk value of 2.83 μ_b per f.u.[109–111]

In an iron deficient magnetite structure, lithium insertion to the 16d site of a missing Fe competes with the interstitial sites previously examined for pristine magnetite (16c, 8b, or 48f). Computations for insertion of lithium into $Fe_{2.875}O_4$ in the standard eight formula unit cell showed that lithium insertion was most stable on the 16d iron vacancy defect, by 38 meV/Li over insertion at a vacant 16c site. As shown in Figure 2.8 a, all atoms in the lattice remained undisturbed in the presence of the 16d Li. Adding another lithium atom, it was found that the lowest energy configuration was a split interstitial motif in which the two lithiums share the available 16d site. Alternative structures, in which the second Li atom went to a more remote interstitial site resulted in the same type of local motif as illustrated in Figure 2.5 b, with the added cost of local displacement of the neighboring 8a site Fe atom and were therefore less stable than the split interstitial.

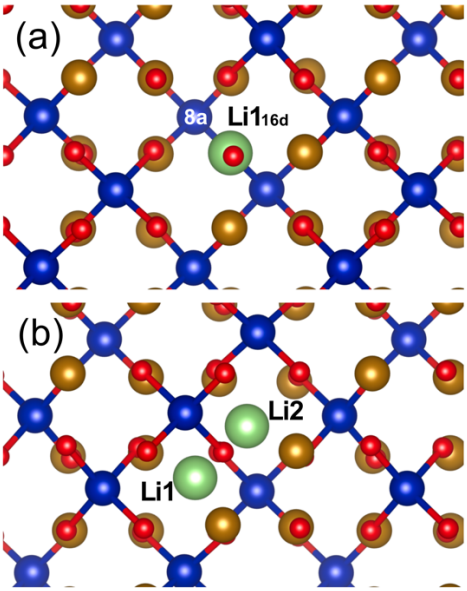

Figure 2.8. Lowest energy structures for lithium insertion into $Fe_{2.875}O_4$ with the iron defect on a 16d site. Lithium insertion onto the 16d defect a) x=0.125 and split interstitial of the 16d defect b) x=0.25. All calculations were performed in eight formula unit cell. Brown atoms are Fe_{16d}, red atoms are oxygen at 32e, dark blue atoms are Fe_{8a}, green atoms are lithium inserted at 16d site.

To test stability of $Li_xFe_{2.875}O_4$ structures against phase segregation, the analysis used for the ideal magnetite case was extended. Specifically, the end-point $Li_{1.125}Fe_{2.875}O_4$ was characterized as follows. With a composition on the FeO to $LiFeO_2$ tie line in the ternary phase diagram neighboring to $LiFe_3O_4$, a constrained search of configurations was done starting from the previously determined lowest energy P_1 structure for $LiFe_3O_4$. All 16 symmetry distinct ways to substitute a lithium for iron on a 16d were considered and the lowest energy structure was taken to represent $Li_{1.125}Fe_{2.875}O_4$. The 16 calculations are shown in Figure 2.9 a and the lowest energy structure is visualized in Appendix 4. In addition to restrictions derived from the specific organization of Fe and Li on the 16c site, this search also excludes more extensive iron and lithium redistribution over the 16c + 16d sites. While the constrained search may not have revealed the most energetically favorable end-point, the calculated formation energy is still -4.6 meV/atom below the computed FeO to α $-LiFeO_2$

tie line, similar to the $LiFe_3O_4$ stability of -4.9 meV/atom. Using it as an end point to form a convex hull to examine lithium insertion into $Fe_{2.875}O_4$, the formation energies shown in Figure 2.9 a show that a single lithium atom on the available defect site is a stable intercalate. However, lithium insertion on the 16c site is unstable and the x = 0.25 split interstitial motif is already unstable against phase segregation. This further exemplifies the strong Coulomb repulsion between the 16c site and the 8a site occupied by iron that destabilized insertion into pristine or defective spinel.

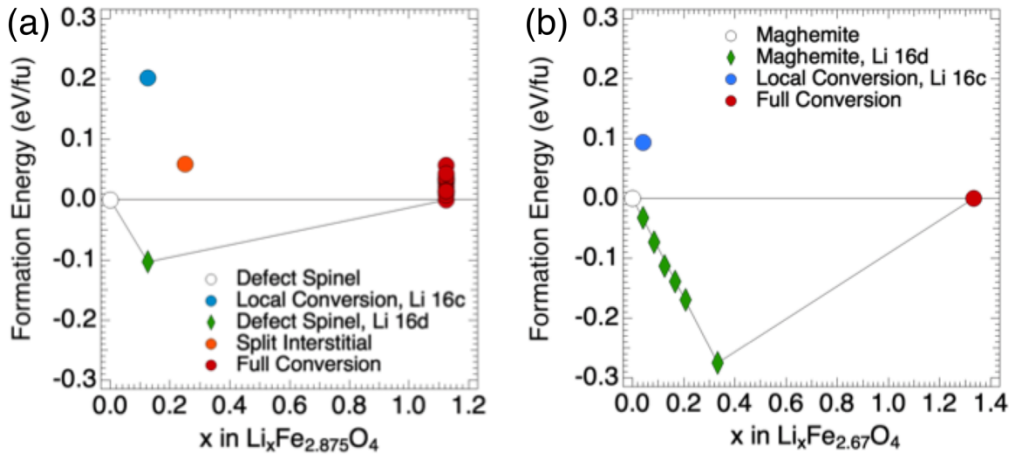

Figure 2.9. Convex-Hull for lithium insertion into (a) $Fe_{2.875}O_4$ and (b) $Fe_{2.667}O_4$.

The highest concentrations of 16d iron defects observed in magnetite is x=0.33, occurring in maghemite, γ-$Fe_{2.67}O_4$. Following the same trend as in defective magnetite, $Li_xFe_{2.875}O_4$, lithium insertion onto 16d sites up to the concentration of the defects result in stable intercalated structures into γ-$Fe_{2.67}O_4$, where there were no structural rearrangements of the parent γ-$Fe_{2.67}O_4$ in the presence of the 16d intercalated lithium. The supercell for γ-$Fe_{2.67}O_4$ is 24 formula units, too large to enumerate all possible orderings of Li+ Fe on the 16c sites as was done for $LiFe_3O_4$ and in a constrained way for $Li_{1.125}Fe_{2.875}O_4$, as such, concentrations between $0.33 < x < 1.33$ were not sampled. However, due to the

knowledge gained from the $Li_xFe_3O_4$ and $Li_xFe_{2.875}O_4$ structures, insertion of lithium past the concentration of defects will likely result in Coulombic repulsions and instability with respect to the rocksalt end point, $Li_{1.33}Fe_{2.67}O_4$. Due to computational cost, only one structure for the $Li_{1.33}Fe_{2.67}O_4$ end point was calculated. This structure was characterized by maintaining the defect order on the 16d site according to $P4_12_12$ order found to be most stable by Grau-Crespo *et al.*[103] and the Li+Fe on the 16c site was set as visualized in Appendix 4. The $Li_{1.33}Fe_{2.67}O_4$ phase calculated was found to be 8 meV/atom above the tie line to phase segregation to FeO to α-$LiFeO_2$, and as will be discussed in the next section, has a DFT predicted voltage comparable to experiment.

2.3.7 Open Circuit Potential.

Due to instability of lithium insertion past the concentration of Fe defects on the 16d site, lithium insertion greater than x = 0.125 in $Li_xFe_{2.875}O_4$ and greater than x=0.33 in $Li_xFe_{2.67}O_4$ results in the prediction of two-phases in equilibrium. For defective magnetite, $Li_{0.125}Fe_{2.875}O_4$ and $Li_{1.125}Fe_{2.875}O_4$ are the two phases in equilibrium and for maghemite, $Li_{0.33}Fe_{2.67}O_4$ and $Li_{1.33}Fe_{2.67}O_4$ are the two phases in equilibrium. Analogously, lithium insertion into Fe_3O_4, with the 16d site fully occupied by Fe, results in a two-phase equilibrium between Fe_3O_4 and $LiFe_3O_4$. The DFT+U predicted voltages of the two-phase equilibria for lithium insertion into Fe_3O_4, $Fe_{2.875}O_4$, and $Fe_{2.67}O_4$ can be seen in Figure 2.3 b.

Although the Convex-Hull stability analysis predicts that lithium insertion into magnetite will phase segregate into Fe_3O_4 and Li Fe_3O_4, an analysis of the DFT predicted voltages for the Li-clustering motifs in Figure 2.5 gives insight into if these motifs occur or are metastable. For the x=0.375, 3 Li-clustering depicted in Figure 2.5 d, the DFT predicted

voltage is 1.30 V, while the experimentally observed voltage at x=0.375 is ~2.6 V. Similarly, for x=0.125, the DFT voltage is 1.01 V, while the experimentally observed voltage is ~2.8 V. Due to such a large discrepancy between the predicted voltage for the local lithium clustering motif and the experimentally observed voltage, it is unlikely that these structures contribute to the experimentally observed reversible potential.

From the experimental data in Figure 2.3b, it is observed that the reversible potential for lithiation of 8-9 nm Fe_3O_4 nanoparticles initiates with an intercalation regime from 2.8-1.8 V, followed by a two-phase voltage plateau at around 1.8 V. When 16d defects occur in the material, as in the case of $Fe_{2.875}O_4$ and $Fe_{2.67}O_4$, lithiation into these defects results in stable intercalates, there are no substantial structural rearrangements of the spinel background, and the intercalate is energetically favored against phase segregation. The DFT+U predicted voltages for 16d defect filling by lithium is 2.87-3.01 V, consistent with the experimental voltage range for early lithiation into the 8-9 nm particles reported in Figure 2.3b and shown in the green shaded region in Figure 2.10. Once all 16d defects are filled, additional lithium must insert onto 16c sites, and due to their proximity to iron on 8a sites, this causes Coulombic repulsion and the resultant intercalates are unstable against phase segregation. Further lithiation past the concentration of 16d Fe defects, results in phase segregation at a DFT+U predicted voltage of 1.89-2.02 V, consistent with the first experimental voltage plateau in Figure 2.3b.

2.4 Conclusions.

The stability analysis for lithium insertion into Fe_3O_4, $Fe_{2.875}O_4$, and γ-$Fe_{2.67}O_4$ is summarized in Figure 2.10, a zoom-in on the pertinent region of the Li-Fe-O ternary phase

diagram from Figure 2.2. In Figure 2.10, all structures that were found to be within room temperature k_BT, 24 meV/atom, of a tie-line are in yellow, while structures higher than 24 meV/atom above the corresponding tie line are in red. The known stable phases are in green. The line connecting FeO to $LiFeO_2$ represents a string of defective rocksalt structures, where Li is substituting for Fe on 16c ($LiFe_3O_4$) or 16c + 16d sites ($Li_{1.125}Fe_3O_4$, γ-$Li_{1.33}Fe_{2.67}O_4$, $LiFeO_2$). The line connecting Fe_3O_4 to $LiFe_5O_8$ represents the string of spinel structures with $(Fe)_{8a}[Li_\delta Fe_{2-\delta}]_{16d}[O_4]_{32e}$, where the concentration of Li is equal to the concentration of Fe defects on the 16d site. The structures on the spinel tie line, Fe_3O_4, $Li_{0.125}Fe_{2.875}O_4$, and γ-$Li_{0.33}Fe_{2.67}O_4$, have the 8a site fully occupied by Fe and the 16d site fully occupied by $\delta Li + (2-\delta)Fe$, therefore, further lithiation results in Li insertion on vacant 16c sites. Here we show that due to the proximity of the 16c site to the 8a site occupied by Fe, lithiation of structures on the Fe_3O_4 to $LiFe_5O_8$ tie lie is unstable against phase segregation to the corresponding rocksalt-like endpoint on the FeO to $LiFeO_2$ tie line, while voltages for these phase transitions from spinel to defective rocksalt are ~2.0 V. Lithiation of the 16d defects in the structures on the spinel tie lie, Fe_3O_4 to $LiFe_5O_8$, is stable and results in voltages around ~3.0 V.

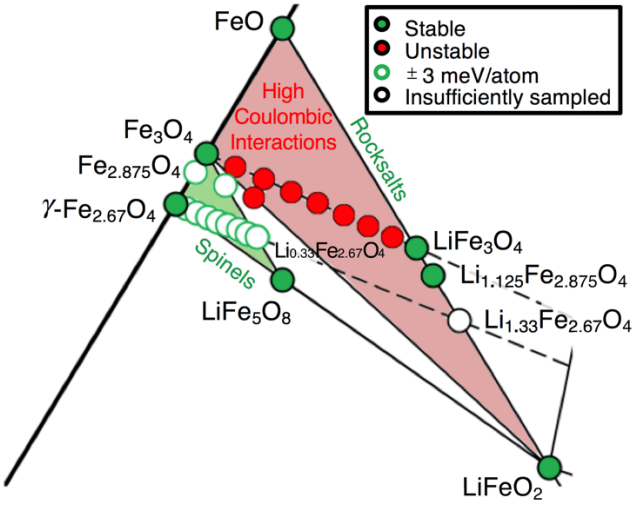

Figure 2.10. Zoom in on Li-Fe-O ternary phase diagram with DFT+U stability assessment of lithiation of Fe_3O_4, $Fe_{2.875}O_4$, and $Fe_{2.667}O_4$.

The $LiFe_3O_4$ phase is predicted to be stable against phase segregation to $LiFeO_2$ + 2FeO by ~5 meV/atom here. We note that we have not fully explored the complex issue of orbital ordering or magnetic configuration in the $LiFe_3O_4$ structure for all Li-Fe configurations, as this is a computationally large problem and our studies indicate this energy scale to be small compared to charge ordering. However, additional analysis and reporting of a lower energy orbital or magnetic configuration will only further enhance the stability prediction for $LiFe_3O_4$ due to the variational principle. Similarly, the energy scale for charge and orbital ordering in the Fe_3O_4 structure is small compared to internal relaxations. For a (Li)Fe_3O_4 ground state structure with a lower energy than that found herein, the $Li_xFe_3O_4$ intercalates are further destabilized against phase segregation to $LiFe_3O_4$ + Fe_3O_4, reinforcing the finding that lithiation onto 16c sites in Fe_3O_4 is predicted unstable.

Magnetite is known to have Fe defects on the 16d sites, the highest concentration of defects observed while maintaining the spinel structure is x=0.33 in maghemite, γ-$Fe_{2.67}O_4$.

Lithium insertion onto these 16d defects is found to be stable against phase segregation. In a particle comprised of pure γ-$Fe_{2.67}O_4$ the highest x for which the intercalation regime lasts would be the concentration of defects, $x = 0.33$. From the experimental open circuit voltage in Figure 2.3 b, the intercalation regime lasts until $x \sim 0.8$. This indicates that there are likely other mechanisms by which intercalation proceeds in the nanoparticles. Further investigation into the chemistry and termination of particle surfaces, the interaction between pristine and iron defective regions of the particles, iron extrusion, and side reactions are all possible culprits for continued intercalation. However, from theoretical investigation of the thermodynamics of lithium insertion into magnetite, defective magnetite, and maghemite, it becomes evident that the 16d Fe vacancy defects Fe_3O_4 play a large role in the open circuit potential for lithium insertion into magnetite, which will be explored in the following Chapter.

CHAPTER 3: THE CATION DEFECT MEDIATED SIZE DEPENDENCE OF THE REVERSIBLE POTENTIAL FOR IRON-OXIDE NANOPARTICLES[3]

3.1 Chapter Overview

The reversible potential for 9 nm and 25 nm magnetite nanoparticles is studied at low lithium concentrations, and a particle size dependence is observed in the resultant voltage profiles. Smaller 9 nm particles are observed to have a larger intercalation regime compared to larger 25 nm particles. The O K edges and $L_{2,3}$ edges of electron energy loss spectroscopy show evidence for increased iron oxidation at the surface of a Fe_3O_4 nanoparticle compared to the core. Neutron diffraction indicates that Fe_3O_4 nanoparticles show off-stoichiometry, with smaller 9 nm particles having lower Fe_{16d} occupation than 25 nm particles. DFT+U calculated voltage profiles are able to capture the size dependence observed in the reversible potential when the nanoparticles are treated as a superposition of a stoichiometric Fe_3O_4 core with an oxidized $\gamma - Fe_2O_3$ shell at the surface. We show that the cationic defects observed in the Fe_3O_4 nanoparticles are a function of nanoparticle size and that the defect concentrations in these particles have implications on the lithium intercalation behavior and structural characteristics of the iron oxide nanoparticles.

[3] This chapter presents work that was done in collaboration with: Andrea M. Bruck, Christina A. Cama, Xiaobing Hu, Kenneth J. Takeuchi, Yimei Zhu, Amy C. Marschilok, Esther S. Takeuchi, Mark S. Hybertsen, Alan C. West

3.2 Introduction to the Effects of Nanostructuring in Magnetite

Nanostructuring brings the interfacial properties of a material to the forefront of its performance.[19,112] Iron-oxide nanoparticles are known to show off-stoichiometry, and a surface defect region or surface restructuring is commonly observed.[100,113,114] The stoichiometry in both bulk and nanoparticulate magnetite can range from perfectly stoichiometric Fe_3O_4, $(Fe^{3+})_{8a}[Fe^{3+}Fe^{2+}]_{16d}O_4$, to fully oxidized $\gamma - Fe_2O_3$, $(Fe^{3+})_{8a}[Fe^{3+}_{1.67}\ \boxdot_{0.33}]_{16d}O_4$, while maintaining the inverse spinel structure. The perseverance of the inverse spinel structure in defective magnetite can inhibit precise quantification of structural defects. EXAFS has previously been leveraged to characterize the average oxidation state of iron in Fe_3O_4 nanoparticles where It was found that in nanoparticulate magnetite, the average oxidation state for iron deviates from $Fe^{2.67+}$, the value for perfectly stoichiometric material, $(Fe^{3+})[Fe^{3+}Fe^{2+}]O_4$, and higher Fe^{3+} enrichment was observed in smaller nanoparticles over larger ones.[114] Here we examine structural characteristics of magnetite as a function of nanoparticle size with XRD, EELS, and Neutron Diffraction studies. Additionally, we examine how the electrochemical behavior and structure of the particles changes with lithiation. The observed dependence on particle size is the result of smaller particles having a larger volume fraction of defects.

3.3 Variation in Defect Concentration as a Function of Nanoparticle Size

Neutron Diffraction measurements of lattice constants for 10 nm and 30 nm Fe_3O_4 particles are found to be 8.3756(2) Å and 8.4007(2) Å. The pure phase lattice constant for Fe_3O_4 is 8.398(6) Å and for γ-$Fe_{2.67}O_4$ is 8.3419 Å.[115] The best fit occupancy on the 16d site was found as 0.93(1) and 0.96(7) for the 10 nm and 30 nm particles, respectively. The final stoichiometry for the 10 nm and 30 nm particles was found to be $Fe_{2.82}O_4$ and $Fe_{2.93}O_4$,

respectively, consistent with Fe_3O_4 nanoparticles that have a 1.2 nm region of the 16d cation defective spinel γ-$Fe_{2.67}O_4$ at the surface of the particle, where the penetration depth of the defective spinel phase is constant for both the 10 nm and 30 nm particles. Due to the effects of the increased surface area to volume ratio in nanoparticles, a 1.2 nm defective region accounts for 56.1% of the 10 nm particle and 22.1% of the 30 nm particle by volume.

3.4 EELS Evidence for Fe_3O_4 Surface Oxidation

Electron energy loss spectroscopy (EELS) has been shown to be useful in deciphering oxidation states in metal-oxides.[116] In Figure 3.1 f, the O K edges are shown for a 60 nm Fe_3O_4 particle at 3 nm into the sample (red) and 45 nm into the sample (blue) as depicted in Figure 3.1 a and b. The ionization edges from EELS experiments can be dependent on the crystal orientation, here the crystal was oriented along the <110> direction for the scan as indicated in Figure 3.1 a, results are also shown in Appendix 6 for a random orientation. The losses in the low energy loss region, Figure 3.1 c, are associated with valence electron excitations, interband, and collective plasmon modes.[117] The loss labeled Fe $M_{2/3}$ in Figure 3.1e at ~55 eV is the characteristic iron-oxide excitation of 3p iron electrons to unoccupied d states. Additionally, there is a shift of the plasmon peak of approximately 2.75 eV, where the 3 nm depth has a decreased energy loss over the 45 nm depth.

The O K edges of iron oxides have a pre-peak that is attributed to the Fe 3*d* and O 2*p* hybridization, and splitting here is normally attributed to t_{2g} and e_g states and is characteristic of hematite in the sample.[118,119] The second loss region for O K, typically 5-10 eV above the Fe 3*d* pre-peak, can be attributed to Fe 4*s* and 4*p* hybridization with O 2*p*. The intensity of the Fe 3*d* pre-peak with respect to the 4*sp* band is known to vary with oxygen connectivity, specifically a pre-peak intensity decrease indicating iron reduction.[120,121] In

Figure 3.1 d, the O K pre-peak at 3 nm into the sample is at a higher intensity than that at 45 nm into the sample with respect to their respective 4*sp* bands. The increased intensity for the O K pre-peak indicates that the iron 45 nm into the sample is more reduced than the iron at 3 nm into the sample, consistent with surface oxidation.

The L edges in Fe^{2+} and Fe^{3+} in iron oxides are attributed to excitation of a $2p^6$ electron to $Fe2p^53d^6$ for Fe^{3+} and $Fe2p^53d^7$ for Fe^{2+}.[121] The L-edge intensity is proportional to the Fe *d* character in the metal ions where the L_2 edge in magnetite has been observed to be shapeless, while the L_3 edge has been observed to have two pre shoulders.[121,122] The white line intensity ratio, I(L3)/I(L2), is known to increase for increased oxidation states[117], and as shown in *Figure 3.1* e, the intensity of the L_3 edge compared to the respective L_2 edge intensity is increased at 3 nm into the particle versus 45 nm into the particle, indicating increased Fe^{3+} enrichment at the 3 nm depth compared to the 45 nm depth herein measured.

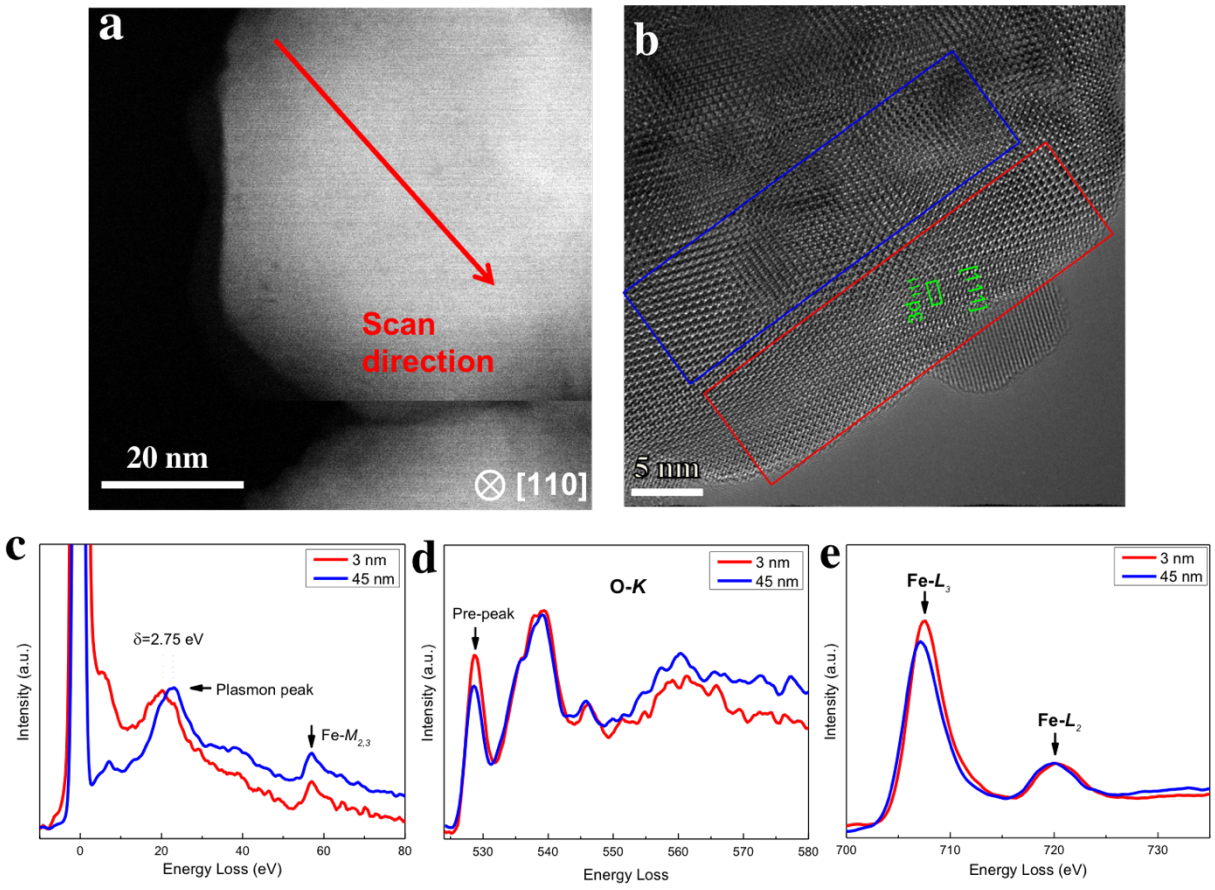

Figure 3.1: (a) Scan direction in 60 nm Fe_3O_4 nanoparticle. (b) HRTEM image viewed along [1-10]. EELS and losses in (c) plasmon peak, (d) low-loss, and (e) core loss regions for 3 nm depth (red) and 45 nm depth (blue) into 60 nm particle.

3.5 Electrochemical Behavior as a Function of Nanoparticle Size

The Fe_3O_4 nanoparticles are modeled as core-shell particles with the core consisting of pure Fe_3O_4 and the shell consisting of γ-$Fe_{2.67}O_4$. All particle sizes, independent of particle diameter, are assumed to have a 1.2 nm penetration depth of γ-$Fe_{2.67}O_4$ as seen in Figure 3.2a and b. Further details for the core-shell particles can be seen in Appendix 5. The reversible potential for the lithiation of 9 nm and 25 nm synthesized Fe_3O_4 nanoparticles compared to 32 nm commercial is shown in Figure 3.2 c. For nanoparticles fabricated with the same synthetic method, the initial intercalation regime in the reversible potential shows nanoparticle size-dependence, where the smaller particles exhibit higher potentials by up to

70 mV at the same nominal lithium concentration. The reversible potential for the commercially obtained 32 nm sample lies in between the two synthetic samples, indicating that the defect concentration in a particle may vary with the synthetic method.

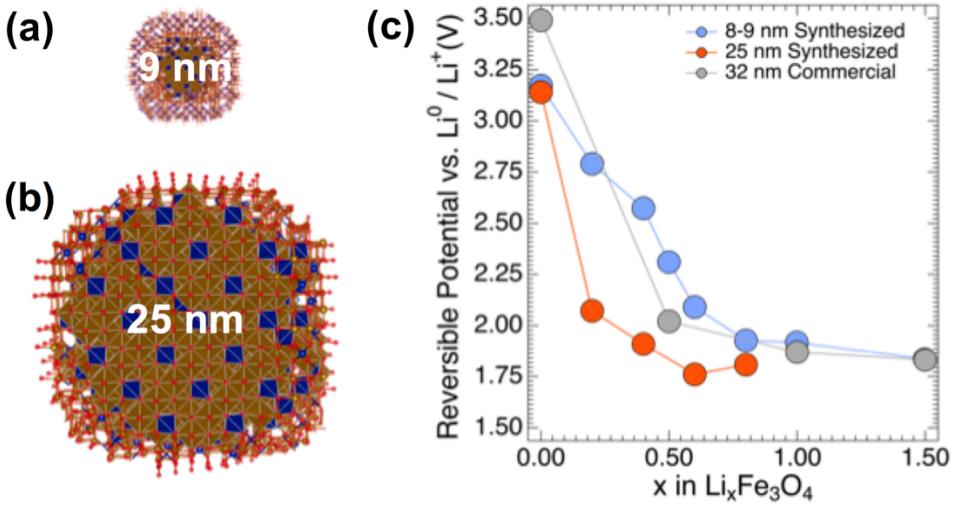

Figure 3.2: Theoretical treatment of Fe_3O_4 nanoparticles showing (a) 9 nm and (b) 25 nm particles, to scale, with constant penetration depth of 1.2 nm γ-$Fe_{2.67}O_4$, for both particle sizes. (c) Experimental reversible potential for 8-9 nm (blue) and 25 nm (orange) synthesized Fe_3O_4 nanoparticles and a 32 nm (grey) commercial Fe_3O_4 nanoparticle.

Experimental XRD patterns for unlithiated x=0.0 and fully relaxed samples taken at x=1.0 equivalents of lithium are shown for 10 nm and 30 nm particles in Figure 3.3 compared to the XRD patterns for the theoretical Fe_3O_4, γ-$Fe_{2.67}O_4$, and FeO structures shown in black, green, and grey respectively. The methods for the collection of the experimental and prediction of the theoretical XRD patterns can be seen in Chapter 4.3.2 and Chapter 4.3.5. Between x=0.0 and x=1.0, there are no significant changes in the diffraction patterns for either the 10 nm or 30 nm particles. Lithiation at 16d cationic defects in γ-$Fe_{2.67}O_4$ does not cause Coulombic repulsions between the inserted lithium and the iron at 8a and 16c sites, while insertion on the 16c sites in either γ-$Fe_{2.67}O_4$ or Fe_3O_4 results in migration of the 8a iron to vacant 16c sites as explored in Chapter 2. Lithiation at 16c and resultant migration of

iron at the 8a site to the 16c would cause the formation of a secondary peak at ~4.3° in the XRD pattern. For both nanoparticle sizes, the patterns at x=0.0 and x=1.0 show negligible differences. For the 30 nm particle, there is broadening at the late end of the 4.3° peak, as well as slight intensity increase at 5.1°. As can be seen in Figure 3.2 c, intercalation regime for the 30 nm particle ends at x~0.4 and at x~1.0 for the 10 nm particle, consistent with the observation of marginal changes in the 30 nm XRD spectra and negligible changes in the 10 nm XRD spectra at x=1.0. The lack of the secondary peak at x=1.0 for both 10 nm and 30 nm particles in the XRD pattern in Figure 3.3 and the lattice constant expansion being proportional to the concentration of defects in the nanoparticles in Figure 3.4 are both consistent with the initial intercalation regime consisting of lithiation at 16d cationic defects and not at 16c sites in either γ-$Fe_{2.67}O_4$ or Fe_3O_4.

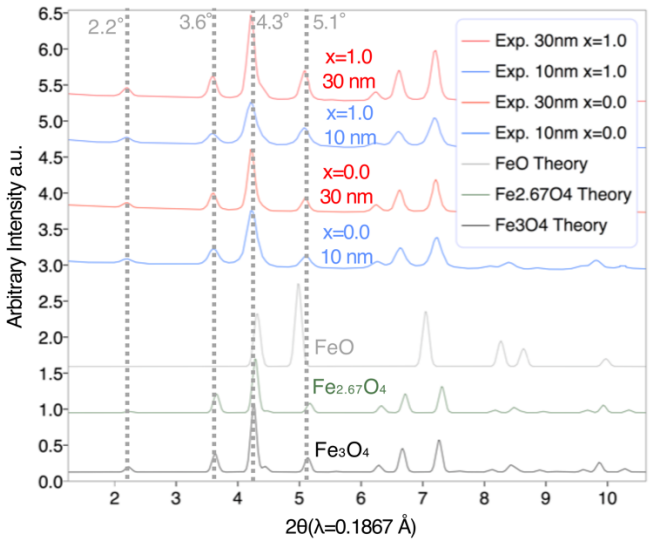

Figure 3.3: Experimental XRD patterns for 10nm and 30 nm Fe_3O_4 at x=0.0 and at the end of voltage relaxation for x=1.0. Theoretical Fe_3O_4, $Fe_{2.67}O_4$, and FeO XRD patterns are shown for reference, with lattice constant set at 8.398 Å for Fe_3O_4, 8.3419 Å for γ-$Fe_{2.67}O_4$, and 8.652 Å for FeO.[115]

At the x=1.0 lithiation state, the neutron-diffraction determined lattice constants are 8.3899(2) Å and 8.4087(1) Å. As can be seen in Figure 3.4, the smaller particle grows more

with lithiation in the intercalation regime than the larger particle does, indicated by the differences in the slopes of the experimental data for 10 nm (orange solid line) and 30 nm particles (blue solid line). The theoretical lattice constant value at x=0.0 is predicted with structural results from DFT+U calculations, where a correction has been applied to the DFT+U determined volume to account for the known overestimation of volume with GGA+U. The details of the DFT corrections can be found in Chapter 5.11.

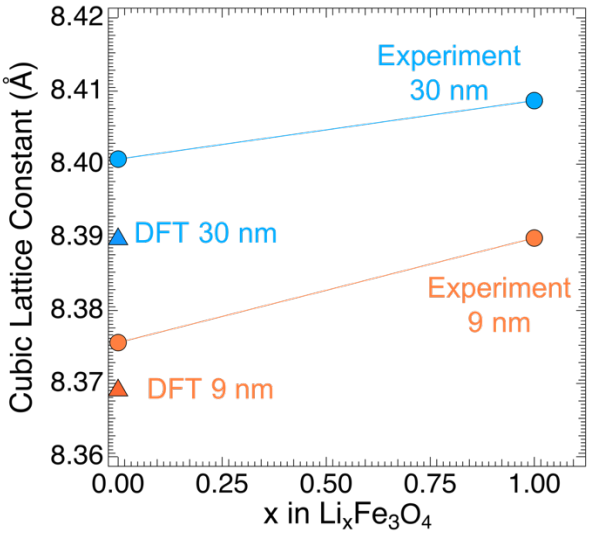

Figure 3.4: Neutron Diffraction lattice constant measurements compared to nanoparticle size dependent lattice constant prediction for 10 nm and 30 nm particles with 1.2 nm defect region at x=0.0.

To predict the nanoparticle lattice constant at x=0.0, the lattice constant of the nanoparticle is assumed to be the volume averaged lattice constant of the 1.2 nm defective surface and the Fe_3O_4 pristine core. As can be seen in Figure 3.4, the larger particles have a lattice constant closer to pure Fe_3O_4 while the lattice constant for the smaller particles is more consistent with maghemite, the defective material.

3.6 DFT Modeling of Electrochemical Behavior as a Function of Nanoparticle Size

The surface region of Fe_3O_4 nanoparticles are modeled with a bulk DFT calculation of maghemite $\gamma - Fe_2O_3$, the 16d cation defective inverse spinel, with defect ordering from a previous first-principles analysis focused on defect order.[103] The core of the nanoparticle is modeled with a bulk DFT calculation of Fe_3O_4. The details of the DFT calculations can be found in Chapter 5.3. The radius of the Fe_3O_4 core of the particle (r_c) is the difference between the XRD measured particle radius, r_p, and the penetration depth of defects (l_d) indicated from the neutron diffraction experiments, $r_p - l_d = r_c$. The theoretical capacity of the Fe_3O_4 nanoparticle with a $\gamma - Fe_2O_3$ surface is calculated as the volume average theoretical capacities for each of the pure materials, where the range of capacities is 1007 mAhr/g to 926 mAhr/g, as defined by pure $\gamma - Fe_2O_3$ and pure Fe_3O_4, respectively. The 9 nm particles with a 1.2 nm defect region are predicted to have a ~975 mAhr/g theoretical capacity, while the 25 nm particles with a 1.2 nm defect region are predicted to have a ~947 mAhr/g theoretical capacity.

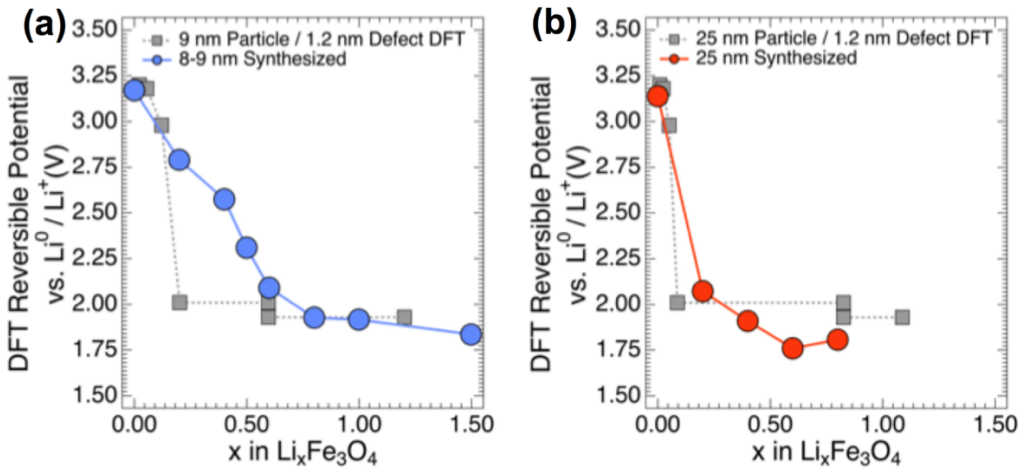

Figure 3.5: DFT+U predicted (squares) reversible potential compared to experimentally measured (circles) reversible potential for (a) 9 nm and (b) 25 nm Fe_3O_4 nanoparticles. The theoretically predicted nanoparticles have a with 1.2 nm defect region.

It was shown in Chapter 2 the filling of 16d cationic defects by lithium intercalation occurs at DFT+U calculated potentials ~2.98-3.01 V, while lithiation of non-defective pure magnetite is unstable and instead results in phase segregation into a rocksalt-like $LiFe_3O_4$ + spinel Fe_3O_4 at a DFT+U calculated potential of ~2.01 V, the first voltage plateau. Assuming a constant defect penetration depth of 1.2 nm for the 9 nm and 25 nm particles, the theoretical DFT+U voltage profiles overlaid with the experimental voltage profiles are shown in Figure 3.5. With the treatment of only 16d cationic defects in the nanoparticles, the amount of lithium that can intercalate into the nanoparticle is limited to the concentration of defects in the particle. However, as can be seen in Figure 3.5, the intercalation process for the experimental reversible potential lasts until x~0.4 for the 25 nm particles and x~1.0 for the 9 nm particles before the first phase segregation plateau occurs, while in a particle composed of 100% γ-$Fe_{2.67}O_4$, the maximum allowed concentration of lithium is x=0.33 for intercalation. In Figure 3.5b, only 16d cationic defects have been accounted for in the DFT+U simulations of the reversible potential, but there are likely other effects contributing to this intercalation regime such as particle surface lithiation or solid-electrolyte interphase side reactions.[123]

In Figure 3.5, it is seen that by incorporating the 1.2 nm defect layer inferred from the EELS and neutron-diffraction experiments, the experimental observation of the nanoparticle size dependence of the reversible potential can be captured with DFT+U calculations. The voltage plateau corresponds to the phase change $Li_yFe_{3-y}O_4 + Li \rightarrow Li_{1+y}Fe_{3-y}O_4$, where y=0.33 for $\gamma - Fe_{2.67}O_4$ at a DFT+U potential of 1.93 V and y=0 for Fe_3O_4 at a potential of 2.01 V. The $Li_{1.33}Fe_{2.67}O_4$ shell and $LiFe_3O_4$ core are both rocksalt structures, the details of which been previously studied and are reported in Chapter 2 and the structures can be seen in Appendix

4. With the constant 1.2 nm defect concentration, the 9 nm particle and the 25 nm particle have 60.6% and 26.1% $\gamma - Fe_{2.67}O_4$ respectively. It can be seen that the DFT+U predicted intercalation regime lasts longer in Figure 3.5a compared to b, due to the increased 60.6% $\gamma - Fe_{2.67}O_4$ in the 9 nm particle compared to the 26.1% in the 25 nm particle. Additionally, the 25 nm particle, being composed of 73.9% Fe_3O_4, has a larger plateau at 2.01 V in Figure 3.5b, which corresponds to the conversion of $Fe_3O_4 \rightarrow LiFe_3O_4$.

3.7 Conclusions for the Effects of Nanostructuring on Fe_3O_4 Nanoparticles

Neutron Diffraction data of 9 nm Fe_3O_4 and 25 nm Fe_3O_4 synthesized nanoparticles showed off-stoichiometry as a function of particle size, with both particle sizes characterized by a defect region of ~1.2 nm, resulting in significant differences in volume-average defect concentrations. Electron energy loss spectroscopy showed evidence for increased surface oxidation at 3 nm penetration depths compared to 45 nm penetration depths in 60 nm Fe_3O_4 nanoparticles, indicating that the Fe^{3+} enrichment occurred at the surface of the particles. The reversible potential for the lithiation of 9 nm and 25 nm Fe_3O_4 nanoparticles showed a size dependence which could only be accounted for theoretically when the Fe^{3+} surface enrichment and off-stoichiometry was included in the DFT model for the reversible potential. Here we show that the reversible potential of nanoparticulate magnetite varies with nanoparticle size and that this variation can be attributed to the cationic defects that occur as a function of nanoparticle size. As iron-oxides are prone to off-stoichiometry and nanomaterials can be prone to surface defects, we anticipate these results to be relevant to other iron-oxide nano materials compounds and more generally, any nanomaterials that could form surface defects.

CHAPTER 4: PHASE CHANGE AND CONVERSION REACTIONS ARISING FROM THE LITHIATION OF MAGNETITE NANOPARTICLES[4]

4.1 Chapter Overview

The phases occurring on the first voltage plateau for lithiation of Fe_3O_4 nanoparticles has been investigated with density functional theory (DFT) through the evaluation of stable or hypothesized, metastable reaction pathways. Hypotheses were compared to the measured reversible potential, x-ray diffraction (XRD), and neutron-diffraction measurements at two states of charge. The samples were discharged at the low rate of C/600 and the XRD and neutron diffraction characterization measurements were taken at least 600 hours following current interrupt to allow full relaxation of the sample. In contrast to what is predicted from the Li-Fe-O thermodynamic pathway, Fe^0 does not appear on the first voltage plateau in 10 or 30 nm Fe_3O_4 nanoparticles, in agreement with previous work.[51,97] Here, we have reconciled these observations on a ternary Li-Fe-O diagram and have put forth the most plausible reaction mechanism pathway, which results in rocksalt FeO and $LiFeO_2$, in addition to the Li_2O phase, all hypothesized to be occurring on the first voltage plateau.

[4] This chapter presents work that was done in collaboration with: Andrea M. Bruck, Kenneth J. Takeuchi, Amy C. Marschilok, Esther S. Takeuchi, and Alan C. West.

4.2 Introduction to Phase Change and Conversion Reactions Arising from the Lithiation of Magnetite Nanoparticles

4.2.1 Magnetite as an Electrode Material

The Li-Fe-O ternary phase diagram is rich with phases that have small differences in heats of formation, such as magnetite and maghemite[124] with ~10 meV/atom difference, or such as Li_2O[125] and Li_5FeO_4,[126] with ~40 meV/atom difference in formation energy, with free energy available at room temperature being ~24 meV/atom, k_BT. Room temperature and long-time scale persistence of metastable phases is not unique to the Li-Fe-O phase space and is a pervasive phenomenon in nature.[127] Due to the similarity in measured formation enthalpies, the number of DFT calculated potentials that satisfies experimentally measured voltages is not unique in the Li-Fe-O ternary phase space. Here we will show how the DFT+U predicted energetics for many of the combinations of phases present in the Li-Fe-O ternary space are commensurate with the electrochemically measured voltage of ~1.8 V and therefore additional modes of interrogation must be taken for reliable phase identification.

Magnetite is an iron oxide with an inverse spinel crystal structure, in the $Fd\bar{3}m$ space group. Iron exists in two oxidation states in two different coordination environments, with the 8a tetrahedral A-site fully occupied by Fe^{3+} and the 16d octahedral B-site 50/50 by Fe^{2+}/Fe^{3+}. Oxygen defines the cubic close packed lattice at the 32e site.[29] During lithiation of magnetite in an lithium-ion electrode, the overlap of reactions has been observed in nanoparticles under in situ observation,[41,45] likely due to both slow kinetics of the chemical reactions occurring and slow transport of lithium in the solid state. In battery systems with chemical additives, identification of equilibrium products can also be muddled by long relaxation times, during which side reactions may occur.[91] However, identification of the

equilibrium pathway is pertinent to the identification of the phases driving the structural rearrangements occurring during discharge, and as such, investigation into the reversible potential is warranted.

During discharge, it is observed that the cubic close packed (ccp) oxygen framework is maintained for $0 < x < 8$ equivalents of lithium into nanoparticulate magnetite. There are multiple phases in the Li-Fe-O ternary phase space that satisfy the experimental observation of maintaining the ccp oxygen framework with lithiation,[44] such as $LiFeO_2$, FeO, Li_5FeO_4, Li_2O, and Li_2FeO_3. Additionally, we recently show in a first-principles investigation that the rocksalt-like $LiFe_3O_4$ phase is predicted stable by ~5 meV/atom against phase segregation to $LiFeO_2$ + 2FeO, as reported in Chapter 2. As such, there have been multiple pathways proposed in the literature for the phases that may be driving the reactions observed during discharge. Distinguishing the phases driving the chemical reactions in Fe_3O_4 nanoparticles can enable the identification of the kinetic limitations of the material and diagnose phases contributing to cycling irreversibility.

4.2.2 The Three Known Lithiation Regimes of Nanoparticulate Magnetite

As was illustrated in Chapter 2 and Chapter 3, the reversible potential for lithiation of magnetite varies with particle size. Upon full reduction of nanoparticulate Fe_3O_4 with lithium, there are three characteristic structural changes as indicated by the experimentally measured reversible potential, and in larger micron-sized magnetite particles, only two regimes have been observed.[38,51,98,128] In the case of nanoparticulate magnetite, there is an intercalation regime followed by two voltage plateaus, one at ~1.8 V and the second at ~1.2V. For larger particles of magnetite, there is an intercalation regime followed by only one voltage plateau at ~1.2V.[38,51,128] Here we focus on the smaller nanoparticles that show two

voltage plateaus, but highlight that the reaction pathway has been observed to be a function of particle size.

4.2.2.1 Regime 1: The Intercalation Regime in Nanoparticulate Magnetite

The full reversible potential for 8 nm Fe_3O_4 can be seen in Figure 4.2. The intercalation region in Fe_3O_4 for $0 < x < \sim 1.0$ has been attributed to lithium intercalation into 16c sites in Fe_3O_4 magnetite resulting in a rocksalt-like structure that was hypothesized to form in a solid-solution type reaction between the spinel and rocksalt phases.[38] In Chapter 3 it was shown that for the reversible potential, this intercalation regime is attributed to filling of cationic iron defects on 16d sites with lithium and other surface or nanoparticle effects, the spinel phase is maintained for the intercalation process, and no rocksalt is formed during intercalation. Additionally, it was shown in Chapter 2 that once the 16d defects have been filled with lithium, further lithiation at 16c site is destabilized by Coulombic interactions between inserted lithium and iron in the tetrahedral (A) sublattice and a phase change to a rocksalt-like $LiFe_3O_4$ material may occur. The implication is that there is no reaction that results in a rocksalt-like phase that can be attributed to the initial intercalation regime, and that at the start of the first reversible potential plateau the sample primarily resembles the spinel phase.

4.2.2.2 Regime 2: The Phase Change to a Rocksalt Phase

The intercalation regime is followed by the first voltage plateau at around ~1.8 V as illustrated in Figure 4.2, where the spinel structure is observed to transition from inverse spinel magnetite to the aforementioned rocksalt-like structure. There are many phases in the ternary phase diagram that satisfy the requirement of a rocksalt-like phase. Additionally, many combinations of these phases also predict a DFT voltage that is comparable to the

experimental voltage of 1.8 V for this first plateau. As can be seen in Figure 4.1a, the bulk phase ternary phase diagram predicts that, on this first voltage plateau, BCC-Fe^0 should be extruded; however, previous analyses indicate that Fe^0 is not observed.[51,97] For this reason, lithiation of Fe_3O_4 nanoparticles may follow a metastable pathway. Here we seek to identify the metastable phases occurring on the first voltage plateau.

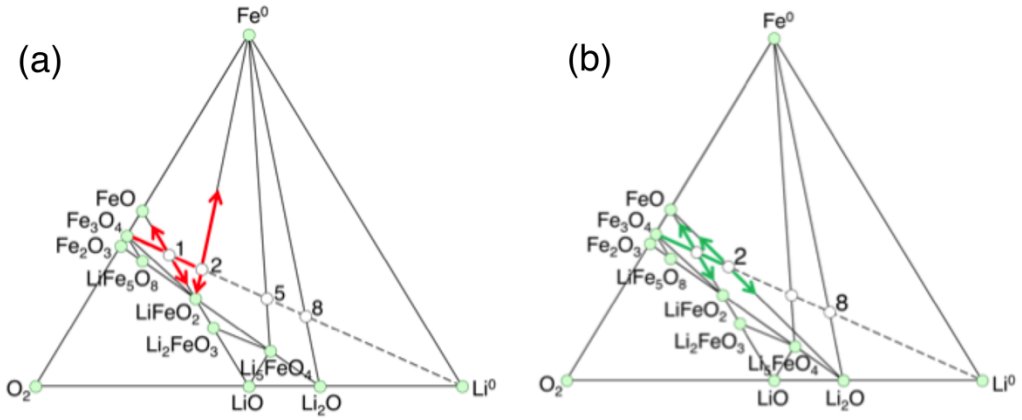

Figure 4.1: Li-Fe-O ternary phase diagrams with known stable phases in green, the lithiation of magnetite as a dashed line, and white open circles indicating x for $Li_xFe_3O_4$ lithiation states. Bulk Li-Fe-O ternary phase diagram prediction for first phase plateau phase change predicting iron extrusion in shown in (a). The metastable redrawing of Li-Fe-O phase diagram showing no iron extrusion on first plateau is shown in (b), this is the pathway most consistent with experiment.

To identify the phases occurring on the first voltage plateau, nine hypotheses were developed based on redrawing of the *x*=0 - 2 region on the ternary diagram, summarized in Table 4.1. Of these hypotheses, four included the extrusion of iron and five did not. DFT was used to predict potentials for all of these hypotheses, and it was found that the differences in potentials spanned 200 mV for eight of the hypotheses, similar to the variation in the experimentally measured plateau itself, and one hypothesis was +300 mV. In Figure 4.1b the ternary phase diagram is redrawn connecting FeO→Li_2O, eliminating the extrusion of BCC-Fe^0 on the first voltage plateau and showing the metastable pathway most consistent with

the experimental measurements of voltage, XRD, and neutron diffraction measurements reported herein.

4.2.2.3 Regime 3: The Final Conversion Plateau

The final voltage plateau results in the final conversion products, BCC-Fe and Li_2O. On the Li-Fe-O ternary phase diagram in Figure 4.1. it can be seen that full reduction (8 equivalents) of magnetite with lithium results in Li_2O + BCC-Fe^0. Consequently, the final voltage plateau at ~1.2 V on the reversible potential is attributed to the end products of the conversion reaction, Li_2O + BCC-Fe. This is widely accepted in the literature, however due to mass transport resistances leading to spatial variations in Li concentration, these phases have been observed earlier than the nominal concentration predicted by thermodynamics.[41]

4.2.3 Previous Studies of The Two Voltage Plateaus of the Reversible Potential

The observation of a rocksalt-like phase on the first voltage plateau is consistent throughout the literature. After 24 hours of relaxation following lithiation to $Li_{1.5}Fe_3O_4$, X-ray powder diffraction studies indicated the sample to be predominately rocksalt, with evidence of unreacted spinel.[38] In another study, at x=1.7, 16% unreacted spinel remained in the sample.[97] Room temperature studies have shown no evidence for iron for $0 < x < 2.0$ at fully relaxed conditions.[51,97] However, both of the Fe^0+ Li_2O conversion products have been observed during discharge prior to the thermodynamically predicted concentration and occurring in parallel with the first phase change reaction that results in the rocksalt structure.[41,97] A study of the equilibrium phases for the lithiation of α- Fe_2O_3 at 420°C showed that the material converted to the inverse spinel γ-Fe_2O_3, which is a defective Fe_3O_4 structure and upon lithiation at 420°C, iron was extruded at x=0.5, 1.5, and 3.0.[78] The elevated

temperature observation of BCC-Fe at such low lithiation states indicated that Fe extrusion of the first voltage plateau is a possibility, given enough time.

He et al., used DFT+U calculations to predict the reversible potential for two competing pathways for the full $0 < x < 8$ equivalents. One of the pathways was guided by the stable phases on the Li-Fe-O ternary diagram and is the thermodynamically predicted equilibrium path. The second proposed pathway was metastable and motivated by the experimentally observed phases occurring in situ. In both pathways, the first equivalence of lithium passed results in the formation of the rock-salt $LiFe_3O_4$ phase. In the equilibrium pathway, further lithiation of $LiFe_3O_4$ resulted in $LiFeO_2$+Fe^0, followed by three additional steps continuing to form BCC-Fe^0. This equilibrium pathway predicts that Fe^0 is formed on the first voltage plateau. The second pathway was a two-step process where the $LiFe_3O_4$ phase converts directly to the Li_2O+Fe^0 conversion products. The study is primarily focused on the heterogenous reaction kinetics far from equilibrium and discharged at high rates, conditions relevant to device operation, where both proposed pathways could be occurring in parallel. The work illustrates the mass transfer resistances and slow kinetics magnetite is plagued with. To isolate kinetic effects from equilibrium conditions, here we focus on the opposite limit, with slow C/600 discharge rates and upwards of 600 hour relaxation times to ensure samples are fully relaxed. Additionally, He et al. illustrated that the two pathways proposed predicted comparable potentials, and we will further show that many other pathways satisfy the same criteria.

4.2.4 The Need for An Integrated Approach to Phase Identification

To identify the reaction driving the phase change corresponding to the first voltage plateau, a series of hypotheses was developed that satisfy several constraints. First, the

phases within the Li-Fe-O phase space must yield a ccp rocksalt-like structure. This is due to the experimental observation that through full lithiation, the ccp oxygen network remains invariant.[44] Secondly, the hypotheses must satisfy the constraint of the nominal lithium concentrations allowed on the first voltage plateau, ~2 equivalents, and they must satisfy the voltage observed experimentally, ~1.8 V. Reactions are grouped into two categories: those that allow iron to be extruded on the first voltage plateau and those that do not allow iron extrusion.

To interrogate hypotheses, the theoretical XRD patterns should be consistent with experimental XRD patterns taken at equilibrium conditions at x=2.0, probing the position of iron in the system. In addition, the position of lithium in the proposed phases and the theoretical lattice constants should be consistent with equilibrium lattice constants and lithium locations measured with neutron diffraction patterns, taken at equilibrium conditions at x=2.0.

4.3 Methodologies

4.3.1 Electrochemical Measurements

The reporting for the 8 nm and 32 nm reversible potential has been previously published.[52,98] Coin cell batteries were fabricated under Argon. The positive electrode was a slurry-type electrode with carbon additive, polyvinylidene fluoride binder matrix, and Fe_3O_4 nanoparticulate active material against the solid lithium negative electrode. The positive electrode slurry consisted of magnetite (90 wt %), acetylene carbon black (5 wt%), and polyvinylidene fluoride binder (5 wt%) coated onto an aluminum foil substrate. The electrolyte was a 1:1 by volume ratio of dimethyl carbonate and ethylene carbonate

electrolyte in 1 M $LiPF_6$. The electrode pellets were 51 $\pm 4\mu$m thick. All electrochemical testing was performed at 30°C. The coin cells consisting of the commercial 32 nm Fe_3O_4 particles were discharged at C/200 to x=0.5, 1.0, 1.5, 2.0, 2.5, 3.0, 3.5, and 4.0. The 8 nm Fe_3O_4 particles were discharged at C/200 to 0.5, 1.0, 1.5, 2.0, 2.5, 3.25, 3.5, 4.0, 4.5, 5.0, 6.0, 7.0, and 8.0 equivalents. Following discharge, the current was interrupted, and the cells were allowed to rest for up to 720 hours. Each reversible potential measurement corresponded to a single coin cell experiment. The x=0.0 voltage for a given particle size was taken as the average resting voltage of all the coin cells of that particle size before the current was turned on.

4.3.2 XRD and Neutron Diffraction Measurements

XRD and neutron diffraction analysis was completed on 10 nm and 30 nm active material Fe_3O_4 that was synthesized by the co-precipitation method previously reported.[47,48] Constant current lithiation without preconditioning at C/600 was carried out to x=1.0 and 2.0 for the 10 nm and 30 nm samples. At least seven coin cells were used for each active material size at each state of lithiation. Following discharge to either x=1.0 or x=2.0, the circuit was made open and the samples were allowed to relax for a minimum of 600 hours. The reversible potential following C/600 discharge and voltage relaxation was compared to the previously reported reversible potential curves and can be seen in Appendix 7.

Monochromatic x-ray powder diffraction (XRD) was performed ex situ at λ=0.1887. The Fe_3O_4 electrode powder was packed in a polyimide tube for X-ray Powder Diffraction (XPD) measurements at Brookhaven National Laboratories (BNL) National Synchrotron Light Source II (NSLS-II) beamline 28-ID. The beam was calibrated to a wavelength of

0.18667 Å and used a 16-inch CsI scintillator detector for the collection of 2D images that were integrated to 1D diffraction data using a LaB6 standard.

Samples used for neutron diffraction were only handled in Ar or N_2 environment as they were prepared for Time-of-flight (TOF) powder neutron diffraction analysis at POWGEN (BL-11A) diffractometer at the Spallation Neutron Source (SNS), Oak Ridge National Laboratory, Oak Ridge, Tennessee.

4.3.3 First Principle Calculations Methods

A zero temperature Li-Fe-O ternary phase diagram was constructed in Chapter 2 and Chapter 5. All calculations were performed with Vienna ab initio simulation package (VASP)[129] with projector augmented wave potentials,[129–131] with an energy cutoff of 600 eV. To account for the Coulomb interactions in the 3d orbitals of Fe, U_{eff}=5.3 eV was used.[56,70,72] In the case of Fe^0, an effective U was not applied, as it is not physically reflective of the conductive electronic structure. To ensure accurate prediction of reaction energies which include both Fe^0 and materials with correlation in 3d orbitals, corrections were applied to account for mixing of GGA and GGA+U from the methodology developed by Jain et al.[132] The corrections impact the reaction energies, and therefore the voltages, when Fe^0 is a reactant or product, the details of which can be seen in Chapter 5.10. The generalized gradient approximation by Perdew, Burke, and Ernzehof (PBE) was used for the exchange-correlation energy.[133] A Γ-centered grid defined by a 3×3×3 mesh for the cubic Fe_3O_4 structure was used for Brillouin zone sampling. The mesh was scaled appropriately for structures sampled in different supercells. The Methfessel-Paxton smearing scheme of order 1 with a broadening parameter of 0.2 eV was employed. Total energies were found to converge to within 2

meV/f.u and a force criterion of 0.05 eV/Å was applied. Cells were allowed to relax fully without imposing symmetry. Further details for DFT calculations can be seen in Chapter 5.

4.3.4 Prediction of potential

Equilibrium voltages have been predicted from the DFT calculations in the Li-Fe-O ternary phase space as outlined in Chapter 5.9. To arrive at voltages from DFT calculated energies, a stoichiometrically consistent reaction is written out, and the zero-temperature change in energy upon reaction A + nLi^0 → C is computed with energies from the DFT calculations, resulting in $\Delta E_f = E(C) - E(A) - nE(Li^0)$ for the reaction energy. The voltage is then determined from the reaction energy, $V = -\frac{\Delta E_f}{nF}$, where *n* is the number of electrons passed in the reaction. We direct readers to the review papers on the methodology relating the DFT calculated change in zero temperature reaction energy to equilibrium potential for more information.[55,134,135]

In the case of a phase change reaction, the voltage is constant for all concentrations on the plateau. We plot the phase change voltage over the full concentration range sampled. For instance, for a reaction where 1 electron is transferred, we plot the DFT predicted potential over a range of Δx =1.0. Where indicated, the potential is not necessarily plotted at the nominal x value indicated by the reaction. For instance, the reaction Fe_3O_4 + Li → $LiFe_3O_4$ may be plotted starting at a nominal x value on the x-axis of *x*=1.0 and lasting until *x*=2.0 due to side reaction and defect filling occurring between nominal *x*=0.0 and *x*=1.0 as examined in Chapter 2 and Chapter 3.

The reversible potential is split into three regions, the first intercalation regime for which $0 < \overline{x_i} < \overline{x_{i,max}}$, and the first voltage plateau, where $0 < \overline{x_{P1}} < \overline{x_{P1,max}}$ are defined by

the slope of the measured reversible potential. The maximum intercalation, first voltage plateau, and final voltage plateau concentrations are $\overline{x_{i,max}}$ and $\overline{x_{P1,max}}$. All maximum concentrations are defined by the nominal measured value of x defined for a given voltage cutoff determined from experimental measurements of the reversible potential. The voltage cutoffs for $\overline{x_{i,max}}$ and $\overline{x_{P1,max}}$ are 1.88 V and 1.78 V, respectively and the concentrations at which these potentials occur are a function of nanoparticle size.

4.3.5 XRD Predictions

The DFT relaxed structures were used to predict XRD patterns using Crystal Diffract® Package in the CrystalMaker Software package. The software allows for predictions of mixtures of pristine phases. For a given theoretically determined XRD pattern with a mixture of phases, volume fraction for mixtures of phases were determined from the molar ratios presented in the reactions written out herein. An XRD pattern for each DFT structure was compared to patterns predicted from room temperature experimental structures taken from Karlsruhe Crystallographic and American Mineralogist Crystal Structure Databases to ensure no additional peaks or splitting were occurring in zero temperature DFT calculated structures. All DFT patterns matched well except for FeO. Density functional theory identifies ground state structures, and FeO is known to be monoclinic at 0K,[136] as such, additional splitting was observed in the theoretical 0K structure compared to the room temperature experimental pattern. An experimental structure was therefore used for FeO. The XRD pattern for $LiFe_3O_4$ used here is the lowest energy structure identified in Chapter 2, where DFT was used to examine stability of this phase and it was found that the compound was predicted stable against phase segregation to FeO + $LiFeO_2$ by ~5 meV/atom.

4.4 Results

4.4.1 Measured and DFT Predicted Reversible Potential

The reversible potential for the lithiation of synthesized 8 nm Fe_3O_4 nanoparticles and commercially obtained 32 nm Fe_3O_4 particles is shown in Figure 4.2 and is reproduced from previous studies.[52,98] It is observed that the first voltage plateau occurs at ~1.8 V and lasts for Δx_{P1}=2.0 equivalents. Following the first phase change plateau, the conversion plateau is observed for the 8 nm particles at ~1.2 V.

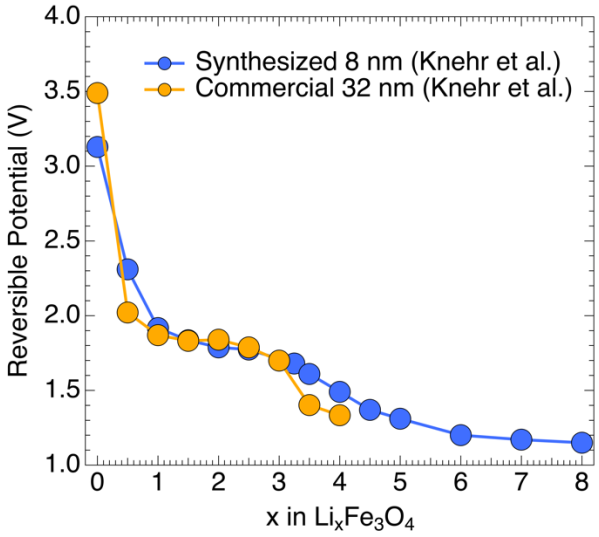

Figure 4.2: Experimentally measured reversible potential for 8 nm and 32 nm Fe_3O_4 nanoparticles.

4.4.2 Hypothesized Reactions Occurring on First Phase Change Plateau

Fifteen hypothesized reaction mechanisms were tested, and nine yielded DFT+U calculated equilibrium potentials that satisfy the experimental potential of 1.8 V, which are shown in Table 4.1. In four of the pathways (a-d), BCC-Fe^0 is predicted to form while the other five do not involve the formation of iron (e-i). The experimentally observed plateau potential is ~1.8 V, the five DFT predicted potentials within 100 mV of the experimental value are shown in bold, (a,d,g,h, and i), these hypotheses are closest to the experimental

measurement. The remaining three between ±100-200 mV are shown in regular type, (b, c, and i). The lowest energy hypothesis, (e), is shown in italics as it is 300 meV above the measured value.

As seen in the open circuit potential in Figure 4.2, the first phase change plateau lasts for Δx_{p1}=2.0 equivalents of lithium, where x_{p1} is the discharged concentration of lithium on the first plateau. For each hypothesis in Table 4.1 the maximum length of the plateau is indicated in the second line of the second column followed by the concentration at which the reaction in column 1 is written at. As can be seen, not all hypotheses last the full 2.0 equivalents, but are included herein as the products are in the correct concentration range on the ternary phase diagram and they may still occur in combination with another reaction. In columns three and four in a Table 4.1, a qualitative assessment of agreement of the theoretically proposed reaction with measured potential, measured plateau length, experimental XRD, and neutron diffraction measurements is given. In column five, a qualitative percent match for the proposed reaction is given, which will be further developed throughout the discussion of the paper. The percent match is calculated as 1 point for each criterion corroborated by experiment, 0.5 point for moderate agreement, and 0 points for poor agreement with experiment. The maximum agreement would be 4/4 points, one for each: DFT voltage, plateau length, XRD measurement, and neutron diffraction measurement.

Table 4.1. Hypothesized reactions for the first voltage plateau (column 1) with the corresponding DFT predicted voltages, and equivalents of lithium allowed for each reaction (Column 2), and qualitative assessment of hypothesized reaction match with XRD and Neutron diffraction experiments, along with qualitative assessment of overall hypothesized reaction match to experiment.

Hypotheses for Reaction Pathway on First Voltage Plateau (Red Pathway in Figure 4.3)	DFT Predicted Voltage and Allowed x_{p1}	Agreement with Exp. x=2.0 XRD	Agreement with Exp. x=2.0 Neutron Diffraction	Qualitative Percent Match
Iron Extrusion				
a) $Fe_3O_4 + x_{P1}Li^0 \rightarrow 2\ LiFeO_2 + Fe^0$	**1.9 V** **$0 < x_{P1} < 2$ (2.0)**	Poor	Poor	2/4 50%
b) $Fe_3O_4 + x_{P1}Li^0 \rightarrow 0.57\ Li_2O + 0.86\ LiFe_3O_4 + 0.43\ Fe^0$	1.6 V $1 < x_{P1} < 6$ (2.0)	Poor	Poor	1.5/4 37.5%
c) $Fe_3O_4 + x_{P1}Li^0 \rightarrow Li_2O + 0.75\ Fe^0 + 0.75\ Fe_3O_4$	1.6 V $0 < x_{P1} < 8$ (2.0)	Poor	Poor	1.5/4 37.5%
d) $Fe_3O_4 + x_{P1}Li^0 \rightarrow 0.4\ Li_5FeO_4 + 0.8\ Fe^0 + 0.6\ Fe_3O_4$	**1.7 V** **$0 < x_{P1} < 5$ (2.0)**	Poor	Poor	2/4 50%
No Iron Extrusion				
e) $Fe_3O_4 + x_{P1}Li^0 \rightarrow LiFe_3O_4$	*2.1 V* *$0 < x_{P1} < 1$ (1)*	Moderate, extra low angle peaks	Moderate	1/4 25%
f) $Fe_3O_4 + x_{P1}Li^0 \rightarrow 2\ FeO + LiFeO_2$	2.0 V $0 < x_{P1} < 1$ (1)	Consistent	Consistent	2.5/4 62.5%
g) $Fe_3O_4 + x_{P1}Li^0 \rightarrow 0.5\ LiFeO_2 + 2.5\ FeO + 0.5\ Li_2O$	**1.7 V** **$0 < x_{P1} < 2$ (1.5)**	Consistent	Moderate, Li_2O not consistent	3.5/4 87.5%
h) $Fe_3O_4 + x_{P1}Li^0 \rightarrow 0.5\ LiFe_3O_4 + 1.5\ FeO + 0.5\ Li_2O$	**1.8 V** **$0 < x_{P1} < 2$ (1.5)**	Moderate, extra low angle peaks	Poor	2/4 50%
i) $Fe_3O_4 + x_{P1}Li^0 \rightarrow 3\ FeO + Li_2O$	**1.8 V** **$x_{P1} = 2$**	Poor	Poor	2/4 50%

For DFT prediction, the potentials that are greater than 200 mV are considered poor agreement (0 points), the potentials within 100-200 meV are considered moderate (0.5 points), and the potentials within 100 meV are considered good agreement (1 point). Agreement with XRD is rated as poor (0 points), moderate (0.5 points), or consistent (1 point). The neutron diffraction is also rated as poor (0 points), moderate (0.5 pts.), or consistent (1 point). The details of the XRD and neutron diffraction rating will be developed in the following sections.

4.4.3 Ternary Diagrams for Hypothesized Reactions Occurring on First Phase Change Plateau

All of the hypotheses put forth herein can be seen graphically in the ternary phase diagrams in Figure 4.3, where the figure letters in Figure 4.3 correspond to the hypothesis letter in Table 4.1. In Figure 4.3, the first voltage plateau is shown in red with the corresponding DFT predicted voltage also in red. Following the first voltage plateau is the known conversion to Li_2O+Fe^0, occurring at ~1.2 V in Figure 4.2, this pathway is shown in blue in Figure 4.3. The reactants for the conversion reactions are the products from the first phase change plateau and are numbered according to the numbering for the first phase change plateau hypotheses. In some cases, the ternary phase diagram indicates there is more than one step to arrive at $Li_8Fe_3O_4=4Li_2O+3Fe^0$, and these additional steps are shown in orange.

Until recently, Figure 4.3a was believed to be the equilibrium pathway for the lithiation of magnetite, however, in Chapter 2 it was shown that $LiFe_3O_4$ is predicted stable against phase segregation to $LiFeO_2$ + 2 FeO by ~5 meV/atom on a 0K ternary diagram, this path is shown in Figure 4.3e. This lowest energy pathway is predicted at 300 mV higher than the experimental measurement but it is included in Table 4.1 and Figure 4.3 as it is the lowest energy path for lithiation to x=1.0.

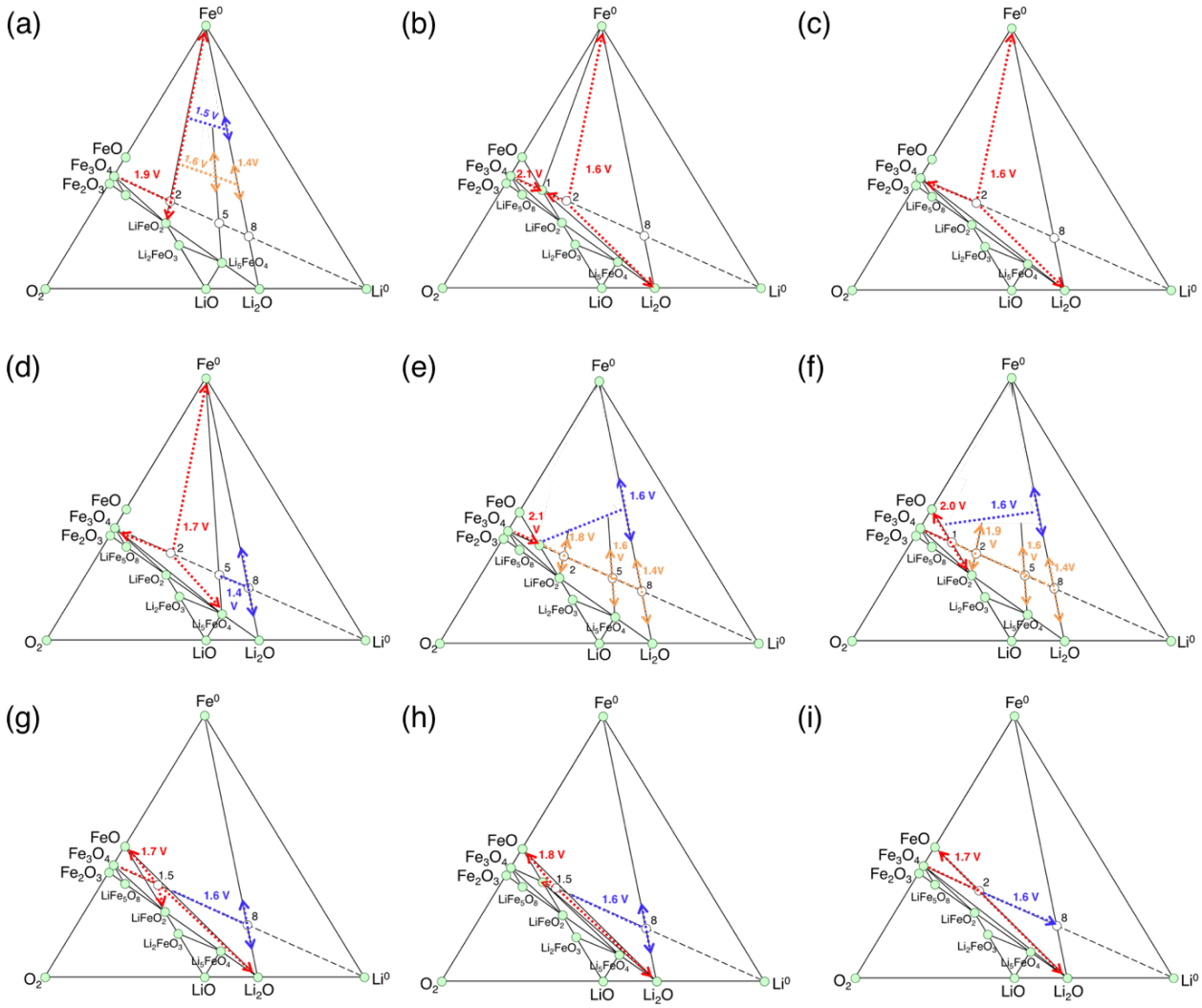

Figure 4.3: Ternary phase diagram pathways for hypotheses a-i in Table 1. For all ternary diagrams the red pathway is the first voltage plateau with the corresponding DFT predicted voltage. Following the first plateau, the pathway options to get to $Li_8Fe_3O_4$=4Li_2O + 3Fe^0 are shown in different colors. One step process from the first plateau in red to 4Li_2O + 3Fe^0 is shown in blue, while other multi-step pathways are shown in orange.

4.4.4 XRD Measurements and Predictions

In Figure 4.4a, the experimental XRD patterns for x=0.0 and fully relaxed equilibrium patterns for x=1.0 and 2.0 equivalents of lithium are shown for 10 nm (blue) and 30 nm (red) Fe_3O_4 nanoparticles. Additionally, the XRD pattern for the DFT Fe_3O_4, FeO, and Fe^0 structures are shown in black for reference. Between x=0.0 and x=1.0, there is not a substantial difference between the diffraction pattern for neither the 10 nm nor the 30 nm particles, and

the lithiation mechanism can be attributed to cationic defect filling as reported in Chapter 2 and Chapter 3. The peak at 3.6° is still present in the *x*=2.0 patterns for both nanoparticle sizes and can be indexed to the Fe_3O_4 phase but is not present in the pure FeO phase as seen in Figure 4.4a. The peak at 2.2° that is present in the *x*=2.0 patterns can be indexed to the Fe_3O_4 phase in Figure 4.4a but is also observed in $LiFeO_2$ and $LiFe_3O_4$ as seen in hypotheses (a)-(h) in Figure 4.4b. At *x*=2.0 equivalents, the experimental patterns show distinct peak splitting of the spinel peak at 4.2°. This splitting is indicative of a rocksalt-like structure forming, as can be seen in by the FeO peak shift at 4.2° relative to the Fe_3O_4 pattern in Figure 4.4a.

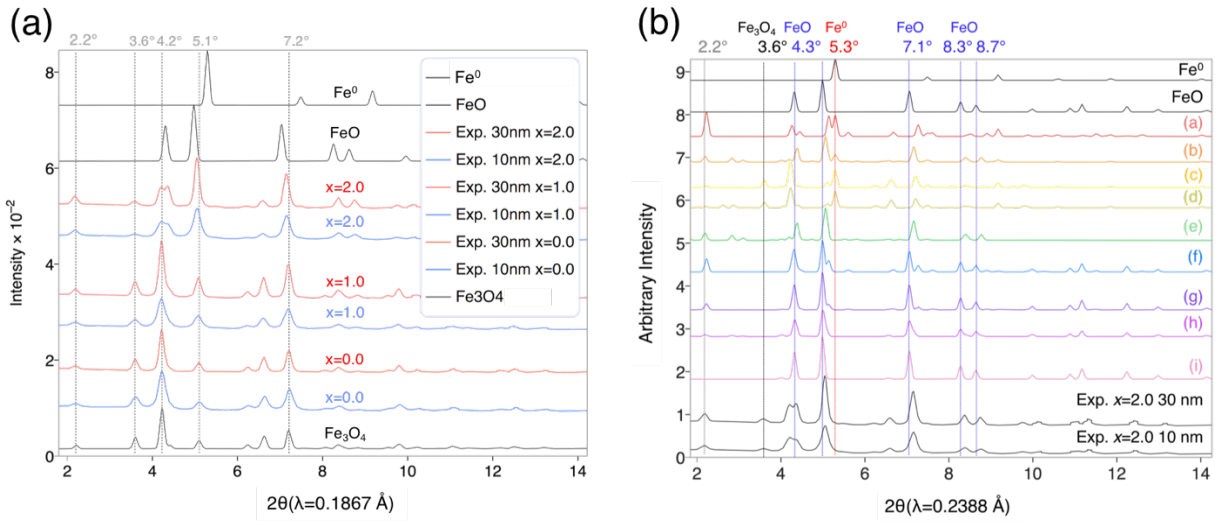

Figure 4.4: (a) Experimental XRD patterns for 10nm and 30 nm Fe_3O_4 at *x*=0.0 and at end of voltage relaxation for *x*=1.0, 2.0. (b) Theoretically predicted XRD patterns for hypothesis (a)-(i) at *x*=2.0 compared to experimental *x*=2.0. The volume of the theoretical structures in (b) have been adjusted according to a volume correction outlined in Chapter 5.11

4.4.5 Neutron Diffraction for Experimental Lattice Constant Determination

The Neutron diffraction lattice constants for the 10 nm and 30 nm particles were determined at *x*=0.0 as 8.3756(2) Å and 8.4007(2) Å. The 16d site was found to be fractionally occupied at 0.93(1) and 0.96(7), resulting in $Fe_{2.82}O_4$ and $Fe_{2.93}O_4$, for the 10 nm

and 30 nm particles respectively. At x=1.0, the Neutron Diffraction determined lattice constants are 8.3899(2) Å and 8.4087(1) Å.

Neutron diffraction experiments indicate that at x=2.0, there are two distinct crystalline phases observed in the 10 nm and the 30 nm particles. The lattice constants for these two phases were determined to be 8.4066(2) Å and 8.4484(6) Å. The small lattice constant phase, at 8.4066(2) Å, was present at 40% by weight and 20% by mole and was indexed to unreacted Fe_3O_4 with the inverse spinel structure. In the 10 nm particles, the two crystalline phases at x=2.0 were found to have 8.4066(2) Å and 8.4856 Å lattice constants. A crystalline Li_2O phase was unable to be detected at x=2.0 with neutron diffraction.

4.5 Discussion

4.5.1 DFT Predicted Potentials for First Voltage Plateau

In Table I, combinations of products are used which satisfy experimental observation that the ccp oxygen lattice remains invariant upon full lithiation.[44] As is seen in Table I, DFT predicts multiple reactions give a reasonable range for the DFT prediction of voltage, while also satisfying the number of electrons passed on this first voltage plateau. Here we see that the prediction of potential alone with DFT is insufficient to predict any one reaction pathway, and we turn to other structural characteristics afforded by density functional theory to aide in phase elucidation.

4.5.2 Absence of Evidence for Fe^0 in XRD Measurements

To assess if Fe^0 is forming at x=2.0, the XRD patterns for the reactions in Table 4.1 have been predicted and compared to measurements at x=2.0 in Figure 4.4b. In Figure 4.4b, hypotheses (a-d) all have the Fe^0 peak indicated by the red dashed vertical line at 5.3°, which

is not observed experimentally. In Table 4.1, the agreement between hypotheses (a-d) and the experimental XRD pattern are all considered 'poor' due to this additional Fe^0 peak, and the possibility for iron extruding and forming a *bulk-like phase* is therefore eliminated by comparison of the first 4 hypotheses (a-d) with experimental XRD patterns as well as poor agreement with neutron diffraction. It should be noted that the XRD pattern for iron used here is a bulk pattern, and other studies have indicated that iron extrusion can result in nanoparticulate Fe^0, which may not be present on an XRD pattern depending on nanoparticle size. TEM studies at equilibrium conditions could be used to further elucidate this possibility, but Fe^0 is likely not forming in any bulk-like form, consistent with previous studies.[51,97]

4.5.3 Neutron Diffraction Measurements for the Position of Lithium at *x*=2.0

The neutron diffraction fitting indicated a best fit for two crystalline phases at *x*=2.0 for 30 nm particles, with lattice constants of 8.4066(2) Å and 8.4484(6) Å. The smaller crystalline phase present at *x*=2.0 with a lattice constant of 8.4066(2) Å, is consistent with the 8.4087(1) Å value measured at *x*=1.0, which was determined to be the spinel phase with lithium inserted at 16d cation defect sites in Chapter 2 and Chapter 3. The neutron diffraction patterns indicated that the 8.4066(2) Å phase is consistent with spinel with Li on the 16d sites, not the vacant 16c sites. The small phase lattice constant observed at *x*=2.0, 8.4066(2) Å, is therefore assigned to the defect lithiated spinel phase present at *x*=1.0.

The neutron diffraction measurements indicated that lithium was not homogenously organized in the large phase, 8.4484(6) Å. Rather, the measurements were most consistent with partial occupation of lithium at 16c and 16d sites combined with a phase that did not contain any lithium. The results from the neutron diffraction measurement are therefore not consistent with the $LiFe_3O_4$ phase, hypothesis (e), as this phase has lithium constricted to the

16c site, $[LiFe]_{16c}[Fe_2]_{16d}O_4$. The neutron diffraction data for the position of lithium most consistent with $LiFeO_2$+ FeO, hypothesis (f), at a predicted potential of 2.0V as listed in Table 4.1. Where the $LiFeO_2$ phase has lithium on both 16c and 16d sites, $[Li_{0.75}Fe_{0.25}]_{16c}[Li_{0.25}Fe_{0.75}]_{16d}O_2$. This structure is consistent with a material that initially has defects on the 16d sites, which are filled by lithium during the initial intercalation regime. However, the 2.0 V DFT predicted potential for this reaction is slightly high compared to the experimentally measured 1.8 V and only one equivalent of lithium can be passed with this reaction, compared to the two equivalents experimentally measured.

As can be seen in Table 4.1, hypothesis (g) with the same $LiFeO_2$ + FeO products but with the addition of Li_2O, has a closer DFT predicted potential of 1.7 V, and the reaction can last the full 2.0 equivalents measured experimentally. The neutron diffraction measurements did not detect the formation of a crystalline Li_2O phase, however, the lattice mismatch between Li_2O and the other possible phases forming in the nanoparticles is high, at 9.86%, 7.43%, and 10.53% for Fe_3O_4, FeO, and $LiFeO_2$, respectively, contributing to the likelihood of an amorphous and not well defined crystalline phase. These phases are characterized in the following sections utilizing XRD analysis for further information regarding the positions of iron.

4.5.4 XRD Analysis for the Presence of (e) $LiFe_3O_4$ vs. (f) $LiFeO_2$ + 2 FeO

4.5.4.1 XRD Analysis Eliminates the Presence of (e) $LiFe_3O_4$

On the ternary phase diagram, $LiFe_3O_4$ falls on the tie lie between $LiFeO_2$ + 2FeO. The $LiFe_3O_4$ phase was investigated in Chapter 2 and 97 different cation orderings for the Li+Fe on the 16c site were calculated with DFT and tested for phase stability against $LiFeO_2$ + 2 FeO. Approximately 35 of these were found stable against phase segregation to $LiFeO_2$ +

2FeO, the lowest being stable by ~5 meV/atom. The XRD predictions for the lowest energy structure for $LiFe_3O_4$ is shown in green in Figure 4.5a. As seen by the black arrows in Figure 4.5a, there are low angle peaks in the lowest energy $LiFe_3O_4$ structure that are not present in the experimental pattern.

The $LiFe_3O_4$ structure in Figure 4.5a is just one of 97 theoretical possible orderings for Li+Fe on the 16c site, and to probe if the low angle peaks are ubiquitous to $LiFe_3O_4$, or merely a function of just one cation ordering, the theoretical XRD patterns for all 97 structures are shown in Figure 4.5b. The 97 structures are grouped by stability, where the spectra color is an indicator for stability against phase segregation to $LiFeO_2$ + 2FeO. As can be seen by low angle regions highlighted with black arrows, all of the 97 $LiFe_3O_4$ structures have low angle peaks that are not observed experimentally. The alternate cation order for $LiFe_3O_4$ is allowing the lithium and iron to relax across the both 16c+16d sites, the XRD patterns for these theoretical structures still show low angle peaks not observed experimentally, and these patterns are shown in Appendix 8.

Although $LiFe_3O_4$ is predicted lower in energy than $LiFeO_2$ + 2FeO, it is not corroborated by either the XRD analysis or the neutron diffraction measurements and is eliminated as the product forming on the first voltage plateau.

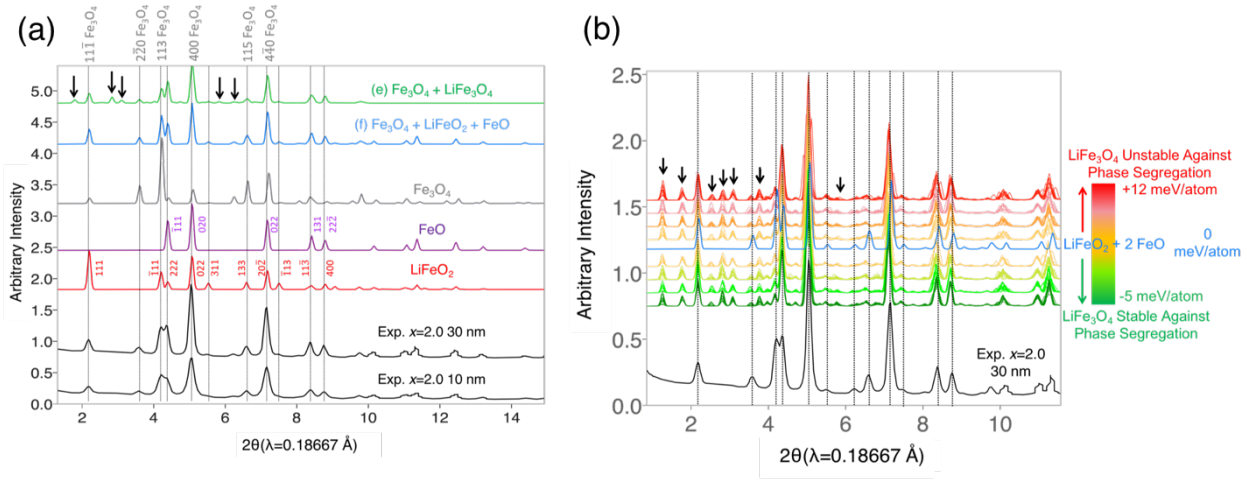

Figure 4.5: Hypotheses (e) and (f) as written in Table I but with 20% molar fraction of Fe_3O_4 included. The lattice constant for Fe_3O_4 has been adjusted to 8.4066(2) Å and 8.448(6) Å for all FeO, $LiFe_3O_4$, and $LiFeO_2$ phases. The pure phase Fe_3O_4, FeO, and $LiFeO_2$ are shown in grey, purple, and red, respectively. While all 97 theoretical cation orderings for Li+Fe on the 16 site in $[LiFe]_{16c}[Fe_2]_{16d}O_2$ are shown in (b). All $[LiFe]_{16c}[Fe_2]_{16d}O_2$ cation orderings show additional low angle peaks not observed experimentally, highlighted by black arrows. The theoretical $LiFe_3O_4$ XRD patterns are colored according to phase stability against $LiFeO_2$ + 2FeO.

4.5.4.2 XRD Analysis for the Presence of $LiFeO_2$+FeO: Hypotheses (f)

Of all hypotheses tested, (f) has the best agreement with both the experimental XRD pattern and neutron diffraction pattern as indicated in Table 4.1. The $LiFeO_2$ phase has iron on both 16c and 16d sites, but both Wyckoff sites are shared with lithium, $[Li_{0.75}Fe_{0.25}]_{16c}[Li_{0.25}Fe_{0.75}]_{16d}O_2$. As can be seen in Figure 4.5a, the pure phases for Fe_3O_4, FeO, and $LiFeO_2$ are shown in grey, purple, and red, respectively. The experimentally observed peak splitting at 4.4° is well captured by the presence of both Fe_3O_4 (113 grey) and FeO ($\bar{1}11$ purple). The low angle peaks at 2.2° and 3.6° observed experimentally are present in hypotheses (f) where 2.2° is primarily due to 111 in $LiFeO_2$ (red) and the 3.6° is due to the $2\bar{2}0$ plane in the persistent Fe_3O_4 (grey). There are small shoulders at 5.5° and 7.5° in the experimental 30 nm pattern, and these peaks can be indexed to 133 and $\bar{1}13$ $LiFeO_2$, respectively.

Despite the best agreement with XRD pattern and neutron diffraction for hypothesis (f), predicting $LiFeO_2$ + 2 FeO to be the products on the first voltage plateau, can only account for 1 of the two equivalents of lithium passed on first voltage plateau and the potential is 200 mV higher than experimentally measured. Alternately, hypothesis (g), $LiFeO_2$ + 2 FeO + Li_2O, can account for both equivalents of lithium and the potential is within 100 mV of the measured potential. The differences between the XRD patterns for hypotheses (f) and (g) are negligible, as Li_2O is transparent to X-rays, and the agreement with XRD for hypothesis (g) is considered consistent in Table 4.1.

The experimental bulk equilibrium lattice constants for FeO and $LiFeO_2$, are 8.652 Å[137] and 8.31 Å[138], respectively. In the theoretically predicted pattern in Figure 4.5a, the lattice constants for both FeO and $LiFeO_2$ have been adjusted to the experimentally measured value of 8.4484(6) Å. However, as these diffraction patterns are in 30 nm particles, the $LiFeO_2$ and FeO phases forming are not larger than tens of nanometers. It has been shown that in the case of two heterogenous domains, each on the order of 10 nm or less, the XRD pattern will erroneously indicate a homogenous solid solution, with a lattice parameter at the average value of the two heterogenous phases, although that explicit lattice spacing is not physically present in the sample.[139] Additionally, it was shown that the XRD reported lattice constant follows Vegard's law for the two heterogenous phases.[139] The Vegard's Law (rule of mixtures) lattice constant for $LiFeO_2$ + 2FeO present at this state of lithiation is 8.47 Å, close to the measured value of 8.4484(6) Å. Since the XRD pattern for $LiFeO_2$+FeO with residual Fe_3O_4 starting material matches well with both XRD and Neutron diffraction, and the particles sizes in the sample are 30 nm, these phases are most likely heterogenous but with small domain sizes, and therefore diffracting at the average of their lattice constants.

4.5.5 A Mass Balance on Lithium and the Hypothesized Reaction Pathway

The first intercalation regime into magnetite lasts from $0 < x < \sim 0.8$, where lithium inserts onto 16d cationic defects in the spinel γ-Fe_2O_3 and the spinel phase is maintained as indicated by the slope of the reversible potential in Figure 4.2 for the 30 nm particles, XRD in Figure 4.4a, and investigations in Chapter 2 and Chapter 3. When referencing the ternary phase diagram inset in Figure 4.6a, this intercalation regime is accounted for with the grey species, γ-Fe_2O_3 and corresponds to the grey DFT voltage prediction. The first phase change plateau initiates at ~0.8 equivalents of lithium discharged for 30 nm Fe_3O_4 nanoparticles and is represented by the blue pathway on the ternary phase diagram inset in Figure 4.6a, insertion into Fe_3O_4. This insertion into Fe_3O_4 lasts for $\Delta x \sim 2.0$ equivalents of lithium as can be seen by the length of the plateau in Figure 4.6a. Hypothesis (g) forms LiFeO2 + FeO + Li_2O and is corroborated by XRD, the phase change reaction can be maintained for $\Delta x = 2.0$ equivalents of lithium, and the predicted potential, 1.7 V is within 100 mV of the measured potential, 1.8 V. Neutron diffraction studies herein did not detect a crystalline Li_2O phase at $x = 2.0$, however, the measurements were not taken at the end of the first voltage plateau, and as such, ~0.25 moles of Li_2O would be formed at $x = 2.0$ as seen in in Figure 4.6b at $x_{p1} = 1.2$. Additionally, the lattice mismatch between Li_2O and the other phases forming in the nanoparticles is high, at 9.86%, 7.43%, and 10.53% for Fe_3O_4, FeO, and $LiFeO_2$, respectively, contributing to the likelihood of an amorphous and not well defined crystalline phase, which has been previously observed.[41,97]

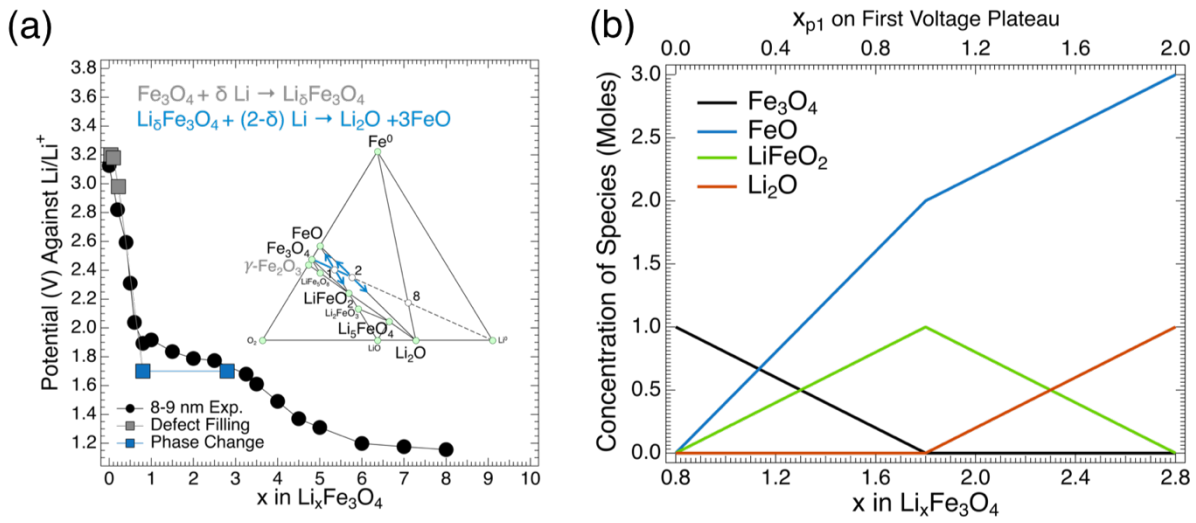

Figure 4.6: (a) DFT predicted reversible potential (squares) for lithiation of Fe_3O_4 nanoparticles compared to experimentally measured reversible potential for 8-9 nm particles (black circles).[98] Initially lithium inserts into 16d defects in the nanoparticles, DFT potentials (squares) in dark grey corresponding to insertion into γ-Fe_2O_3, dark grey phase on the ternary phase diagram inset. On the first voltage plateau, $LiFeO_2$ + FeO + Li_2O is formed (blue squares), indicated by the blue lines on the ternary phase diagram. (b) The concentrations of each phase, $LiFeO_2$ (green), FeO (blue), Li_2O (red), and Fe_3O_4(black) on the first phase plateau as a function of x in the nanoparticle (bottom axis) and as a function of lithium passed on the plateau, x_{p1} (top axis).

4.6 Chapter 4 Concluding Remarks

Magnetite is known to suffer high mass transport resistances, and local regions of high lithium concentration can result, resulting in non-thermodynamically predicted phases forming and becoming kinetically trapped. Consequently, the Fe_3O_4 nanoparticles undergo a pathway upon lithiation that does not follow the bulk-phase predicted path. Here we have discussed 9 possible pathways and determined that on the first voltage plateau, the most probable hypothesis is (g), forming $LiFeO_2$ + FeO + Li_2O, at a DFT predicted potential of 1.7 V. The lack of neutron diffraction evidence for Li_2O is likely due to the low concentration of the Li_2O phase predicted at the measured value of x=2.0 and the high lattice mismatch between Li_2O and the other phases in the sample, both of these factors that would contribute to the phase being amorphous. Additionally, this hypothesis is the most consistent when

information from XRD studies, neutron diffraction, the measured potential, and the measured plateau length are all taken into consideration. This study illustrates the importance of multidisciplinary studies for the examination of complex but engineering relevant processes such as those that occur in lithium-ion batteries. The Li-Fe-O battery system exemplifies the ubiquitous nature of metastable pathways in non-ideal systems such as nano-systems operating far from equilibrium.

CHAPTER 5: DENSITY FUNCTIONAL THEORY AND OTHER METHODOLOGIES[5]

5.1 Open Circuit Potential Measurements for Chapter 2

Electrochemical testing was done using two-electrode coin cells versus lithium metal electrodes, at 30° C. The 8-9 nm Fe_3O_4 nanoparticles were synthesized by co-precipitation using previously reported methods.[47,48] The cathodes were fabricated using the synthesized magnetite (90%), super P carbon additive (5%), and polyvinylidene fluoride binder (5%) coated onto an aluminum foil substrate. The electrolyte was formed from dimethyl carbonate and ethylene carbonate in a one-to-one ratio by volume with 1 M $LiPF_6$. Constant current lithiation at C/200 was carried out to x=0.2, 0.4, 0.5, 0.6, 0.8, 1.0, 1.5, and 2.0. Subsequent voltage monitoring under open circuit conditions for up to 30 days was performed.

5.2 Open Circuit Potential Measurements for Chapter 4

Two electrode coin cell type batteries were fabricated under Argon and tested electrochemically with methods described above. Coin cells comprised of 8, 9, or 25 nm Fe_3O_4 nanoparticles were synthesized by co-precipitation using previously reported methods.[47,48] Active material for 32 nm particles was purchased from Alfa Aesar. Constant current lithiation without preconditioning at C/200 was carried out to x = 0.2, 0.4, 0.6, and 0.8 for 9 and 25 nm samples. Each reversible potential measurement corresponded to a single coin cell experiment. The x=0.0 voltage was taken as the average resting voltage of all the coin cells before the current was turned on. After discharge, open circuit voltage

[5] This chapter was written in collaboration with Mark Hybertsen.

monitoring for up to 30 days was performed and the maximum open circuit voltage during relaxation was taken as the reversible potential for that lithiation state.

5.3 First Principles Calculations.

DFT-based calculations were performed with the Vienna *ab initio* simulation package (VASP),[129,130] using the projector augmented wave (PAW) method.[131] The generalized-gradient approximation in the form proposed by Perdew, Burke and Ernzerhof (PBE) was used for the exchange-correlation potential.[140] To approximately account for local Coulomb interactions in the Fe 3*d* orbitals, the DFT+U approach was used,[56,70] specifically in the spherical approximation.[141] In this case there is only one parameter, taken to be U_{eff}=5.3 eV for all Fe 3d orbitals, independent of nominal local ionic configuration.[95] Spin polarized calculations were performed throughout.

The plane-wave basis set was determined by a cutoff of 600 eV, chosen following tests to assure reliable relaxation of cell size based on the computed stress tensor. The reference unit cell was chosen to be the simple cubic form of the inverse spinel structure with eight formula units per cell. Where indicated, other unit cells were used. For maghemite, $Fe_{2.67}O_4$, the $P4_12_12$ structure in a 3×1×1 supercell, relative to the cubic reference, was adopted from the prior theoretical study and consistent with experiment.[103] For the reference eight formula unit Fe_3O_4 cell, the Brillouin zone sampling was done with a Γ-centered grid defined by a 3×3×3 mesh and using the Methfessel-Paxton smearing scheme of order 1 with broadening parameter 0.2 eV.[142] Sampling was adapted for other cells to be equivalent as is shown in Table 5.1. In cases where self consistency with specific d-orbital occupancy for Fe^{2+} centers was hard to achieve, a sequence of electronic minimizations was employed. First in

a Gaussian broadening scheme, the broadening parameter was reduced in steps to a much smaller value (0.01 eV) with a small or zero value of U. Then the U was incremented in steps to the final value.[143]

Table 5.1. Supercell specifications and k-point sampling: Except where noted, the supercells are nominally cubic. For cases where variable amounts of Li are indicated, the volume per cell is for the parent compound with x=0.

Compound	Number of Formula Units	Volume per oxygen (Å^3)	K-point Sampling
$Li_xFe_3O_4$	8	19.44 Å^3	3x3x3
$Li_xFe_3O_4$	16[a]	19.44 Å^3	2x2x2
$Li_xFe_{2.875}O_4$	8	19.27 Å^3	3x3x3
$Li_xFe_{2.667}O_4$	24[b]	18.94 Å^3	3x3x1
Li^0	2	40.41 Å^3	7x7x7
FeO	32	21.09 Å^3	3x3x3
α-Fe_2O_3	6[c]	23.97 Å^3	4x4x4
$LiFeO_2$	16	18.74 Å^3	3x3x3
LiO	4[d]	16.53 Å^3	8x8x3
Li_2O	32	27.40 Å^3	3x3x3
Li_5FeO_4	8	24.66 Å^3	3x3x3
$LiFe_5O_8$	3	24.96 Å^3	3x3x3

[a]Rhombohedral, [b]Tetragonal, [c]Monoclinic, [d]Hexagonal

Explicit tests indicate that these choices of energy cutoff and k-point sampling grid give total energies with convergence to about 2 meV/f.u. In general, unit cells were optimized without imposing symmetry and relaxation was carried out to an explicit force criterion of 0.05 eV/Å. For auxiliary compounds, results were similarly converged with respect to k-point sampling.

In the literature, there has been a range of chosen values of U_{eff} for magnetite, U_{eff} = 3.7-5.3 eV.[27,57,95] To probe the impact of U_{eff} on formation energy here, the reaction

$0.5LiFe_3O_4 + 0.5\ Fe_3O_4 \rightarrow Li_{0.5}Fe_3O_4$, was calculation as a function of U_{eff} in the range 0.0 to 7.0. In the range of U_{eff} = 4.5-5.7, the formation energy was found to plateau, the details of which can be seen in Figure 5.1. Our final results should not be too sensitive to the choice of U_{eff} =5.3 eV from the Materials Project.

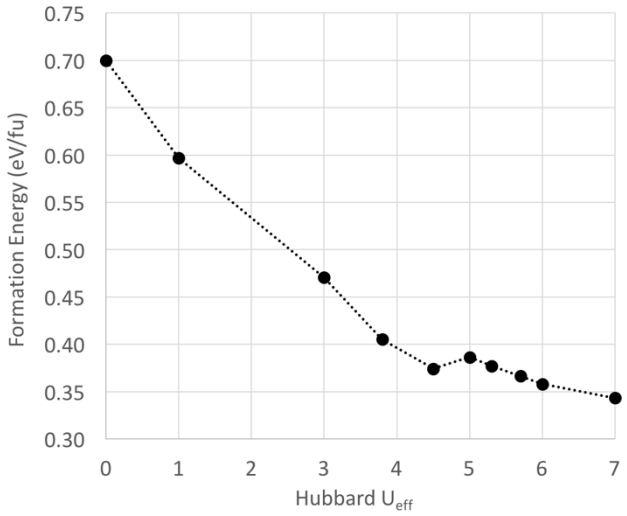

Figure 5.1: Formation energy of $Li_{0.5}Fe_3O_4$ as a function of the U_{eff} in DFT+U. To probe the effect of the Hubbard U parameter on the formation energy of lithiated iron oxides, the formation energy of $Li_{0.5}Fe_3O_4$ was calculated relative to Fe_3O_4 and $LiFe_3O_4$ in two formula unit cells for a broad range of values of U_{eff}. In the range of U_{eff} = 4.5 - 5.3 eV, the formation energy was found to vary by less than 0.03 eV/f.u.

5.4 Structural Properties for All Reference Compounds

A summary of our computed structure properties for the reference compounds in this study appears in Table 5.2.

Table 5.2: DFT+U predicted structural properties for Li-Fe-O ternary phases. Predicted structural properties for the stable phases examined in the Li-Fe-O ternary phase diagram.

	Lattice Parameters: a, b, c in Å α, β, γ in degree	Local Fe Magnetic Moments (m_b/Fe), Multiplicity, Wyckoff Site in $Fd\bar{3}m$
Fe_3O_4 Inverse Spinel	8.50, 8.50, 8.60 90.00, 90.00, 90.69	-4.2, 8, 8a 4.3, 8, 16d 3.7, 8, 16d
$Fe_{2.875}O_4$ Inverse Spinel	8.52, 8.52, 8.50 89.74, 90.26, 89.94	-4.2, 8, 8a 4.3, 10, 16d 3.7, 5, 16d
$Fe_{2.667}O_4$ Maghemite	8.47, 8.47, 25.35 90.00, 90.00, 90.00	-4.2, 24, 8a 4.3, 48, 16d
FeO	8.68, 8.68, 8.97 90.17, 90.17, 88.28	3.73, 16 -3.73, 16
α-Fe_2O_3	8.23, 8.24, 9.50 54.78, 125.24, 109.71	4.3, 8 -4.3, 8
$LiFeO_2$	8.43, 8.45, 8.43 89.90, 89.84, 89.90	4.3, 8 -4.3, 8
LiO	3.15, 3.15, 7.68 90.00, 90.00, 120.00	-
Li_2O	9.23, 9.23, 9.23 90.00, 90.00, 90.00	-
Li_5FeO_4	9.21, 9.25, 9.26 90.00, 90.00, 90.00	4.2, 8, tetrahedral
$LiFe_5O_8$	8.43, 8.43, 8.43 90.00, 90.00, 90.00	-4.2, 8 4.3, 12

5.5 Charge and Spin Order in Reference Structures

The assignment of the nominal ionic charge for discussion and analysis was based on local magnetic moment, that for Fe^{2+} being clearly distinguishable from that for Fe^{3+}. For analysis purposes, nominal ionic charges and computed, relaxed structures were used with the MADEL program from the RIETAN-FP-VENUS package to compute Madelung energies.[144]

Crystal structures were visualized using the VESTA package, which was also used to create figures with atomic structure depicted herein.[145]

The lowest energy spin configuration calculated for Fe_3O_4 was ferrimagnetic, driven by antiferromagnetic coupling between iron ions on tetrahedral 8a sites and those on octahedral 16d sites. Local magnetic moments showed Fe^{3+} (4.2 μ_b) on 8a sites and an even mixture of Fe^{3+} (4.3 μ_b) and Fe^{2+} (3.7 μ_b) on 16d sites and a net magnetic moment of 3.96 μ_b per f.u. where oxygen has non-zero magnetization. The 0K saturation magnetization for Fe_3O_4 has been found to be 4.05 μ_b/f.u.[146]

In the rock salt structure, the experimental reference compound FeO (monoclinic C2/m a = 5.2615(1) Å, b = 3.0334(1) Å, c = 3.0602 (1) Å, andα= γ=90° β= 124.649(2)° is antiferromagnetic with ordering along the <111> direction.[136,147] Experiments and DFT-based calculations have been modeled using a near-neighbor Heisenberg model.[148] The nearest neighbor Fe-Fe exchange constant J_1 (coupling through oxygen octahedral edges) is relatively weak compared to the second neighbor J_2 (coupling through corner shared oxygen with a 180° angle). Allowing for further distortion and relaxation in a four formula unit cell monoclinic cell taken from experiment,[136] resulted in local magnetic moments showing Fe^{2+} alternating $\pm$3.7 μ_b with spin alternating on <111> planes and a resulting net magnetic moment of 0.0 μ_b per f.u.

For the reference compound $LiFeO_2$, the α-$Li_2Fe_2O_4$ cubic phase with cation disorder on the 16c and 16d Wykoff sites from the $Fd\bar{3}m$ space group, $[Li_3Fe_1]_{16c}[Li_1Fe_3]_{16d}[O_8]_{32e}$ was found to be 0.54 meV/atom lower than the cation-ordered phase, $[Li_4]_{16c}[Fe_4]_{16d}[O_8]_{32e}$ and was found to be 16 meV/atom lower in energy than the competing, γ-tetragonal phase.[149]

Cation disorder was tested in a two formula unit cell where there are nine symmetry unique ways to enumerate 4 Li and 4 Fe on the 8 16c + 16d sites. Ferromagnetic coupling within <111> planes with antiferromagnetic coupling between them was found as lowest in energy, corroborated by experiment,[150] with magnetic moments $\pm 4.3\ \mu_b$.

5.6 Sampling Configurations for Lithium Insertion.

The site-occupancy disorder (SOD) tool[107] and pymatgen tool from the Materials Project[151,152] were used to determine the symmetry distinct number of configurations to sample for each structure in which specific Wyckoff position were either partially occupied or had mixed occupation.

Consider the case of $Li_xFe_3O_4$ as an example. In a two formula unit, spinel unit cell ($Fd\bar{3}m$ space group) up to two Li atoms can be inserted to available 16c sites. For x=0.5 (1 Li), there are four total configurations, but just one that is distinct based on the symmetry of the spinel parent. For x=1.0 (2 Li), there is one symmetry distinct configuration out of six. Alternatively, with all of the Fe atoms on 8a sites shifted to 16c sites, the parent has a rock-salt structure with half of the Fe sites frozen from the 16d sites of spinel and a mixed occupancy of Fe, Li and vacancies on the 16c sites. Continuing to use the Wyckoff positions from the $Fd\bar{3}m$ space group, for x=1.0, there are once again one unique configuration out of six possible. However, if the x=1.0 case is reconsidered in the $F\bar{3}m$ space group, with only one cation site for all of the Li and Fe, then there are four unique structures.

As the supercell size is increased, a more refined mesh of composition values can be studied, but the number of configurations grows rapidly. We focus on an eight formula unit cell derived from the cubic, room temperature magnetite structure. We represent both the

spinel and the rocksalt structures in the $Fd\bar{3}m$ space group. Based on the simplest possible physical model of Li insertion, the full occupancy of the 16d site is maintained (no atomic exchanges with Li considered) and Li insertion is restricted to the 16c site. We then compare two scenarios: (1) the tetrahedral Fe relaxes locally in response to the Li insertion; and (2) the tetrahedral iron is collectively displaced to 16c sites. The number of configurations, both raw and symmetry distinct, are enumerated in Table 5.3.

Table 5.3: Enumeration of configurations for LixFe3O4 in an eight formula unit cell. Total number and unique number of configurations for LixFe3O4 in an eight formula unit cell for the spinel parent with Li atoms and vacancies (V) on 16c (columns 2-3) and the rock-salt parent with the eight Fe atoms, Li atoms and vacancies (V) on 16c (columns 4-5). Symmetry of the parent compound was applied in each case without regard for charge or orbital order among the Fe^{2+} and Fe^{3+} on the fully occupied 16d sites.

	Spinel 16c: Li_nV_{16-n}		Rock-salt 16c: $Fe_8Li_nV_{8-n}$	
Li number (concentration)	Total	Unique	Total	Unique
1 (0.125)	16	1	102,960	580
2 (0.250)	120	3	360,360	1,995
3 (0.375)	560	8	720,720	3,885
4 (0.500)	1,820	22	900,900	4,879
5 (0.625)	4,368	35	720,720	3,885
6 (0.750)	8008	65	360,360	1,995
7 (0.875)	11,440	82	102,960	580
8 (1.000)	12,870	97	12,870	97

In scenario one, insertion to the spinel phase, all symmetry distinct configurations were calculated for the sequence of concentrations from x=0.125 through 0.625, at which point these structures were relatively high in energy. For the stoichiometric case of x=1.0, all 97 distinct configurations were also sampled. However, in scenario two with x=n/8 < 1.0, eight Fe, n Li and (8-n) vacancies occupied the 16c sites and the number of symmetry distinct configurations exploded. For this scenario, we used physically motivated sampling. Starting from a specific configuration for x=1, calculations were done for all symmetry distinct ways

to form one Li vacancy in the $LiFe_3O_4$ parent rock-salt structure to make $Li_{0.875}Fe_3O_4$. The lowest energy $Li_{0.875}Fe_3O_4$ result was then used as the next rock-salt parent, and all the symmetry unique ways to introduce a second lithium vacancy was sampled to make $Li_{0.75}Fe_3O_4$. This sequence was continued to lower Li concentrations as needed. To assess the robustness of this limited sampling, we repeated it for several configurations chosen from the set of 97 available for the $LiFe_3O_4$ parent rock-salt structure, rank ordered according to increasing energy. Those chosen were 1st, 2nd, 3rd, 10th, 20th, 30th, and 97th. The formation energies (Figure 5.2) suggest that this limited sampling gave reliable physical conclusions.

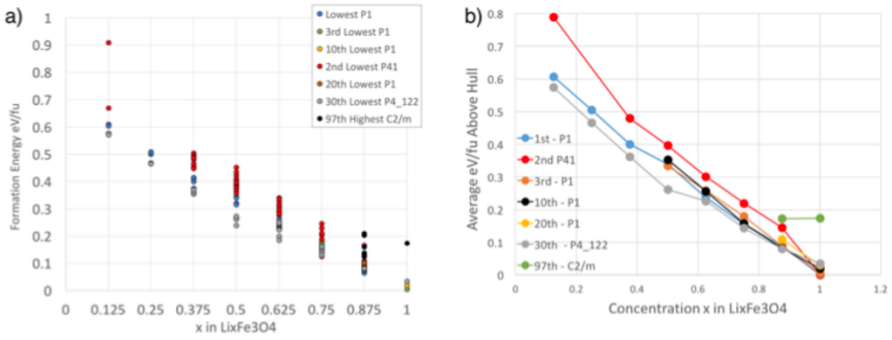

Figure 5.2**:** (a) Sampling Li-vacancy formation in the 1st, 2nd, 3rd, 10th, 20th, 30th lowest structures and the highest 97th structure of the 97 structures representing 97 symmetry unique Fe orders on the 16c sites. (b) The average energy above the convex hull is shown for all structures with a unique 16c Li:Fe parent cation order.

In the study of the effect of iron vacancies, the low Li concentration cases were considered following the analogue of scenario one, considering all symmetry distinct configurations. At the opposite limit of full Li insertion, the lowest energy *x*=1.0 rock-salt parent structure was used to introduce Fe vacancies on 16d. Iron at 1 single Fe site was exchanged for a Li for all 16d irons to calculate $Li_{1.125}Fe_{2.875}O_4$, as the parent was P_1 symmetry. The maghemite cell with 24 formula units was too large to sample configurations systematically.

5.7 Charge and Orbital Order in Fe_3O_4

The DFT calculations inherently probe the zero-temperature structure. In the case of magnetite, this includes the impact of Jahn-Teller distortions resulting from Jahn-Teller distortions around the Fe^{2+} centers and the ordering of the distribution of Fe^{2+} and Fe^{3+} among 16d sites. In a simple local picture, the distortion is specifically linked to the occupied spin down d-orbital on each Fe^{2+} site among the Jahn-Teller split t_{2g} manifold of d-states. In principle, for n formula units being sampled, there is a combinatorial factor for charge order multiplied by 3^n for orbital selection on the n Fe^{2+} sites. In practice, the lattice connectivity makes the local distortions interdependent and electronic band formation competes with the localization of the d-electrons; the problem remains quite complex.

Several groups have used DFT calculations to study charge and orbital orderings in different space group representations and supercell sizes for Fe_3O_4.[33,36,94] In this discussion, nominal charge order (Fe^{2+} and Fe^{3+}) was formally distinguished by local magnetic moment and orbital order was determined from local, projected orbital character of spin down energy states on those sites. These correlate with local octahedral volumes and distortions.[35,36] Compared to an ideal, undistorted cubic structure, the largest energy scale (~0.4 eV/f.u.) was associated with allowing distortions of local octahedral and the concomitant distortion of the unit cell and symmetry lowering.[94] A much smaller variation in energy was attributable to different ordering schemes in cells that ranged from four to 16 f.u. Starting from different experimental refinements of the low temperature magnetite structure, DFT calculations exhibit the charge and orbital ordering dictated by the pattern of octahedral distortions. The range of relaxed total energies was ~0.02 eV/f.u.[94] In a different approach, the cluster expansion concept was extended to model the charge-orbital space

more extensively.[33] The results show that structures with the original, Verwey charge order[30–32] are competitive with those based on P2/c and Cc experimental refinements that imply a different charge order, namely in the middle of the ~0.02 eV/f.u. range found previously.[94] In addition, they identified a new ordering scheme that DFT calculations indicated was a further 0.02 eV/f.u. lower in energy than the previous calculated, lowest energy for a Cc structure. So far as we are aware, these alternative orbital ordering results have not been compared to the latest experimental refinements.[35,36]

The experimental room temperature, $Fd\bar{3}m$ cubic structure includes an internal structure distortion parameter u_{iso} = 0.004[97,153] which displaces the oxygen atoms from the high symmetry 32e Wycoff positions. This results in 16c octahedra having larger volume than 16d octahedra but leaves the Fe-O bond lengths equal in each octahedron locally. We used this as a starting point for full relaxation without imposed symmetry. Upon full relaxation, the distribution of the nominal Fe^{2+} and Fe^{3+} cations on the 16d sites was found to be consistent with the Verwey charge order, where planes in the <100> direction alternate between Fe^{2+} and Fe^{3+}. For comparison, we also considered several scenarios. First, the energy gain was 0.389 eV/f.u. when going from the $Fd\bar{3}m$ cubic (a=b=c=8.54 Å and $\alpha = \beta = \gamma = 90°$) structure, with u_{iso}=0.0 and all cations fixed at their high symmetry position to the same supercell (a=b=c=8.54 Å and $\alpha = \beta = \gamma = 90°$,) but with internal parameters allowed to relax. This scale agrees with Jeng, Guo, and Huang.[154] Allowing the cell shape to distort to monoclinic (Imma) resulted in a further 0.008 eV/f.u. reduction in energy. We also calculated relaxed structures starting from low temperature P2/c experimental structure with non-Verwey charge order[34,37] and found a minimum energy that was 0.002 eV/f.u. higher than our lowest $Fd\bar{3}m$-based refinement. Visualizations of the structure, charge and orbital order

in each case appear in Figure 5.3. Overall, our computed energies for different charge and orbital orders agree with the tabulation of Zhou and Ceder.[33] Their results suggest that the larger Cc structure (16 fu) based on experiment could be 0.015 eV/f.u. lower than our lowest Fd$\bar{3}$m-based refinement.

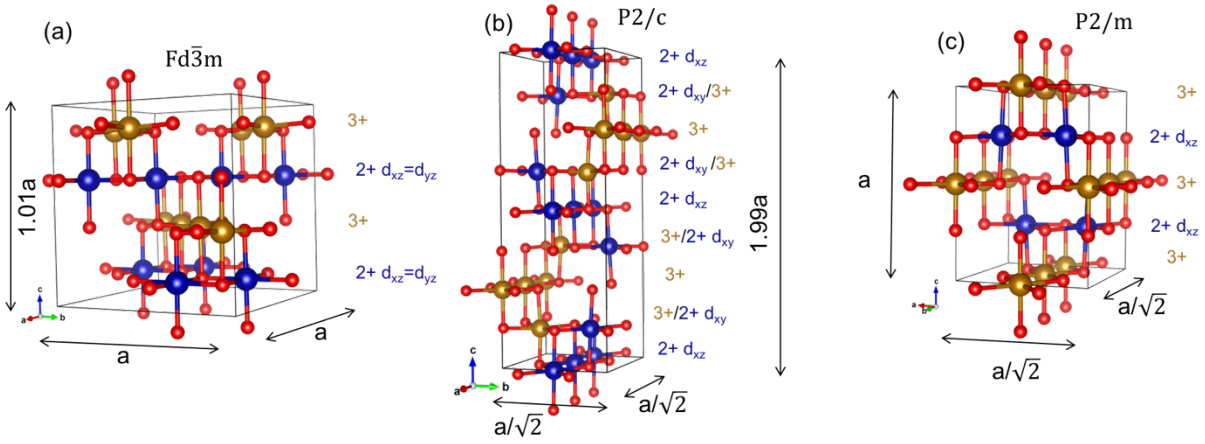

Figure 5.3**:** Spinel structure showing the 32e O atoms and the 16d octahedral Fe atoms, but suppressing the 8a tetrahedral Fe atoms for clarity. (a) Fully relaxed lowest energy charge and orbital order, found starting from the room temperature, Fd$\bar{3}$m eight formula unit cell. (b) Fully relaxed, lowest energy charge and orbital order found starting from a measured, low temperature P2/c eight formula unit cell determined by Wright, et al.[34] Alternative experimental charge order found by Wright et al. and fully relaxed herein. (c) P2/m cell with fixed cell parameters but allowed to fully relax internally.

Our study of charge and orbital order was primarily based on the eight formula unit cell determined by starting from the room temperature, Fd$\bar{3}$m cell. Our relaxed structure showed the Verwey charge order for the eight Fe^{2+} and eight Fe^{3+} formal cations on the 16d sites, visualized in Figure 5.3 a. In a local picture, the extra electron for each Fe^{2+} cation partially would occupy a spin down, three-fold-degenerate t_{2g} manifold for full octahedral symmetry. As discussed in the text, full relaxation included Jahn-Teller driven distortions locally that lifted this degeneracy. We examined the local, projected orbital character of the electronic states on the Fe^{2+} sites and in the minority spin channel. A manifold of eight states

in the local, minority spin down channel were the highest occupied states and they showed predominantly equal projections on dyz and dxz character. Correspondingly, the unit cell relaxed to one with an elongated c =8.60 Å cell parameter and a=b=8.50 Å. These results agree with those reported by Zhou and Ceder for this unit cell with Verwey charge order.[33]

Another charge order was tested by starting from the P2/c cell with eight formula units and atomic positions fitted to experiments at 90 K by Wright, et al.[34] The charge and orbital order we found is illustrated in Figure 5.3 b for the final, fully relaxed structure (a=6.04 Å, b=6.06 Å, and c=17.01 Å). Here, the charge order in the <0, 0, 1> direction showed a sequence where the first plane was Fe^{2+}, the second plane was comprised of 50:50 Fe^{2+}: Fe^{3+}, the third plane was all Fe^{3+}, and the fourth plane was 50:50 Fe^{2+}: Fe^{3+}. This charge order agrees with that found by Jeng, Guo, and Huang.[94] As noted earlier, we found this structure to be higher in energy than our $Fd\bar{3}m$ derived structure by 0.002 eV/f.u. For comparison, Zhou and Ceder[33] report an energy that is higher by 0.007 eV/f.u., similar to our result. Examining the projected, occupied minority spin orbitals on the Fe^{2+} sites, the layers comprised of only Fe^{2+} showed dxz orbital occupation and the mixed layers showed dxy orbital occupation. Jeng, Guo, and Huang saw a similar pattern of alternation of the orbitals between the layers, but within the Fe^{2+} layers, they found an additional patter of alternation between dxz and dyz.[94]

Finally, we considered a P2/m cell with four formula units, it was set to the equilibrium volume determined by the fully relaxed $Fd\bar{3}m$ cell, allowed to relaxed internally only, fixing cell shape and size (a=b=6.05 Å and c=8.50 Å). [This was done to isolate single orbital occupancy in this cell shape.] This case resulted in Verwey charge order and occupancy of just the dxz orbital on the Fe^{2+} sites, Figure 5.3 c. The energy was found to be

0.011 eV/f.u. higher than our $Fd\bar{3}m$ derived structure. The orbital order and the energy difference agree Zhou and Ceder who also report 0.011 eV/f.u.[33]

5.8 Charge Order in $LiFe_3O_4$

For $LiFe_3O_4$ in rock-salt cells under consideration here with eight Li and eight Fe distributed on the 16c sites and 16 Fe on 16d sites, there still remains the internal organization of 16 Fe^{2+} and eight Fe^{3+} cations. Starting with the oxygen sublattice from the room temperature, cubic $Fd\bar{3}m$ magnetite structure with the measured u_{iso}, we again fully relax without imposing symmetry. We find Fe^{2+} on 16c sites and an equal mixture of Fe^{2+} and Fe^{3+} on the 16d sites across all 97 unique configurations of considered. This is consistent with the positive u_{iso} imposed, which leads to larger octahedra on 16c sites. Considering as an example the lowest energy cation ordering for the $LiFe_3O_4$ structure, the energy gain in going from a u_{iso} of 0.0 to the lowest energy value of u_{iso}=0.004 was small, 0.064 eV/f.u. compared to the energy gain of allowing the internal degrees of freedom to fully relax at fixed cell parameters, (a,b,c,α, β, γ), 0.316 eV/f.u. There was an additional lowering of < 0.001 eV/f.u. for relaxation of cell parameters, a,b,c,α, β, γ. This result was globally true for other cation orderings in $LiFe_3O_4$, where the largest energy scale was the relaxation of the internal degrees of freedom.

While the sequence of energy scales for $LiFe_3O_4$ was similar to what we found for magnetite, the $LiFe_3O_4$ case is inherently different from magnetite in that the Li distribution already drives a non-uniform electrostatic environment for the 16d sites. The results reported below will show a range of 0.2 eV/f.u. across the sampling of Li configurations, an order of magnitude larger than the charge and orbital ordering scale for magnetite noted

above. Finally, to test the role of the initial choice of positive u_{iso} and the robustness of Fe^{2+} on the 16c sites, we tested several specific frozen configurations varying the u_{iso} by n* $u_{iso,exp}$, where n ranged from -2 to +2, stepped by 0.5. In the frozen configurations, the lowest energy u_{iso} was the experimental value of 0.004 in all Li+Fe 16c cation orders tested and the -2*$u_{iso,exp}$ was always the highest energy. To examine the effects of ionic relaxations and resultant charge order, the -2*$u_{iso,exp}$ was used as a starting point and allowed to fully relax for the lowest energy Li+Fe 16c cation order. The effect of the negative u_{iso} value, and resultant decreased octahedra volume, was maintained throughout the relaxation, as 7/8 of the 16c irons were relaxed to Fe^{3+}. The energy was 0.013 eV/f.u. lower than the inverted charge order case having all 16c iron Fe^{2+}. Taken together, these results suggest that the charge order and local Jahn-Teller distortions that emerged self consistently were likely representative of the lowest energy Fe charge and orbital order, although for each Li configuration, there may well be several competitive orders possible.

More broadly, for the $Li_xFe_3O_4$ cases, in either spinel or rock-salt, the same overall logic applies and the internal Fe charge and orbital order was not optimized, beyond that which was found self-consistently in fully relaxed calculations.

5.9 Phase Stability and Computation of Open Circuit Potential.

The first principles calculations have been used to predict specific electrochemical properties of the materials under study here using a conceptual framework that has been well developed and described in recent reviews.[55,134,135] More broadly, the use of DFT-based computations to assess material stability and phase diagrams has been embedded in publicly accessible databases, the Materials Project[95] and the Open Quantum Materials

Database.[155,156] The present study was restricted to zero temperature and utilized binary and ternary convex hull constructs to assess stability. Open circuit potential was estimated from total energy differences. Relevant details are briefly summarized below. Where specific materials, *e.g.*, representing a certain concentration *x* of Li in $Li_xFe_3O_4$, could adopt different arrangements, a representative range of configurations was sampled, as described in the previous subsection.

The stable phases in an insertion reaction with a nominally fixed host and a single degree of freedom were determined by the convex hull of the lowest formation energies as a function of composition calculated relative to the end-point compounds, *e.g.*,

$$E_F = E(Li_xFe_3O_4) - xE(Li_1Fe_3O_4) - (1-x)E(Fe_3O_4). \quad \text{Equation 8}$$

These energies were reported per host formula unit. For a composition range $[x_1, x_2]$ bounded by two stable phases, open circuit voltage associated to the conversion process in this range was determined by the free energy difference between the end points relative to the Li metal reservoir. This was approximated by the zero temperature energy difference, *e.g.*,

$$V = -\frac{E(Li_{x_2}Fe_3O_4) - E(Li_{x_1}Fe_3O_4) - (x_2 - x_1)E(Li)}{(x_2 - x_1)F}, \quad \text{Equation 9}$$

where *F* is Faraday's constant. Even in a composition range where the open circuit potential may vary continuously, in practice, the composition x was sampled discretely, based on the choice of supercell size. The open circuit potential was approximated by finite differences of the same form as Equation 9.

For the full ternary stability analysis, the formation energies were computed relative to the constituents in standard states (bcc Fe, bcc Li, and molecular oxygen) and reported per atom for each compound. In the ternary convex hull, such as illustrated in Figure 2.2, the test for an additional stable phase was that its formation energy be negative relative to decomposition into the nearest neighbor stable phases. For a continuous line across the phase diagram, such as that illustrating Li insertion into Fe_3O_4 in Figure 2.2, the zero temperature result for the corresponding open circuit voltage, assuming equilibrium among all possible products at each point along the path, was a series of constant values, one for each of the Gibbs triangles traversed.

5.10 DFT Corrections for Energy.

Shortcomings in the accuracy of the DFT+U approach for formation energies of compounds have been documented in the literature, with different empirical remedies suggested.[57,132,157,158] To improve the predictions based on the DFT+U approach, two types of empirical corrections are included in results returned from queries to the Materials Project. First, an overall offset in transition metal oxidation energies can be addressed by adjusting the oxygen reference energy.[57] Second, it has been argued that while the DFT+U approach is more accurate for transition metal oxides, the conventional PBE approach is more accurate for the metals themselves.[132] This has been addressed with a correction applied to each transition metal for which a finite U is applied in the oxide and determined from experimental formation energies. We have analyzed these two corrections using the known experimental formation energies for FeO, Fe_3O_4, α-Fe_2O_3, α-$LiFeO_2$, LiO, Li_2O, Li_5FeO_4, and $LiFe_5O_8$ within the Li – Fe – O ternary phase diagram (Figure 2.2).[124–126,155,156,159]

Here we detail the experimental and computed formation energies for structures used in Li-Fe-O ternary phase diagram (Figure 2.2) and the methodology for empirical corrections to DFT+U formation energies. The summary of the final information appears in Table 5.4. All experimental values are at standard conditions unless otherwise noted. Theoretical formation energies are from the Open Quantum Materials Database (OQMD)[156], the Materials Project Database[95], and the theoretical formation energies computed here.

Table 5.4. Formation energies for known compounds in the Li-Fe-O phase diagram from experiment, Materials Project Database, and OQMD compared to the formation energies computed herein with DFT+U methods only and then the GGA/GGA+U corrected formation energies computed herein.

Compound	Experimental ΔH (eV/atom)	Theory from Materials Project (eV/atom)	Theory from OQMD Database (eV/atom)	Computed with DFT +U (eV/atom)	Computed with Corrections (eV/atom)	Materials Project Material Id
FeO	-1.42[125]	-1.67	-1.52	-1.92	-1.46	mp-715262
Fe_3O_4	-1.67[125]	-1.84	-1.64	-1.97	-1.66	mp-19306
α-Fe_2O_3	-1.72[125]	-1.89	-1.65	-1.97	-1.71	mp-715572
γ-Fe_2O_3*	-1.68[124]	-	-	-1.94	-1.68	-
$LiFeO_2$	-1.94[126]	-2.08	-1.93	-2.03	-1.93	mp-851027
LiO	-1.65[125]	-1.65	-1.62	-1.45	-1.71	mp-841
Li_2O	-2.08[125]	-2.07	-1.98	-1.88	-2.05	mp-1960
Li_5FeO_4	-2.04[126]	-2.10	-2.00	-1.97	-2.04	mp-19511
$LiFe_5O_8$	-1.80[126]	-1.90	-1.73	-2.00	-1.79	mp-31768

All structures in Table 5.4, except those for FeO, $LiFeO_2$, and γ-Fe_2O_3, were obtained from the Materials Project Database and fully relaxed with methods described in Chapter 5.3. The two corrections applied to the DFT+U results are related to the formation energy of O_2 and mixing of GGA with GGA+U calculations for calculation of reaction energies where appropriate. Previously, the correction for O_2 has been found to be a constant shift in the O_2

formation energy by Wang, et al. [57] The second correction traces to the basic idea that GGA gives better overall reaction energies or predictions of stability for metals while GGA+U gives better results for transition metal oxides. When both cases are involved in a reaction energy, e.g., BCC-Fe and iron oxides, a scheme has been developed using appropriate thermodynamic cycles to correct the reaction energies that scales with the amount of metal reduction.[132] To capture both of these corrections for the dataset encapsulated by the Li-Fe-O ternary phase diagram, we have used a two-parameter least-squares regression to all the data in Table 5.4, unless denoted with an asterisk. With this regression, we have fit 1.06 eV/O_2 and 2.47 eV/Fe. For comparison, the previously published corrections, determined by fitting to a broader set of data at a different U_{eff} (4.0 eV for Fe) were 1.36 eV/O_2[57] and 1.723 eV/Fe.[132] Our formation energies without and with corrections are shown in the 5th and 6th columns of Table 5.4, respectively. Figure 5.4 illustrates the impact of the corrections on the formation energies following a path through part of the phase diagram. Generally, the stability criterion itself is not affected, but the open circuit voltage is changed for processes in which Fe^0 is a reaction product.

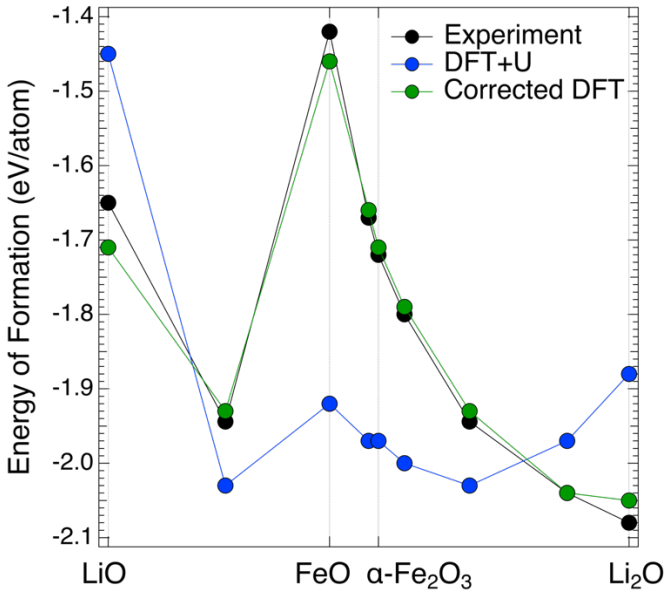

Figure 5.4. A 2D line plot through the ternary phase diagram traversing LiO → FeO → α-Fe_2O_3→ Li_2O, distance on the x-axis is proportional to distance on the ternary phase diagram. Li_2FeO_3 was not calculated and is not included in the 2D line plot. Illustration of the accuracy of Formation energies as calculated by GGA+U alone, or calculated with the O_2 and GGA/GGA+U corrections adapted from Jain et al. and Wang et al. The corrections were determined by a least squares fitting regression to experimental data shown in Table 5.4.

5.11 DFT Corrections for Volume.

Corrections to the DFT volume were applied in a similar method as the corrections to the formation energies described in the previous section, Chapter 5.10. The generalized gradient approximation used in the DFT calculations herein is known to overestimate the volume and therefore the lattice constant of the calculated phases. In order to compare to experimentally measured lattice constants, a correction was applied to the DFT-predicted structure volume. For phases in the Li-Fe-O ternary space studied in Chapter 5.10, where room temperature lattice constants were available, a correction in the lattice constant was determined, and then applied to the DFT structures for which there are no experimental data. For each compound, the lattice constant in a nominally cubic cell was determined from the volume of the calculated cell. Similarly, a cubic lattice constant was determined for all

experimental cells and the two values were compared. On average, DFT was found to overestimate the cubic lattice constant by +1.3% amounting to an average lattice constant increase of +0.11 Å for the cubic cell parameter a. The average expansion per Fe in the cubic cell was then used to correct the DFT predicted lattice constants, bringing the average predicted increase in expansion of lattice constant down to 0.03% for the corrected data. Details of the compounds and lattice constants used for this correction can be found in Table 5.5.

Table 5.5. Corrections to DFT calculated lattice constants. The experimental lattice constants were taken from entries in the Karlsruhe Crystallographic database as indicated by the ICSD number in the last column, or from the reference indicated in the last column. The DFT+U calculated lattice constants are in the second column, where the lattice constant was calculated as the cube root of the DFT determined volume calculated in a cubic cell.

Compound	Experimental Room Temp. Lattice Constant (Å)	DFT+U Calculated Lattice Constant (Å)	Percent Error as Calculated	Corrected Lattice Constant (Å)	Percent Error after Correction	ICSD or Citation for Exp. Lattice Constant
$LiFe_5O_8$	8.3172	8.4429	1.33%	8.3171	-0.017%	75525
$LiFeO_2$	8.3136	8.4321	1.42%	8.3422	0.344%	Abdel-Dheny 2012
Fe_3O_4	8.3958	8.5381	1.69%	8.4032	0.086%	633041, 82237, 633018, 82234
FeO	8.6515	8.7727	1.39%	8.5930	-0.682%	82233
$Fe_{2.67}O_4$	8.3419	8.4622	1.44%	8.3423	-0.005%	Goss 1988
Li_5FeO_4	9.1966	9.24	0.472%	9.1951	-0.017%	30718

CHAPTER 6: CONCLUDING REMARKS

6.1 The Use of DFT in Elucidating Complex Electrochemical Processes

Density functional theory has shown to be an invaluable tool for theorists to probe questions that we may not otherwise be able to fully understand with experimental techniques alone. In the case of electrochemistry, one of the most natural applications of DFT to lithium-ion batteries is the computation of the equilibrium voltages and the reversible potential, as DFT is a ground-state theory. When trying to understand a battery, the most relevant regime is the behavior occurring during operation, which takes place far from equilibrium. In this way, the use of DFT to map out the ground state structures and corresponding reversible potential creates a definition for 'ideal' for a given battery system, from which we can measure and track deviations from during battery operation.

6.2 The Value of DFT in Understanding of Entire Device Operation

Density functional theory is not equipped to model an entire battery due to size and complexity of the problem, and instead, coarse grained continuum methods are more appropriate for capturing the behavior of the whole device. When modeling the whole battery, the deviation from ideality and equilibrium is the property that must be most accurately described. The most important deviations from ideality are the performance limiting ones, and often the limitations do not occur in the bulk of the material, but rather at the junctions and interfaces where nonideality dictates. The strengths of DFT when relating to understanding of an operational battery is the insight into the physics occurring at the atomic scale, including the interfaces and junctions within the system. Determination of the

performance relevant atomic scale processes creates an opportunity to make connections between the atomic scale and the macroscopic scale.

6.3 The Insights DFT has Afforded for Nanostructured Magnetite

One of the allures of nanostructuring a material is the inherent deviation from ideality that occurs as a function of the nanostructure. Surface area to volume ratios, unimportant in bulk materials, become the modulator for the performance of the nanostructured material, and processes that plague the bulk material can disappear entirely. In Chapter 2, the energetics of lithium insertion into magnetite was explored. However, treatment of magnetite alone fails to capture the experimentally observed electrochemical performance of the system and the energetics of defective magnetite and maghemite were also examined. Atomic lattice defects are prevalent in magnetite, especially as the material is nanostructured, and through theoretical inquiry, it became evident that these defects are relevant to the electrochemistry of the material.

In Chapter 3, it becomes evident that the implications of the defects on the electrochemical behavior of the material are exaggerated as the magnetite nanoparticle size is decreased. In both Chapter 2 and Chapter 3, identifying and quantifying the defects has elucidated the mechanism for lithiation in the intercalation regime in the reversible potential and enabled a deeper understanding of how the nanostructured material accepts lithium while operating in a lithium-ion battery. In Chapter 4, DFT was utilized to probe not only the ground state structures for $Li_xFe_3O_4$, but also to explore pathways that are metastable. This chapter illustrates further deviation from ideality in Fe_3O_4 nanoparticles, as the phase changes that occur on the first voltage plateau are not the ones predicted for the bulk material.

The aim of this thesis was to put forth a comprehensive theoretical examination for the lithiation of magnetite, magnetite nanoparticles, and the structural derivatives of magnetite that co-exist with the material under physically realistic conditions. This thesis also aims to make ties between phenomena occurring on the atomic scale and the measurable properties of the macroscopic system, such as voltage. It was illustrated that as a function of particle size, the magnetite system can vary in its atomic structure and the resultant electrochemistry and phase change characteristics are both affected. The findings indicate the importance of the details of the nanostructure in magnetite to the observed and measured electrochemical properties of the material and the findings act as a case study for a system in which inquiry into the atomic scale shed insight into macroscopically observed electrochemical behavior.

BIBLIOGRAPHY

(1) Whittingham, M. S. Electrical Energy Storage and Intercalation Chemistry. *Science (80-.).* **1976**, *192* (4244), 1126–1127.

(2) Dow, K.; Downing, T. *The Greenhouse Effect.*, 3rd ed.; University of California Press, 2011.

(3) U. S. Energy Facts http://www.eia.gov/energyexplained/ (accessed Aug 18, 2015).

(4) International Energy Agency http://www.iea.org/statistics/ (accessed May 1, 2017).

(5) Yang, Z.; Zhang, J.; Kintner-Meyer, M. C. W.; Lu, X.; Choi, D.; Lemmon, J. P.; Liu, J. Electrochemical Energy Storage for Green Grid. *Chem. Rev.* **2011**, *111* (5), 3577–3613.

(6) Tromly, K. *Renewable Energy: An Overview*; 2001.

(7) Chen, H.; Cong, T. N.; Yang, W.; Tan, C.; Li, Y.; Ding, Y. Progress in Electrical Energy Storage System: A Critical Review. *Prog. Nat. Sci.* **2009**, *19* (3), 291–312.

(8) Whittingham, M. S. Introduction: Batteries. *Chem. Rev.* **2014**, *114* (23), 11413–11413.

(9) Huggins, R. A. Energy Storage in Batteries. In *Understanding Batteries*; Dell, R. M., Rand, D. A. J., Eds.; 2001.

(10) Oliveira, L.; Messagie, M.; Mertens, J.; Laget, H.; Coosemans, T.; Van Mierlo, J. Environmental Performance of Electricity Storage Systems for Grid Applications, a Life Cycle Approach. *Energy Convers. Manag.* **2015**, *101*, 326–335.

(11) Nitta, N.; Wu, F.; Lee, J. T.; Yushin, G. Li-Ion Battery Materials: Present and Future. *Mater. Today* **2014**, *18* (5), 252–264.

(12) Bock, D. C.; Kirshenbaum, K. C.; Wang, J.; Zhang, W.; Wang, F.; Wang, J.; Marschilok, A. C.; Takeuchi, K. J.; Takeuchi, E. S. 2D Cross Sectional Analysis and Associated Electrochemistry of Composite Electrodes Containing Dispersed Agglomerates of

Nanocrystalline Magnetite, Fe 3 O 4. *ACS Appl. Mater. Interfaces* **2015**, *7* (24), 13457–13466.

(13) Whittingham, M. S. History, Evolution, and Future Status of Energy Storage. *Proc. IEEE* **2012**, *100* (Special Centennial Issue), 1518–1534.

(14) Newman, J.; Thomas-Alyea, K. E. *Electrochemical Systems*, 3rd ed.; John Wiley & Sons, Inc.: Hookben, New Jersey, 2004.

(15) Cabana, J.; Monconduit, L.; Larcher, D.; Palacín, M. R.; Palacin, M. R. Beyond Intercalation-Based Li-Ion Batteries: The State of the Art and Challenges of Electrode Materials Reacting through Conversion Reactions. *Adv. Mater.* **2010**, *22* (35), 170–192.

(16) Ong, M. T.; Verners, O.; Draeger, E. W.; Duin, A. C. T. Van; Lordi, V.; Pask, J. E.; van Duin, A. C. T.; Lordi, V.; Pask, J. E. Lithium Ion Solvation and Diffusion in Bulk Organic Electrolytes from First-Principles and Classical Reactive Molecular Dynamics. *J. Phys. Chem. B* **2014**, *8* (4), 1535–1545.

(17) Park, M.; Zhang, X.; Chung, M.; Less, G. B.; Sastry, A. M. A Review of Conduction Phenomena in Li-Ion Batteries. *J. Power Sources* **2010**, *195*, 7904–7929.

(18) Chen, Y.-H.; Wang, C.-W.; Liu, G.; Song, X.-Y.; Battaglia, V. S.; Sastry, a. M. Selection of Conductive Additives in Li-Ion Battery Cathodes. *J. Electrochem. Soc.* **2007**, *154* (10), A978.

(19) Guo, Y. G.; Hu, J. S.; Wan, L. J. Nanostructured Materials for Electrochemical Energy Conversion and Storage Devices. *Adv. Mater.* **2008**, *20* (15), 2878–2887.

(20) Aricò, A. S.; Bruce, P.; Scrosati, B.; Tarascon, J.-M.; van Schalkwijk, W. Nanostructured Materials for Advanced Energy Conversion and Storage Devices. *Nat. Mater.* **2005**, *4* (5), 366–377.

(21) Zhang, Z.; Satpathy, S. Electron-States, Magnetism, and the Verwey Transition in Magnetite. *Phys. Rev. B* **1991**, *44* (24), 13319–13331.

(22) Mattis, D. C. *The Theory of Magnetism*; Springer: Berlin, 1988.

(23) Pankhurst, Q. A.; Thanh, N. K. T.; Jones, S. K.; Dobson, J. Progress in Applications of Magnetic Nanoparticles in Biomedicine. *J. Phys. D. Appl. Phys.* **2009**, *42* (22).

(24) Kim, J.; Kim, H. S.; Lee, N.; Kim, T.; Kim, H.; Yu, T.; Song, I. C.; Moon, W. K.; Hyeon, T. Multifunctional Uniform Nanoparticles Composed of a Magnetite Nanocrystal Core and a Mesoporous Silica Shell for Magnetic Resonance and Fluorescence Imaging and for Drug Delivery. *Angew. Chemie - Int. Ed.* **2008**, *47* (44), 8438–8441.

(25) Magela, G.; Blanco-andujar, C.; Grave, E. De; Pankhurst, Q. a. Magnetic Nanoparticles For In Vivo Use : A Critical Assessment of Their Composition Magnetic Nanoparticles for in Vivo Use : A Critical Assessment of Their Composition. **2014**, *44* (1), 1–31.

(26) Yang, T.; Wen, X.-D.; Li, Y.-W.; Wang, J.; Jiao, H. Interaction of Alkali Metals with the Fe3O4(111) Surface. *Surf. Sci.* **2009**, *603* (1), 78–83.

(27) Santos-Carballal, D.; Roldan, A.; Grau-Crespo, R.; de Leeuw, N. H. A DFT Study of the Structures, Stabilities and Redox Behaviour of the Major Surfaces of Magnetite Fe3O4. *Phys. Chem. Chem. Phys.* **2014**, *16*, 21082–21097.

(28) Yu, X.; Tian, X.; Wang, S. Adsorption of Ni, Pd, Pt, Cu, Ag and Au on the Fe3O4(111) Surface. *Surf. Sci.* **2014**, *628*, 141–147.

(29) Sickafus, K. E.; Wills, J. M. Structure of Spinel. *J. Am. Ceram. Soc.* **1999**, *82* (12), 3279–3292.

(30) Verwey, E. J. W. Electronic Conduction of Magnetite (Fe3O4) and Its Transition Point at Low Temperatures. *Nature* **1939**, *144* (3642), 327–328.

(31) Verwey, E. J. W.; Haayman, P. W. Electronic Conductivity and Transition Point of Magnetite ("Fe3O4") . *Phys. Rev. B* **1941**, *8* (9), 979–987.

(32) Walz, F. The Verwey Transition - a Topical Review. *J. Phys. Condens. Matter* **2002**, *14* (12), R285–R340.

(33) Zhou, F.; Ceder, G. First-Principles Determination of Charge and Orbital Interactions in Fe3O4. *Phys. Rev. B - Condens. Matter Mater. Phys.* **2010**, *81* (20), 3–8.

(34) Wright, J. P.; Attfield, J. P.; Radaelli, P. G. Charge Ordered Structure of Magnetite Fe3O4 below the Verwey Transition. *Phys. Rev. B* **2002**, *66* (21), 214422.

(35) Senn, M. S.; Wright, J. P.; Attfield, J. P. Charge Order and Three-Site Distortions in the Verwey Structure of Magnetite. *Nature* **2011**, *481* (7380), 173–176.

(36) Senn, M. S.; Loa, I.; Wright, J. P.; Attfield, J. P. Electronic Orders in the Verwey Structure of Magnetite. *Phys. Rev. B* **2012**, *85* (12), 125119.

(37) Wright, J. P.; Attfield, J. P.; Radaelli, P. G. Long Range Charge Ordering in Magnetite below the Verwey Transition. *Phys. Rev. Lett.* **2001**, *87* (26), 266401.

(38) Thackeray, M. M.; David, W. I. F.; Goodenough, J. B. Structural Characterization of the Lithiated Iron Oxides LixFe304 AND LixFe203 (0<x<2). *Mater. Res. Bull.* **1982**, *17*, 785–793.

(39) Doeff, M. M. Battery Cathodes. In *Batteries for Sustainability: Selected Entries from the Encyclopedia of Sustainability Science and Technology*; Meyers, R. A., Ed.; 2013; pp 5–49.

(40) Knehr, K. W.; Brady, N. W.; Cama, C. A.; Bock, D. C.; Lin, Z.; Lininger, C. N.; Marschilok, A. C.; Takeuchi, K. J.; Takeuchi, E. S.; West, A. C. Modeling the Mesoscale Transport of Lithium-Magnetite Electrodes Using Insight from Discharge and Voltage Recovery

Experiments. *J. Electrochem. Soc.* **2015**, *162* (14), A2817–A2826.

(41) He, K.; Zhang, S.; Li, J.; Yu, X.; Meng, Q.; Zhu, Y. Y.; Hu, E.; Sun, K.; Yun, H.; Yang, X.-Q.; Zhu, Y. Y.; Gan, H.; Mo, Y.; Stach, E. A.; Murray, C. B.; Su, D. Visualizing Non-Equilibrium Lithiation of Spinel Oxide via in Situ Transmission Electron Microscopy. *Nat. Commun.* **2016**, *7* (May), 11441.

(42) Islam, M. S.; Catlow, C. R. A. Lithium Insertion into Fe3O4. *J. Solid State Chem.* **1988**, *77* (1), 180–189.

(43) Thackeray, M. M.; David, W. I. F.; Goodenough, J. B. Structural Characterization of the Lithiated Iron Oxides LixFe3O4 and LixFe2O3 (0<x<2). *Mater. Res. Bull.* **1982**, *17* (6), 785–793.

(44) Zhang, W.; Bock, D. C.; Pelliccione, C. J.; Li, Y.; Wu, L.; Zhu, Y.; Marschilok, A. C.; Takeuchi, E. S.; Takeuchi, K. J.; Wang, F. Insights into Ionic Transport and Structural Changes in Magnetite during Multiple-Electron Transfer Reactions. *Adv. Energy Mater.* **2016**, *6* (10), 1502471.

(45) Bock, D. C.; Pelliccione, C. J.; Zhang, W.; Timoshenko, J.; Knehr, K. W.; West, A. C.; Wang, F.; Li, Y.; Frenkel, A. I.; Takeuchi, E. S.; Takeuchi, K. J.; Marschilok, A. C. Size Dependent Behavior of Fe3O4 Crystals during Electrochemical (de)Lithiation: An in Situ X-Ray Diffraction, Ex Situ X-Ray Absorption Spectroscopy, Transmission Electron Microscopy and Theoretical Investigation. *Phys. Chem. Chem. Phys.* **2017**, *19* (31), 20867–20880.

(46) Komaba, S.; Mikumo, T.; Yabuuchi, N.; Ogata, A.; Yoshida, H.; Yamada, Y. Electrochemical Insertion of Li and Na Ions into Nanocrystalline Fe3O4 and α-Fe2O3 for Rechargeable Batteries. *J. Electrochem. Soc.* **2010**, *157* (1), A60–A65.

(47) Zhu, S.; Marschilok, A. C.; Takeuchi, E. S.; Takeuchi, K. J. Crystallite Size Control and Resulting Electrochemistry of Magnetite, Fe3O4. *Electrochem. Solid-State Lett.* **2009**, *12* (4), A91.

(48) Zhu, S.; Marschilok, A. C.; Takeuchi, E. S.; Yee, G. T.; Wang, G.; Takeuchi, K. J. Nanocrystalline Magnetite: Synthetic Crystallite Size Control and Resulting Magnetic and Electrochemical Properties. *J. Electrochem. Soc.* **2010**, *157* (11), A1158–A1163.

(49) Bock, D. C.; Pelliccione, C. J.; Zhang, W.; Wang, J.; Knehr, K. W.; Wang, J.; Wang, F.; West, A. C.; Marschilok, A. C.; Takeuchi, K. J.; Takeuchi, E. S. Dispersion of Nanocrystalline Fe3O4 within Composite Electrodes: Insights on Battery-Related Electrochemistry. *ACS Appl. Mater. Interfaces* **2016**, *8* (18), 11418–11430.

(50) Shi, Y.; Zhang, J.; Bruck, A. M.; Zhang, Y.; Li, J.; Stach, E. A.; Takeuchi, K. J.; Marschilok, A. C.; Takeuchi, E. S.; Yu, G. A Tunable 3D Nanostructured Conductive Gel Framework Electrode for High-Performance Lithium Ion Batteries. *Adv. Mater.* **2017**, *29* (22).

(51) Thackeray, M. M.; Depicciotto, L. A.; Dekock, A.; Johnson, P. J.; Nicholas, V. A.; Adendorff, K. T.; de Picciotto, L. A.; de Kock, A.; Johnson, P. J.; Nicholas, V. A.; Adendorff, K. T. Spinel Electrodes for Lithium Batteries - A Review. *J. Power Sources* **1987**, *21* (1), 1–8.

(52) Knehr, K. W.; Brady, N. W.; Lininger, C. N.; Cama, C. A.; Bock, D. C.; Lin, Z.; Marschilok, A. C.; Takeuchi, K. J.; Takeuchi, E. S.; West, A. C. Mesoscale Transport in Magnetite Electrodes for Lithium-Ion Batteries. *ECS Trans.* **2015**, *69* (1), 7–19.

(53) Ceder, G.; Aydinol, M. K.; Kohan, A. F. Application of First-Principles Calculations to the Design of Rechargeable Li Batteries. *Comput. Mater. Sci.* **1997**, *8* (1&2), 161–169.

(54) Benco, L.; Barras, J.-L.; Atanasov, M.; Daul, C. A.; Deiss, E. First-Principles Prediction of Voltages of Lithiated Oxides for Lithium-Ion Batteries. *Solid State Ionics* **1998**, *112*

(3,4), 255–259.

(55) Urban, A.; Seo, D.-H.; Ceder, G. Computational Understanding of Li-Ion Batteries. *npj Comput. Mater.* **2016**, *2* (1), 16002.

(56) Anisimov, V. I.; Aryasetiawan, F.; Lichtenstein, A. I. First-Principles Calculations of the Electronic Structure and Spectra of Strongly Correlated Systems: The LDA + U Method. *J. Phys. Condens. Matter* **1997**, *9* (4), 767–808.

(57) Wang, L.; Maxisch, T.; Ceder, G. Oxidation Energies of Transition Metal Oxides within the GGA+U Framework. *Phys. Rev. B* **2006**, *73* (19), 195107.

(58) Liu, X.; Wang, D.; Liu, G.; Srinivasan, V.; Liu, Z.; Hussain, Z.; Yang, W. Distinct Charge Dynamics in Battery Electrodes Revealed by in Situ and Operando Soft X-Ray Spectroscopy. *Nat. Commun.* **2013**, *4* (May), 1–8.

(59) Ceder, G.; Ven, A. Van Der. Phase Diagrams of Lithium Transition Metal Oxides : Investigations from First Principles. *Electrochim. Acta* **1999**, *45*, 131–150.

(60) Abraham, A.; Housel, L. M.; Lininger, C. N.; Bock, D. C.; Jou, J.; Wang, F.; West, A. C.; Marschilok, A. C.; Takeuchi, K. J.; Takeuchi, E. S. Investigating the Complex Chemistry of Functional Energy Storage Systems: The Need for an Integrative, Multiscale (Molecular to Mesoscale) Perspective. *ACS Cent. Sci.* **2016**, *2* (6), 380–387.

(61) Menard, M. C.; Takeuchi, K. J.; Marschilok, A. C.; Takeuchi, E. S. Electrochemical Discharge of Nanocrystalline Magnetite: Structure Analysis Using X-Ray Diffraction and X-Ray Absorption Spectroscopy. *Phys. Chem. Chem. Phys.* **2013**, *15* (42), 18539–18548.

(62) Arora, P. Capacity Fade Mechanisms and Side Reactions in Lithium-Ion Batteries. *J. Electrochem. Soc.* **1998**, *145* (10), 3647.

(63) Wohlfahrt-Mehrens, M.; Vogler, C.; Garche, J. Aging Mechanisms of Lithium Cathode Materials. *J. Power Sources* **2004**, *127* (1–2), 58–64.

(64) Ito, S.; Nakaoka, K.; Kawamura, M.; Ui, K.; Fujimoto, K.; Koura, N.; Kawamura, A.; Ui, K.; Fujimoto, K.; Koura, N. Lithium Battery Having a Large Capacity Using Fe3O4 as a Cathode Material. *J. Power Sources* **2005**, *146* (1–2), 319–322.

(65) Martin, R. M. *Electronic Stucture: Basic Theory and Practical Methods*, 2nd ed.; The Press Syndicate of the University of Cambridge: Cambridge, 2004.

(66) Himmetoglu, B.; Floris, A.; De Gironcoli, S.; Cococcioni, M. Hubbard-Corrected DFT Energy Functionals: The LDA+U Description of Correlated Systems. *Int. J. Quantum Chem.* **2014**, *114* (1), 14–49.

(67) Sciences, B. E.; Bes, T.; Energy, B.; Advisory, S.; Future, S. E.; Challenge, G. From Quantum to Continuum, Opportunities for Mesoscale Science.

(68) Gramsch, S.; Cohen, R.; Savrasov, S. Structure, Metal-Insulator Transitions, and Magnetic Properties of FeO at High Pressures. *Am. Mineral.* **2003**, *88* (2–3), 257–261.

(69) Brandow, B. H. Theory of Mott Insulators. *Int. J. Quantum Chem.* **2009**, *10* (S10), 417–434.

(70) Anisimov, V. I.; Zaanen, J.; Andersen, O. K. Band Theory and Mott Insulators: Hubbard U Instead of Stoner I. *Phys. Rev. B* **1991**, *44* (3), 943–954.

(71) Fang, Z.; Solovyev, I.; Sawada, H.; Terakura, K. First-Principles Study on Electronic Structures and Phase Stability of MnO and FeO under High Pressure. *Phys. Rev. B* **1999**, *59* (2), 762–774.

(72) Dudarev, S. L.; Botton, G. A.; Savrasov, S. Y.; Szotek, Z.; Temmerman, W. M.; Sutton, A. P. Electronic Structure and Elastic Properties of Strongly Correlated Metal Oxides from

First Principles: LSDA + U, SIC-LSDA and EELS Study of UO2 and NiO. *Phys. status solidi* **1998**, *166* (1), 429–443.

(73) Bousquet, E.; Spaldin, N. J Dependence in the LSDA+U Treatment of Noncollinear Magnets. *Phys. Rev. B - Condens. Matter Mater. Phys.* **2010**, *82* (22), 1–4.

(74) Thackeray, M. M. Spinel Electrodes for Lithium Batteries. *J. Am. Ceram. Soc.* **1999**, *82* (12), 3347–3354.

(75) Poizot, P.; Laruelle, S.; Grugeon, S.; Dupont, L.; Tarascon, J. M. Nano-Sized Transition-Metal Oxides as Negative-Electrode Materials for Lithium-Ion Batteries. *Nature* **2000**, *407* (6803), 496–499.

(76) Whittingham, M. S. Lithium Batteries and Cathode Materials. *Chem. Rev.* **2004**, *104* (10), 4271–4301.

(77) Godshall, N. A.; Raistrick, I. D.; Huggins, R. A. Thermodynamic Investigations of Ternary Lithium-Transition Metal-Oxygen Cathode Materials. *Mater. Res. Bull.* **1980**, *15* (5), 561–570.

(78) Thackeray, M. M.; David, W. I. F.; Goodenough, J. B. High-Temperature Lithiation of α-Fe203: A Mechanistic Study. *J. Solid State Chem.* **1984**, *55* (3), 280–286.

(79) Chen, C. J.; Greenblatt, M.; Waszczak, J. V. Lithium Insertion Compounds of LiFe5O8, Li2FeMn3O8, and Li2ZnMn3O8. *J. Solid State Chem.* **1986**, *64* (3), 240–248.

(80) Chen, C. J.; Greenblatt, M.; Waszczak, J. V. Lithium Insertion into Spinel Ferrites. *Solid State Ionics* **1986**, *18* (Part 2), 838–846.

(81) de Picciotto, L. A.; Thackeray, M. M. Lithium Insertion into the Spinel LiFe5O8. *Mater. Res. Bull.* **1986**, *21* (5), 583–592.

(82) Pernet, M.; Strobel, P.; Bonnet, B.; Bordet, P.; Chabre, Y. Structural and Electrochemical

Study of Lithium Insertion into γ-Fe2O3. *Solid State Ionics* **1993**, *66* (3–4), 259–265.

(83) Kanzaki, S.; Inada, T.; Matsumura, T.; Sonoyama, N.; Yamada, A.; Takano, M.; Kanno, R. Nano-Sized γ-Fe2O3 as Lithium Battery Cathode. *J. Power Sources* **2005**, *146* (1), 323–326.

(84) Taberna, P. L.; Mitra, S.; Poizot, P.; Simon, P.; Tarascon, J.-M. High Rate Capabilities Fe3O4-Based Cu Nano-Architectured Electrodes for Lithium-Ion Battery Applications. *Nat. Mater.* **2006**, *5* (7), 567–573.

(85) Kanzaki, S.; Yamada, A.; Kanno, R. Effect of Chemical Oxidation for Nano-Size Gamma-Fe2O3 as Lithium Battery Cathode. *J. Power Sources* **2007**, *165* (1), 403–407.

(86) Zhang, W. M.; Wu, X. L.; Hu, J. S.; Guo, Y. G.; Wan, L. J. Carbon Coated Fe3O4 Nanospindles as a Superior Anode Material for Lithium-Ion Batteries. *Adv. Funct. Mater.* **2008**, *18* (24), 3941–3946.

(87) Hirayama, M.; Tomita, H.; Kubota, K.; Kanno, R. Structure and Electrode Reactions of Layered Rocksalt LiFeO2 Nanoparticles for Lithium Battery Cathode. *J. Power Sources* **2011**, *196* (16), 6809–6814.

(88) Bruck, A. M.; Cama, C. A.; Gannett, C. N.; Marschilok, A. C.; Takeuchi, E. S.; Takeuchi, K. J. Nanocrystalline Iron Oxide Based Electroactive Materials in Lithium Ion Batteries: The Critical Role of Crystallite Size, Morphology, and Electrode Heterostructure on Battery Relevant Electrochemistry. *Inorg. Chem. Front.* **2016**, *3* (1), 26–40.

(89) Yamauchi, S.; Hibino, M.; Yao, T. Structure Change Analysis in γ-Fe2O3/Carbon Composite in the Process of Electrochemical Lithium Insertion. *Solid State Ionics* **2011**, *191* (1), 45–48.

(90) Park, S.; Matsui, T.; Takai, S.; Yao, T. Crystal Structure Analysis of γ-Fe2O3 with

Chemical Lithium Insertion. *Solid State Ionics* **2014**, *255*, 50–55.

(91) Brady, N. W.; Knehr, K. W.; Cama, C. A.; Lininger, C. N.; Lin, Z.; Marschilok, A. C.; Takeuchi, K. J.; Takeuchi, E. S.; West, A. C. Galvanostatic Interruption of Lithium Insertion into Magnetite: Evidence of Surface Layer Formation. *J. Power Sources* **2016**, *321*, 106–111.

(92) Mitra, S.; Poizot, P.; Finke, A.; Tarascon, J.-M. Growth and Electrochemical Characterization versus Lithium of Fe3O4 Electrodes Made by Electrodeposition. *Adv. Funct. Mater.* **2006**, *16* (17), 2281–2287.

(93) Anderson, P. W. Ordering and Antiferromagnetism in Ferrites. *Phys. Rev.* **1956**, *102* (4), 1008–1013.

(94) Jeng, H.-T.; Guo, G. Y.; Huang, D. J. Charge-Orbital Ordering in Low-Temperature Structures of Magnetite: GGA+U Investigations. *Phys. Rev. B* **2006**, *74* (19), 195115.

(95) Jain, A.; Ong, S. P.; Hautier, G.; Chen, W.; Richards, W. D.; Dacek, S.; Cholia, S.; Gunter, D.; Skinner, D.; Ceder, G.; Persson, K. A. Commentary: The Materials Project: A Materials Genome Approach to Accelerating Materials Innovation. *APL Mater.* **2013**, *1* (1), 11002.

(96) Braun, P. B. A Superstructure in Spinels. *Nature* **1952**, *170* (4339), 1123.

(97) Fontcuberta, J.; Rodríguez, J.; Pernet, M.; Longworth, G.; Goodenough, J. B. Structural and Magnetic Characterization of the Lithiated Iron Oxide Li x Fe 3 O 4. *J. Appl. Phys.* **1986**, *59* (6), 1918–1926.

(98) Knehr, K. W.; Cama, C. A.; Brady, N. W.; Marschilok, A. C.; Takeuchi, K. J.; Takeuchi, E. S.; West, A. C. Simulations of Lithium-Magnetite Electrodes Incorporating Phase Change. *Electrochim. Acta* **2017**, *238*, 384–396.

(99) Daniels, J. M.; Rosencwaig, a. Mössbauer Spectroscopy of Stoichiometric and Non-Stoichiometric Magnetite. *J. Phys. Chem. Solids* **1969**, *30* (6), 1561–1571.

(100) Gallagher, K. J.; Feitknecht, W.; Mannweiler, U. Mechanism of Oxidation of Magnetite to G-Fe2O3. *Nature* **1968**, *217* (5134), 1118–1121.

(101) Shmakov, A. N.; Kryukova, G. N.; Tsybulya, S. V; Chuvilin, A. L.; Solovyeva, L. P. Vacancy Ordering in [Gamma]-Fe2O3: Synchrotron X-Ray Powder Diffraction and High-Resolution Electron Microscopy Studies. *J. Appl. Crystallogr.* **1995**, *28* (2), 141–145.

(102) Jørgensen, J.-E.; Mosegaard, L.; Thomsen, L. E.; Jensen, T. R.; Hanson, J. C. Formation of G-Fe2O3 Nanoparticles and Vacancy Ordering: An in Situ X-Ray Powder Diffraction Study. *J. Solid State Chem.* **2007**, *180* (1), 180–185.

(103) Grau-Crespo, R.; Al-Baitai, A. Y.; Saadoune, I.; De Leeuw, N. H. Vacancy Ordering and Electronic Structure of γ - Fe2O3 (Maghemite): A Theoretical Investigation. *J. Phys. Condens. Matter* **2010**, *22* (25), 255401.

(104) Hibino, M.; Terashima, J.; Yao, T. Reversible and Rapid Discharge–Charge Performance of γ–Fe2O3 Prepared by Aqueous Solution Method as the Cathode for Lithium-Ion Battery. *J. Electrochem. Soc.* **2007**, *154* (12), A1107.

(105) Park, S.; Oda, M.; Yao, T. Relaxation Structure Analysis of Li Inserted γ-Fe2O3. *Solid State Ionics* **2011**, *203* (1), 29–32.

(106) Frison, R.; Cernuto, G.; Cervellino, A.; Zaharko, O.; Colonna, G. M.; Guagliardi, A.; Masciocchi, N. Magnetite-Maghemite Nanoparticles in the 5-15 Nm Range: Correlating the Core-Shell Composition and the Surface Structure to the Magnetic Properties. A Total Scattering Study. *Chem. Mater.* **2013**, *25* (23), 4820–4827.

(107) Grau-Crespo, R.; Hamad, S.; Catlow, C. R. A.; Leeuw, N. H. De; de Leeuw, N. H. Symmetry-

Adapted Configurational Modelling of Fractional Site Occupancy in Solids. *J. Phys. Condens. Matter* **2007**, *19* (25), 256201.

(108) Shepherd, J. P.; Koenitzer, J. W.; Aragón, R.; Spal/ek, J.; Honig, J. M. Heat Capacity and Entropy Ofnonstoichiometric Magnetite Fe3(1-d)04: The Thermodynamic Nature Ofthe Verwey Transition. *Phys. Rev. B* **1991**, *43* (10), 8461–8471.

(109) Shafi, K. V. P. M.; Ulman, A.; Dyal, A.; Yan, X.; Yang, N.-L.; Estournès, C.; Fournès, L.; Wattiaux, A.; White, H.; Rafailovich, M. Magnetic Enhancement of γ-Fe2O3 Nanoparticles by Sonochemical Coating. *Chem. Mater.* **2002**, *14* (4), 1778–1787.

(110) Wang, J.; Ma, Y.; Watanabe, K. Magnetic-Field-Induced Synthesis of Magnetic γ-Fe2O3 Nanotubes. *Chem. Mater.* **2008**, *20* (1), 20–22.

(111) Berkowitz, A. E.; Schuele, W. J.; Flanders, P. J. Influence of Crystallite Size on the Magnetic Properties of Acicular γ-Fe2O3 Particles. *J. Appl. Phys.* **1968**, *39* (2), 1261–1263.

(112) Wang, Y.; Cao, G. Developments in Nanostructured Cathode Materials for High-Performance Lithium-Ion Batteries. *Adv. Mater.* **2008**, *20* (12), 2251–2269.

(113) Salazar, J. S.; Perez, L.; Abril, O. De; Phuoc, L. T.; Ihiawakrim, D.; Vazquez, M.; Greneche, J.; Begin-colin, S.; Pourroy, G. Magnetic Iron Oxide Nanoparticles in 10 - 40 Nm Range : Composition in Terms of Magnetite / Maghemite Ratio and Effect on the Magnetic Properties. *Chem. Mater.* **2011**, *23*, 1379–1386.

(114) Menard, M. C.; Marschilok, A. C.; Takeuchi, K. J.; Takeuchi, E. S. Variation in the Iron Oxidation States of Magnetite Nanocrystals as a Function of Crystallite Size: The Impact on Electrochemical Capacity. *Electrochim. Acta* **2013**, *94* (42), 320–326.

(115) Goss, C. J. Saturation Magnetisation, Coercivity and Lattice Parameter Changes in the

System Fe3O4-GammaFe2O3, and Their Relationship to Structure. *Phys. Chem. Miner.* **1988**, *16* (2), 164–171.

(116) Leapman, R. D.; Grunes, L. A.; Fejes, P. L. Study of the L23 Edges in the 3d Transition Metals and Their Oxides by Electron-Energy-Loss Spectroscopy with Comparisons to Theory. *Phys. Rev. B* **1982**, *26* (2), 614–635.

(117) Colliex, C.; Manoubi, T.; Ortiz, C. Electron-Energy-Loss-Spectroscopy near-Edge Fine Structures in the Iron-Oxygen System. *Phys. Rev. B* **1991**, *44* (20), 11402–11411.

(118) Okudera, H.; Yoshiasa, A.; Murai, K.; Okube, M.; Takeda, T.; Kikkawa, S. Local Structure of Magnetite and Maghemite and Chemical Shift in Fe K-Edge XANES. *J. Miner. Pet. Sci.* **2012**, *107*, 127–132.

(119) McCarty, K. F.; Monti, M.; Nie, S.; Siegel, D. A.; Starodub, E.; El Gabaly, F.; McDaniel, A. H.; Shavorskiy, A.; Tyliszczak, T.; Bluhm, H.; Bartelt, N. C.; de la Figuera, J. Oxidation of Magnetite(100) to Hematite Observed by in Situ Spectroscopy and Microscopy. *J. Phys. Chem. C* **2014**, *118* (34), 19768–19777.

(120) De Groot, F. M. F.; Grioni, M.; Fuggle, J. C.; Ghijsen, J.; Sawatzky, G. A.; Petersen, H. Oxygen 1s X-Ray-Absorption Edges of Transition-Metal Oxides. *Phys. Rev. B* **1989**, *40* (8), 5715–5723.

(121) Chen, S.-Y.; Gloter, A.; Zobelli, A.; Wang, L.; Chen, C.-H.; Colliex, C. Electron Energy Loss Spectroscopy and Ab Initio Investigation of Iron Oxide Nanomaterials Grown by a Hydrothermal Process. *Phys. Rev. B* **2009**, *79* (10), 104103.

(122) Hocking, R. K.; Wasinger, E. C.; De Groot, F. M. F.; Hodgson, K. O.; Hedman, B.; Solomon, E. I. Fe L-Edge XAS Studies of K4[Fe(CN)6] and K 3[Fe(CN)6]: A Direct Probe of Back-Bonding. *J. Am. Chem. Soc.* **2006**, *128* (32), 10442–10451.

(123) Van der Ven, A.; Wagemaker, M. Effect of Surface Energies and Nano-Particle Size Distribution on Open Circuit Voltage of Li-Electrodes. *Electrochem. commun.* **2009**, *11* (4), 881–884.

(124) Majzlan, J.; Navrotsky, A.; Schwertmann, U. Thermodynamics of Iron Oxides: Part III. Enthalpies of Formation and Stability of Ferrihydrite (~Fe(OH)3), Schwertmannite (~FeO(OH)3/4(SO4)1/8), and ε-Fe2O3. *Geochim. Cosmochim. Acta* **2004**, *68* (5), 1049–1059.

(125) Chase, M.W., J. NIST-JANAF Themochemical Tables. *J. Phys. Chem. Ref. Data* **1998**, *Monograph*, 1–1951.

(126) Andersson J.O., Helander T., Höglund L., Shi P.F., and S. B. Thermo-Calc and DICTRA, Computational Tools for Materials Science. SSBU Database. *Calphad* **2002**, *26*, 273–312.

(127) Sun, W.; Dacek, S. T.; Ong, S. P.; Hautier, G.; Jain, A.; Richards, W. D.; Gamst, A. C.; Persson, K. A.; Ceder, G. The Thermodynamic Scale of Inorganic Crystalline Metastability. *Sci. Adv.* **2016**, *2* (11), e1600225–e1600225.

(128) Lininger, C. N.; Brady, N. W.; West, A. C. Equilibria and Rate Phenomena from Atomistic to Mesoscale: Simulation Studies of Magnetite. *Acc. Chem. Res.* **2018**, *51* (3), 583–590.

(129) Kresse, G.; Furthmüller, J. Efficient Iterative Schemes for Ab Initio Total-Energy Calculations Using a Plane-Wave Basis Set. *Phys. Rev. B* **1996**, *54* (16), 11169–11186.

(130) Kresse, G.; Joubert, D. From Ultrasoft Pseudopotentials to the Projector Augmented-Wave Method. *Phys. Rev. B* **1999**, *59* (3), 1758.

(131) Blöchl, P. E. Projector Augmented-Wave Method. *Phys. Rev. B* **1994**, *50* (24), 17953–17979.

(132) Jain, A.; Hautier, G.; Ong, S. P.; Moore, C. J.; Fischer, C. C.; Persson, K. A.; Ceder, G. Formation Enthalpies by Mixing GGA and GGA + U Calculations. *Phys. Rev. B* **2011**, *84* (4), 045115.

(133) Perdew, J. P.; Burke, K.; Wang, Y. Generalized Gradient Approximation for the Exchange-Correlation Hole of a Many-Electron System. *Phys. Rev. B* **1996**, *54* (23), 16533–16539.

(134) Meng, Y. S.; Arroyo-de Dompablo, M. E. First Principles Computational Materials Design for Energy Storage Materials in Lithium Ion Batteries. *Energy Environ. Sci.* **2009**, *2* (6), 589–609.

(135) Islam, M. S.; Fisher, C. A. J. Lithium and Sodium Battery Cathode Materials: Computational Insights into Voltage, Diffusion and Nanostructural Properties. *Chem. Soc. Rev.* **2014**, *43* (1), 185–204.

(136) Fjellvåg, H.; Hauback, B. C.; Vogt, T.; Stølen, S. Monoclinic Nearly Stoichiometric Wüstite at Low Temperatures. *Am. Mineral.* **2002**, *87* (2–3), 347–349.

(137) Fjellvåg, H.; Grønvold, F.; Stølen, S.; Hauback, B. On the Crystallographic and Magnetic Structures of Nearly Stoichiometric Iron Monoxide. *J. Sol. Stat. Chem.* **1996**, *124* (124), 52–57.

(138) Abdel-Ghany, A. E.; Mauger, A.; Groult, H.; Zaghib, K.; Julien, C. M. Structural Properties and Electrochemistry of α-LiFeO2. *J. Power Sources* **2012**, *197*, 285–291.

(139) Michaelsen, C. On the Structure and Homogeneity of Solid Solutions: The Limits of Conventional X-Ray Diffraction. *Philos. Mag. A* **1995**, *72* (3), 813–828.

(140) Perdew, J. P.; Burke, K.; Ernzerhof, M. Generalized Gradient Approximation Made Simple. *Phys. Rev. Lett.* **1996**, *77* (18), 3865–3868.

(141) Dudarev, S. L.; Savrasov, S. Y.; Humphreys, C. J.; Sutton, a. P.; Botton, G. A.; Savrasov, S. Y.; Humphreys, C. J.; Sutton, a. P. Electron-Energy-Loss Spectra and the Structural Stability of Nickel Oxide: An LSDA+U Study. *Phys. Rev. B* **1998**, *57* (3), 1505–1509.

(142) Methfessel, M.; Paxton, A. T. High-Precision Sampling for Brillouin-Zone Integration in Metals. *Phys. Rev. B* **1989**, *40* (6), 3616–3621.

(143) Meredig, B.; Thompson, A.; Hansen, H. A.; Wolverton, C.; van de Walle, A. Method for Locating Low-Energy Solutions within DFT+U. *Phys. Rev. B* **2010**, *82* (19), 195128.

(144) Izumi, F.; Momma, K. Three-Dimensional Visualization in Powder Diffraction. *Solid State Phenom.* **2007**, *130*, 15–20.

(145) Momma, K.; Izumi, F. VESTA 3 for Three-Dimensional Visualization of Crystal, Volumetric and Morphology Data. *J. Appl. Crystallogr.* **2011**, *44*, 1272–1276.

(146) Matsui, M.; Tōdō, S.; Chikazumi, S. Magnetization of Low Temperature Phase of Fe3O4. *J. Phys. Soc. Japan* **1977**, *43* (1), 47–52.

(147) Roth, W. L. Magnetic Structures of MnO, FeO, CoO, and NiO. *Phys. Rev.* **1958**, *110* (6), 1333–1341.

(148) Fischer, G.; Däne, M.; Ernst, A.; Bruno, P.; Lüders, M.; Szotek, Z.; Temmerman, W.; Hergert, W. Exchange Coupling in Transition Metal Monoxides: Electronic Structure Calculations. *Phys. Rev. B* **2009**, *80* (1), 014408.

(149) Barré, M.; Catti, M. Neutron Diffraction Study of the B′ and γ Phases of LiFeO2. *J. Solid State Chem.* **2009**, *182* (9), 2549–2554.

(150) Anderson, J. C.; Dey, S. K.; Halpern, V. The Magnetic Susceptibilities of LiFeO2. *J. Phys. Chem. Solids* **1965**, *26* (9), 1555–1560.

(151) Ong, S. P.; Richards, W. D.; Jain, A.; Hautier, G.; Kocher, M.; Cholia, S.; Gunter, D.;

Chevrier, V. L.; Persson, K. A.; Ceder, G. Python Materials Genomics (Pymatgen): A Robust, Open-Source Python Library for Materials Analysis. *Comput. Mater. Sci.* **2013**, *68*, 314–319.

(152) Hart, G. L. W.; Forcade, R. W. Algorithm for Generating Derivative Structures. *Phys. Rev. B* **2008**, *77* (22), 224115.

(153) Tang, J.; Wang, K.; Zhou, W. Magnetic Properties of Nanocrystalline Fe 3 O 4 Films Magnetic Properties of Nanocrystalline Fe 3 O 4 Films. **2014**, *7690* (2001), 9–12.

(154) Jeng, H.-T.; Guo, G. Y.; Huang, D. J. Charge-Orbital Ordering and Verwey Transition in Magnetite. *Phys. Rev. Lett.* **2004**, *93* (15), 1–4.

(155) Saal, J. E.; Kirklin, S.; Aykol, M.; Meredig, B.; Wolverton, C. Materials Design and Discovery with High-Throughput Density Functional Theory: The Open Quantum Materials Database (OQMD). *JOM* **2013**, *65* (11), 1501–1509.

(156) Kirklin, S.; Saal, J. E.; Meredig, B.; Thompson, A.; Doak, J. W.; Aykol, M.; Rühl, S.; Wolverton, C. The Open Quantum Materials Database (OQMD): Assessing the Accuracy of DFT Formation Energies. **2015**, *1*, 15010.

(157) Stevanović, V.; Lany, S.; Zhang, X.; Zunger, A. Correcting Density Functional Theory for Accurate Predictions of Compound Enthalpies of Formation: Fitted Elemental-Phase Reference Energies. *Phys. Rev. B* **2012**, *85* (11), 115104.

(158) Seo, D.-H.; Urban, A.; Ceder, G. Calibrating Transition-Metal Energy Levels and Oxygen Bands in First-Principles Calculations: Accurate Prediction of Redox Potentials and Charge Transfer in Lithium Transition-Metal Oxides. *Phys. Rev. B* **2015**, *92* (11), 115118.

(159) O. Kubaschewski, C. B. Alcock, P. J. S. Materials Thermochemistry. In *Materials*

Thermochemistry; Pergamon Press: Oxford, UK, 1993; pp 257–323.

APPENDIX

Appendix 1: Typical VASP INCAR File

SYSTEM = Structure Name

NPAR = 8; # Varies per cluster and cluster hardware
ISTART=0; # New or CHGCAR =0 & RESTART From WAVECAR=1,
ICHARG=2; # Make rho from superposition atoms=2; Read from CHGCAR = 1, band structure = 11
PREC=HIGH;
LREAL = FALSE ; # For large supercell
LWAVE=FALSE; # Don't write WAVECAR

# Auto Relax Parameters
IBRION = 2
ISIF = 3 #Change all degrees of freedom
NSW = 500 # 15 steps of ionic relaxation

ISPIN = 2 # Spin Polarized Calculation (=1 is non spin polarized)
MAGMOM = Specified as + and – for spin up and spin down Fe, iron magnitude always inflated by 1.3x, oxygen and lithium initialized at 0.0

ENMAX = 600 # 1.3*Cutoff energy for plane-wave basis
EDIFF = 1E-4 # Allowed error in total energy
EDIFFG = -0.05 # Force cutoff criterion

ISMEAR = 1 # KPoints Broadening Method (TET=-5; GAUSS=0; MP=1)
LORBIT = 11 # Write DOSCAR and lm decomposed PROCAR for outputs

#Hubbard U
LDAU = .TRUE. # FeO is a strongly correlated material
LDAUTYPE = 1 # (2) Simple Rotationally invariant LSDA+U (1) Rotationally invariant
LDAUL = 2 -1 -1 # Need to specify l-quantum number for each species which on-site interaction is added, 2 means d-orbital, -1 means no on-site interaction added
LDAUU = 5.3 0.0 0.0 # U Value is 5.3 for Fe and 0 for Oxygen
LDAUJJ = 0.0 0.0 0.0 # J value for each species

Appendix 2: Atomic Coordinates (VASP) for Lowest Energy Fe_3O_4

```
Fe3O4 Lowest Energy Fd3m
  1.00000000000000
    8.5047847207930687    0.0073953292784249    0.0000000000000000
   -0.1097001646308138    8.5040804153758902    0.0000000000000000
    0.0000000000000000    0.0000000000000000    8.6015566877000307
  Fe   O
   24   32
Direct
 0.5000000000000000  0.5000000000000000  0.9933578925468129
-0.0000000000000000 -0.0000000000000000  0.9933578925468129
 0.5000000000000000 -0.0000000000000000  0.4933578925468131
-0.0000000000000000  0.5000000000000000  0.4933578925468131
 0.2500000000000000  0.7500000000000000  0.2566420774531844
 0.7500000000000000  0.2500000000000000  0.2566420774531844
 0.2500000000000000  0.2500000000000000  0.7566421074531871
 0.7500000000000000  0.7500000000000000  0.7566421074531871
 0.6250000000000000  0.3750000000000000  0.6250000000000000
 0.1250000000000000  0.8750000000000000  0.6250000000000000
 0.6250000000000000  0.8750000000000000  0.1250000000000000
 0.1250000000000000  0.3750000000000000  0.1250000000000000
 0.6250000000000000  0.6250000000000000  0.3750000000000000
 0.1250000000000000  0.1250000000000000  0.3750000000000000
 0.6250000000000000  0.1250000000000000  0.8750000000000000
 0.1250000000000000  0.6250000000000000  0.8750000000000000
 0.3750000000000000  0.6250000000000000  0.6250000000000000
 0.8750000000000000  0.1250000000000000  0.6250000000000000
 0.3750000000000000  0.1250000000000000  0.1250000000000000
 0.8750000000000000  0.6250000000000000  0.1250000000000000
 0.3750000000000000  0.3750000000000000  0.3750000000000000
 0.8750000000000000  0.8750000000000000  0.3750000000000000
 0.3750000000000000  0.8750000000000000  0.8750000000000000
 0.8750000000000000  0.3750000000000000  0.8750000000000000
 0.3768005128823479  0.6231994871176525  0.3878594485802104
 0.8768005128823475  0.1231994871176523  0.3878594485802104
 0.3768005128823479  0.1231994871176523  0.8878594775802096
 0.8768005128823475  0.6231994871176525  0.8878594775802096
 0.3824608804281517  0.3824609104281471  0.6269189712001370
 0.8824608504281491  0.8824609104281471  0.6269189712001370
 0.3824608804281517  0.8824609104281471  0.1269189712001370
 0.8824608504281491  0.3824609104281471  0.1269189712001370
 0.6231994871176525  0.3768005128823479  0.3878594485802104
 0.1231994871176522  0.8768005128823475  0.3878594485802104
 0.6231994871176525  0.8768005128823475  0.8878594775802096
 0.1231994871176522  0.3768005128823479  0.8878594775802096
 0.6175390895718530  0.6175391495718507  0.6269189712001370
 0.1175390895718531  0.1175391495718508  0.6269189712001370
 0.6175390895718530  0.1175391495718508  0.1269189712001370
 0.1175390895718531  0.6175391495718507  0.1269189712001370
 0.8731994871176525  0.1268005128823477  0.8621405224197904
 0.3731994871176521  0.6268005128823475  0.8621405224197904
 0.8731994871176525  0.6268005128823475  0.3621405224197908
 0.3731994871176521  0.1268005128823477  0.3621405224197908
 0.6324608504281491  0.1324609104281470  0.6230809687998652
 0.1324608504281491  0.6324609104281471  0.6230809687998652
 0.6324608504281491  0.6324609104281471  0.1230809687998651
 0.1324608504281491  0.1324609104281470  0.1230809687998651
 0.6268005128823475  0.3731994871176521  0.8621405224197904
 0.1268005128823478  0.8731994871176525  0.8621405224197904
 0.6268005128823475  0.8731994871176525  0.3621405224197908
 0.1268005128823478  0.3731994871176521  0.3621405224197908
 0.8675390895718530  0.3675391495718507  0.6230809687998652
 0.3675390895718529  0.8675391495718507  0.6230809687998652
 0.8675390895718530  0.8675391495718507  0.1230809687998651
 0.3675390895718529  0.3675391495718507  0.1230809687998651
```

Appendix 3: Atomic Coordinates (VASP) for Lowest Energy $LiFe_3O_4$

```
LiFe3O4 Lowest Energy SOD Structure
  1.00000000000000
    8.6139182656488202   0.0175742177150267  -0.0031276966106799
    0.0174792936170002   8.6518746458560862   0.0127048142644401
   -0.0031497983664371   0.0128874044638733   8.5538169811733482
  Fe   O    Li
   24   32    8
Direct
  0.5007770544363331  0.5026244003733796  0.4987257390188755
  0.2506705047008336  0.7518041978467868  0.0028790917567265
  0.7463813368424443  0.0019833232498331  0.2526080363562075
  0.0038184824285477  0.2493952571870694  0.7527552660699514
  0.7532455164032805  0.2503428741897567  0.0018262072730924
  0.2506186067993423  0.0001920954346210  0.7446240184786364
  0.9996753478993916  0.7520483150500100  0.2502128603279298
  0.4969810200725307  0.0012777565279966  0.0030564326746898
  0.2526770050804218  0.2503394743975853  0.5021073873666835
  0.7488628367221908  0.4954740481712616  0.7482013623328448
  0.7423395407100357  0.7487386541717121  0.4925715318680896
  0.2523501755595382  0.5026716415237686  0.2514534205717321
  0.0039180086196137  0.4975391106105477  0.0000195978622439
  0.5027878159074409  0.2494966002216747  0.2544206695729378
  0.4940668014814530  0.7507857072749713  0.7459225028396346
  0.9991473898529170  0.9991523337984696  0.5005925382085785
  0.4986385779038850  0.2494780518495795  0.7490624278098125
  0.0001364960150731  0.5007307083590774  0.5020617349022863
  0.7495980101681855  0.7490414575170623  0.0047084305635395
  0.2516830123311343  0.9991780349302566  0.2551446865551625
  0.7486433713341524  0.0034962627926593  0.7470964617510084
  0.0016193574863702  0.7478419724266028  0.7491338669078016
  0.9997232049270317  0.2480559344195811  0.2479082169504262
  0.5006389175780726  0.4987602687496214  0.9986784993246819
  0.2610185727129728  0.2578335657598754  0.2441807537582473
  0.4887755440331502  0.0088289855736911  0.7466807577801937
  0.9847443544218986  0.7543080769811892  0.4933642747583951
  0.7425642210921224  0.5113664557398978  0.0022828648770064
  0.0143203398124622  0.4900185712052458  0.2579181747608705
  0.7574493843572995  0.7465700686612682  0.7409688886113456
  0.5087600159299008  0.2459562933528636  0.0103753941939784
  0.2500858589353899  0.9959137722391236  0.5023129916430770
  0.5065028659443216  0.0144435731030571  0.2559175061188023
  0.0069897216832948  0.2437035682154652  0.5094416329170719
  0.2601503666826133  0.5142097548423880  0.0097797162926131
  0.0071225519694805  0.4872949409110646  0.7424229818658482
  0.4903664153951510  0.7563378968274629  0.9899969057410671
  0.7454615964610088  0.9865909671084491  0.4993813534297652
  0.2402419512283783  0.7637132459131829  0.7608030994327794
  0.4935634447183089  0.4890765260456740  0.2570024656084958
  0.9950028619920526  0.2578758807624537  0.9908387973056938
  0.0073600963325328  0.0097076955657737  0.7538053608339396
  0.7415160800056750  0.2379260383214645  0.2554744738880160
  0.5070544088221044  0.7383393586002405  0.5049276167022297
  0.4942458850477438  0.4899436731089958  0.7387607735409822
  0.0092328718880953  0.7394540796016523  0.0070068125315042
  0.9877550927571678  0.0088458281109551  0.2476883402677855
  0.4976712701066379  0.2647356950157103  0.4923726745614253
  0.7617108371994592  0.2517170209386724  0.7446455458917322
  0.2613176810290297  0.5055998912242663  0.4888026919535027
  0.2534110245697168  0.7423588562954709  0.2420165772192972
  0.7507334435376956  0.9903189426287363  0.0013027845845986
  0.7413678699578581  0.5132092371728738  0.4923091481542842
  0.2468835141702448  0.9867905908202274  0.0038523331472632
  0.7438103671688611  0.7667457570704577  0.2571969289256215
  0.2409061300301069  0.2347273965218227  0.7573706248090860
  0.0038971586275909  0.0034389236023903  0.0003004103229656
  0.7481499726228551  0.2524583005546678  0.4973387675855525
  0.2513611870870905  0.4985644610739078  0.7475674456980838
  0.4978950178835785  0.7525682442697865  0.2560630161270600
  0.2611402875712199  0.7497302067119166  0.4947098917981088
  0.7461825058695919  0.4971931923123248  0.2499232876432061
  0.2468021126469720  0.2463366136022291  0.9992315239574141
  0.4974767264381668  0.9947993725592197  0.4978934234175029
```

Appendix 4: Lowest energy structures for lithium insertion into $Fe_{2.875}O_4$ with the iron defect on a 16d site. Lithium insertion onto the 16d defect a) x=0.125 and split interstitial of the 16d defect b) x=0.25. All calculations were performed in eight formula unit cell. Brown atoms are Fe_{16d}, red atoms are oxygen at 32e, dark blue atoms are Fe_{8a}, green atoms are lithium inserted at 16d site.

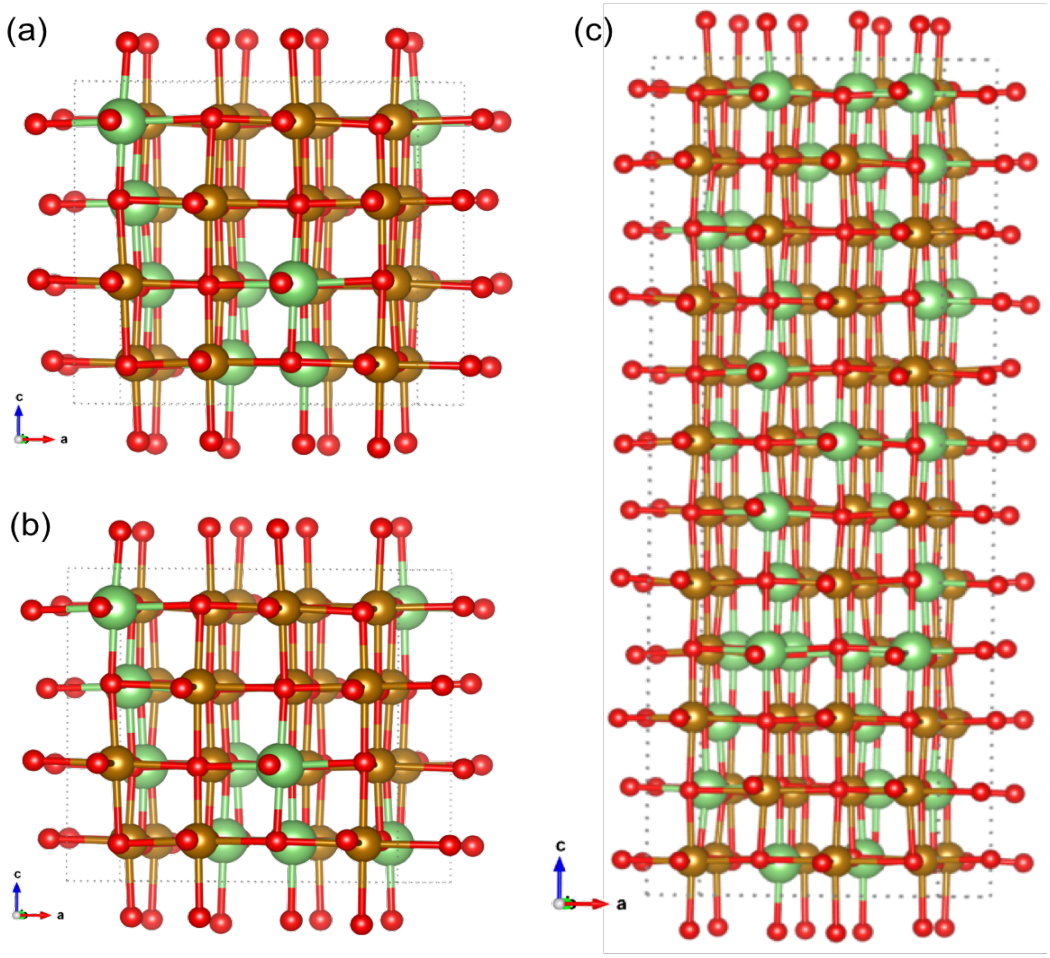

Appendix 5: Core-Shell Particle Formulation

The nanoparticle size is determined by applying the Scherrer equation to the FWHM of the (311) peak of the pristine XPD pattern of the pristine unlithiated materials, from which the radius of the particle is determined as r_p. In the model formulation of the nanoparticles, every particle, independent of diameter, was assumed to have a 1.2 nm penetration depth of

cationic defects at the 16d site. The defect region was treated as γ-$Fe_{2.67}O_4$ bulk DFT calculation and the rest of the nanoparticle was treated as Fe_3O_4 bulk DFT calculation. The average lithium concentration in a single particle, $\bar{x}$, was calculated as the volumetric fraction (v_d) of lithium in the defective γ-$Fe_{2.67}O_4$ surface, $x_d v_d$, plus the volumetric fraction of lithium in the Fe_3O_4 core, $x_c(1 - v_d)$.

Appendix 6: EELS in Random Scan Direction. (a) Radom scan direction in 60 nm Fe_3O_4 nanoparticle. (b) plasmon peak, (c) low-loss, and (d) core loss regions for 3 nm depth (red) and 45 nm depth (blue) into 60 nm particle.

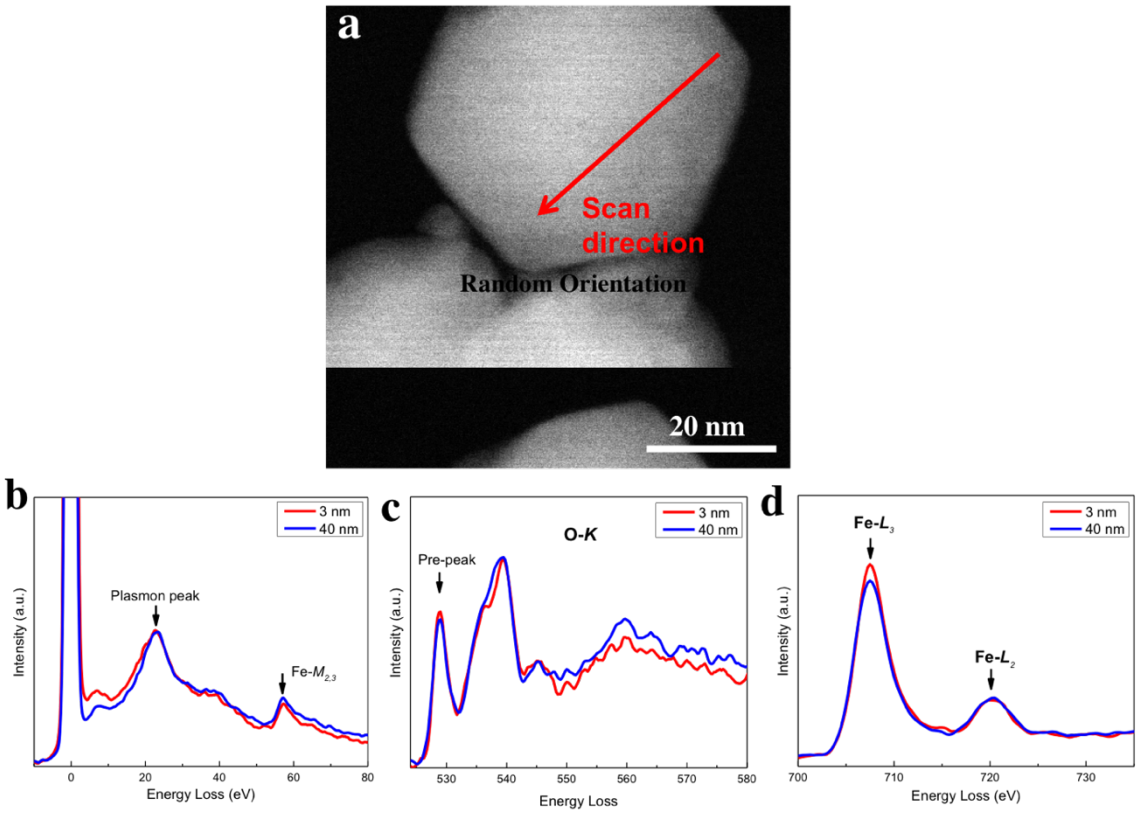

Appendix 7: Open circuit potential measurements for samples used for XRD and Neutron Diffraction characterization compared to the reversible potential of coin cell samples.

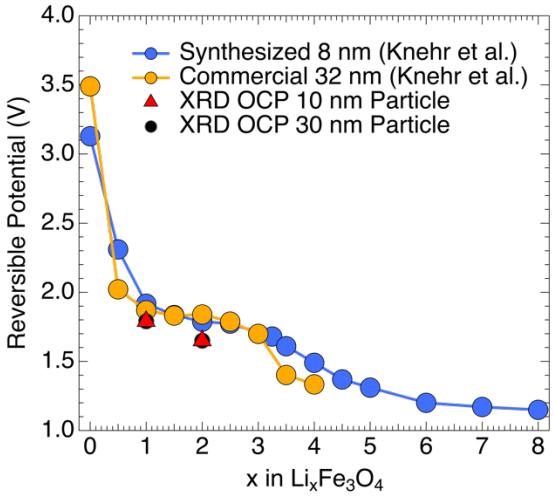

Appendix 8: Investigation of $LiFe_3O_4$ XRD Patterns in Different Supercell Sizes

The $LiFe_3O_4$ phase in an eight formula unit cell produces low angle peaks not observed experimentally at x=2.0. The same $LiFe_3O_4$ structure was tested in a smaller two formula unit cell, allowing for lithium and iron to relax freely over both 16c and 16d sites. The result was that there were less low angle peaks than in the eight formula unit cell, but still peaks inconsistent with experiment, as can be seen in the accompanying figure below.